Physically based irradiance model for photovoltaic applications

Development and validation of an irradiance model that combines ray tracing and view factors

by D. P. Gribnau

TU Delft

Physically based irradiance model for photovoltaic applications

Development and validation of an irradiance model that combines ray tracing and view factors

by

by D. P. Gribnau

to obtain the degree of Master of Science
at the Delft University of Technology,
to be defended publicly on **26th of November** at 9:00 AM.

Student number:	4377419	
Supervisor:	Dr. O. Isabella	
Daily supervisor:	A. Calcabrini	
Project duration:	Sept, 2019 – Nov, 2020	
Thesis committee:	Dr. O. Isabella,	Ass. Prof. EEMCS TU Delft& Head of PVMD group
	A. Calcabrini	PhD. Candidate
	Prof. Dr. ir. E. Eisseman,	Ass. Prof. EEMCS TU Delft & Head of TU Delft CGV group
	Dr. P. Manganiello	Ass. Prof. EEMCS TU Delft

An electronic version of this thesis is available at `http://repository.tudelft.nl/`.

TU Delft

Abstract

The installation of photovoltaic systems in the urban environment is becoming increasingly common. These photovoltaic systems are affected by a large fraction of reflected irradiance as well as partial shading. In a similar way these issues also have an important effect on bifacial photovoltaic power plants.

Irradiance models that are able to take these issues into account are therefore gaining interest. For an accurate economic assessment of a PV system and the calculation of delivered power it is becoming very important to be able to accurately determine the irradiance on a PV system. Therefore there is a rising demand for accurate irradiance models that are able to take into account the effects that arise in complex geometric scenarios. The research in this thesis report aims to develop such a model which is able calculate the irradiance incident on bifacial modules and PV arrays in complex landscapes by combining the concepts of ray tracing and 3D view factors. The implementation of the proposed model decouples the irradiance simulation into independent blocks that allow to efficiently calculate the spectrally-resolved irradiance incident on a PV module. This decoupling makes the proposed model suitable for simulation of tandem devices in the near future.

The developed simulation has been experimentally validated using measurements from the PVMD monitoring station and also in comparison with other sophisticated irradiance simulation models. Experiments with a large fraction of specular reflected irradiance showed a good match between the measured and the simulated irradiance. Validation over a longer time period was also performed for 3 different sensors on the PVMD monitoring station roof. The results show an overall low mean bias error between the measured and simulated irradiance for the time period between mid-August 2020 to mid-October 2020.

The proposed model is able to model the irradiance impinging on a PV system in a complex urban environment using a decoupled structure and its performance is comparable to sophisticated existing ray tracing models. The performed simulations show a good match with the measurements for different situations. Further improvements are the implementation of higher order reflections, computational optimization and more extensive validation.

Preface

by D. P. Gribnau
Delft, November 2020

Dear reader...

Let me begin with thanking you for taking the time to read my thesis. This thesis is the final work of my MSc programme of Sustainable Energy Technology at the TU Delft. In the last years I have worked on this research project within the PVMD group at the Delft University of Technology. Ever since following the PV systems course I knew the system side of photovoltaic energy was the direction that appealed to me most during the Master's programme. The geometrical challenges, mathematical elegance and modelling side appealed to me from the very start. When I was looking for a project I quickly got in contact with Andres Calcabrini. His proposal for creating a new simulatoin model for calculating irradiance immediately sparked my enthusiasm.

Over the last year I have cooperated with Andres Calcabrini and worked on developing this model and delving in the theory behind it. I looked into the different current methods of irradiance modelling and worked on new ways it could be implemented in a new framework. This framework was developed and improved upon in MATLAB and consequently the developed framework was validated with measurements taken at the PVMD monitoring station. This preface is however not for diving into the thesis' subject matter but for expressing gratitude to a number of people.

There I must start with my supervisor Andres Calcabrini. Your excellent technical supervision helped me a lot with understanding the tough and complex subjects of this thesis. However, this is not what I am most thankful for. When times were challenging your attitude was always very understanding and supportive and this is something I will surely not forget. I really enjoyed working with you and the many calls we had about how certain modelling principles should be interpreted. Many thanks and I want to wish you good luck with finishing your PhD!

Next to that I want to thank my housemates Job van der Linden and Dennis Osseweijer. Due to the corona pandemic the time of my thesis was not without challenges. You guys were always there for a nice talk, a laugh or for general support. I will never forget this and I am very grateful to have you guys as friends.

Last but surely not least I am thankful to my family. My brother and my parents who are always there for me and supported me throughout my studies and my thesis. I could not have done it without you. I love you guys!

Contents

List of Figures

List of Tables

1 Introduction

The threat of climate change is one of the biggest challenges in the 21st century for whole mankind. The core of the problem lies at huge amount of CO_2 emissions due to the burning of fossil fuels. To reduce the amount of greenhouse gasses (like CO_2) that are emitted, greener more sustainable sources should be used for our energy supply. This transition is expected to become even more critical as current projections predict the energy demand to increase worldwide as shown in Figure 1.1 [15]. Figure 1.1 also shows that the shares

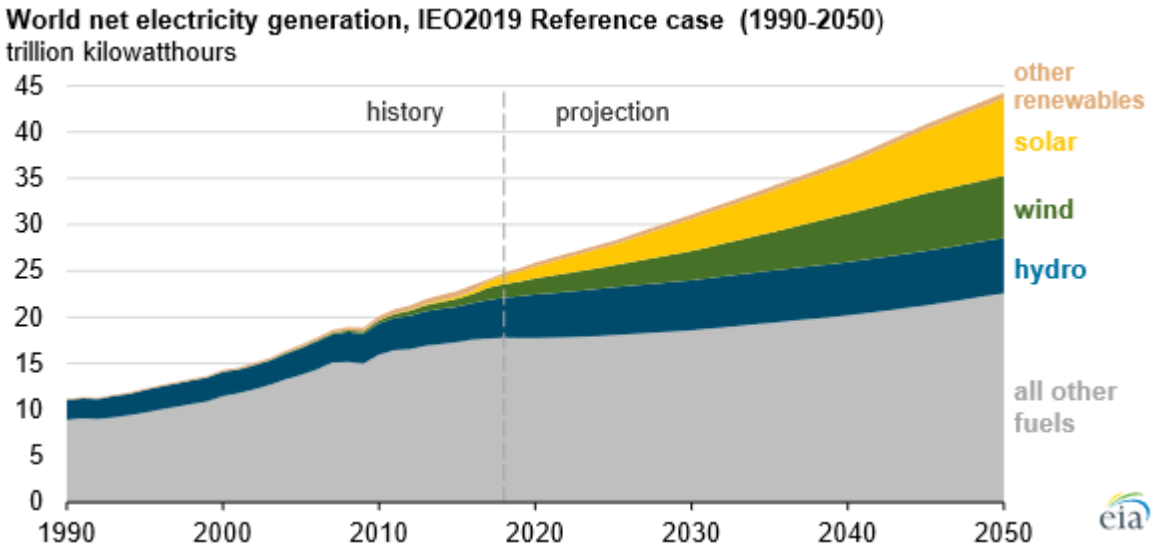

Figure 1.1: Energy demand projection and their expected type of generation in trillion kWh up until 2050. Retrieved from [15].

of renewable energy sources such as solar and wind energy are expected to increase in the energy sector. As these fields are still relatively young there is still a lot of research to be done in the renewable energy field.

As shown in Figure 1.1 solar energy looks like it will be one of the important players in the future energy. The growth of the solar energy is expected for a number of reasons [35]:

- **Availability**: sunlight is available at almost every location on earth.
- **Cost**: the cost of PV panels is dropping rapidly. For a number of locations solar energy is already the cheapest energy source. Even cheaper than non-renewable energy plants.

- **Flexibility**: the flexibility of the PV technology makes this technology suitable to install in a lot of different locations. So not only deserts or wide open spaces but also urban environments are suitable.
- **Predictability** : the seasonal and daily fluctuations are more predictable than for example wind energy.

These reasons make solar energy one of the most attractive renewable energy sources. Therefore the share of solar energy in the energy mix is projected to grow substantially worldwide which is shown in Figure 1.2. The most commonly used method of solar energy production are the photovoltaic (PV) technologies. Photo-

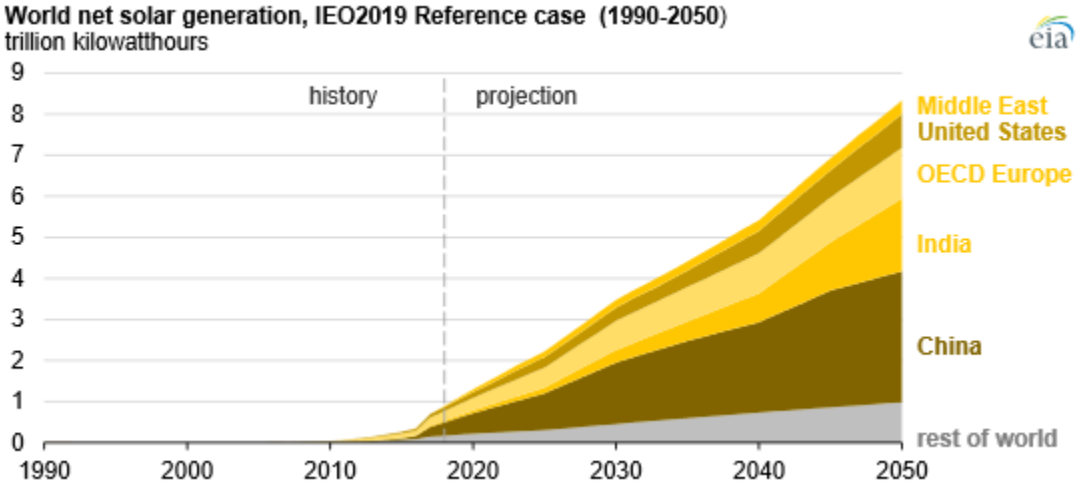

Figure 1.2: Projected electricity generation with their respective sources in trillion kWh for different parts of the world until 2050. Retrieved from [15].

voltaic systems are able to directly convert the sunlight into electricity. Another common form of solar energy is solar thermal energy. This technology converts the sunlight into thermal energy which can consequently be used to generate electricity. This thesis will solely focus on the photovoltaic technology. Thi focus of this thesis is to create a model that can calculate the irradiance incident on this PV technology. But why is it so important to be able to model this irradiance?

1.1. Why do we model irradiance?

As mentioned before there is a rapidly increasing demand for PV technologies. Therefore it is of crucial importance to be able to model the irradiance on these PV technologies. By being able to accurately model the irradiance and yield of your PV system one can make a reliable economic assessment of the system. This allows for better calculations of the systems feasibility and payback time. Additionally, as the share of renewables in the energy mix is increasing, the flow of all this renewable power needs to be managed. The PV system design and the grid management depend on the incoming irradiance. Being able to model this irradiance and therefore the power flows is very beneficial for improved grid management and design.

In designing these irradiancemodels, it is useful to look at the trends of the PV market as they affect the demand of what the developed model need to be able calculate. One of these trends is the location of installation.

A very prominent trend in the location of installation is the increasing deployment of PV technologies into urban environments. Due to the fact that more and more people are living in cities and in general the urban environment is growing around the world. It can be expected that installations of PV systems in cities will keep increasing. Residential PV (i.e PV panels on rooftops) is expected to have a substantial share in the total

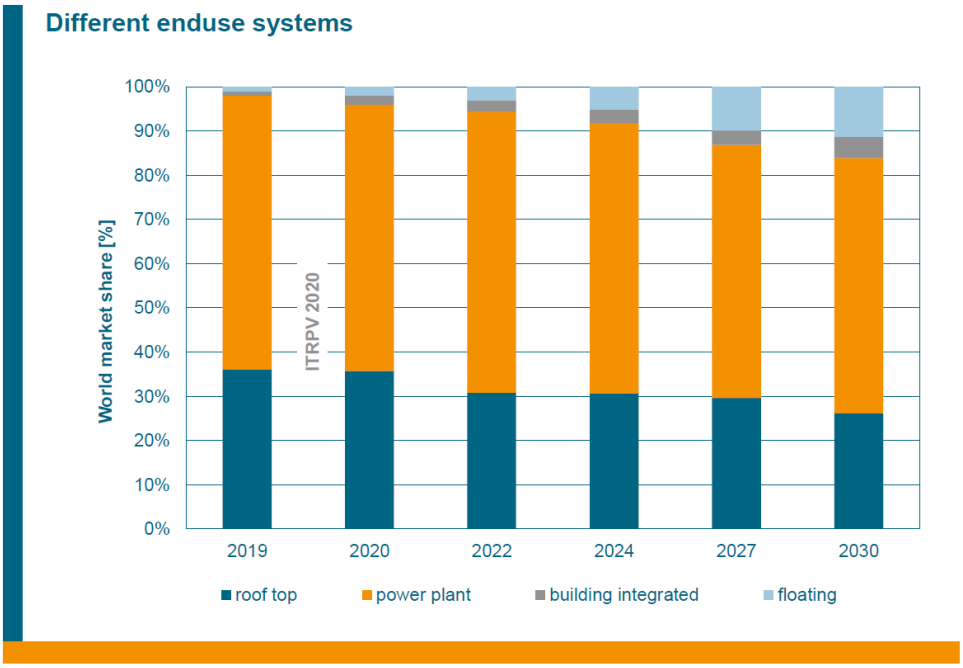

Figure 1.3: Trend of relative market share of different end-use PV systems from 2019-2030. Retrieved from [12].

PV. The trend of how different types of PV systems make up the total PV sector can be seen in Figure 1.3 [12]. Also shown in Figure 1.3 is the increasing share of building integrated PV or short BIPV in the solar energy mix. This BIPV technology is the integration of panels in the buildings itself. An example of this technology can be seen in the glass roof of Rotterdam Centraal train station. The solar panels are integrated within the glass as shown in Figure 1.4. Even though PV power plants will still have the largest share in the future, resi-

Figure 1.4: Building integrated solar panels in the glass roof of the Rotterdam Centraal station. Retrieved from [3].

dential PV and BIPV are expected to occupy at least 20 % share of the total PV market.

Due to this growth the relevance of understanding the effect of the complex environment around residential PV and BIPV a will become more and more relevant. Reflections caused by buildings, walls, glasses and other materials and structures as well as shading will play a substantial role in these types of systems compared to power plants. This is why there is an increasing demand for irradiance models that take into account

these effects.

Additionally, there is another fast growing PV technology that also is affected by reflected irradiance. This technology is the bifacial PV technology. To understand why bifacial PV also deals with an increased fraction of reflected irradiance it is crucial to know the difference between bifacial modules and conventional monofacial modules.

Normally light travels through a transparent front side of the module and is absorbed. The back surface will be opaque and not allow any light to pass through. Bifacial modules are designed differently. The backside is designed in such a way that the bifacial solar cell can absorb reflected light from the ground as well. For bifacial panels there is another parameter that is used to characterize the efficiency of the system. This parameter is called the bifaciality and can be seen as the fraction of how efficient the rear side is compared to the front side of the surface. The bifaciality is defined in equation 1.1[26].

$$\text{bifaciality} = \frac{\text{rear surface efficiency}}{\text{front surface efficiency}} \tag{1.1}$$

This equation assumes the same incident irradiance on both the front and back of the panel. The gain this bifacial module has compared to a monofacial module is expressed in the bifacial gain given in Equation 1.2[37].

$$\text{Bifacial Gain} = (Y_{\text{Bi}} - Y_{\text{Mono}}) / Y_{\text{Mono}} \tag{1.2}$$

In this equation Y_{Bi} and Y_{Mono} are the bifacial and monofacial yields respectively[37]. Due to the advantages bifacial panels give compared to monofacial panels the "International Technology Roadmap for PV"(ITRPV) [10] expect a growth of almost 50% in the bifacial PV market. In 2019 the market share is 13% and it is expected to be close to 60%. This trend can be seen in Figure 1.5. Due to this growth the simulation of bifacial modules

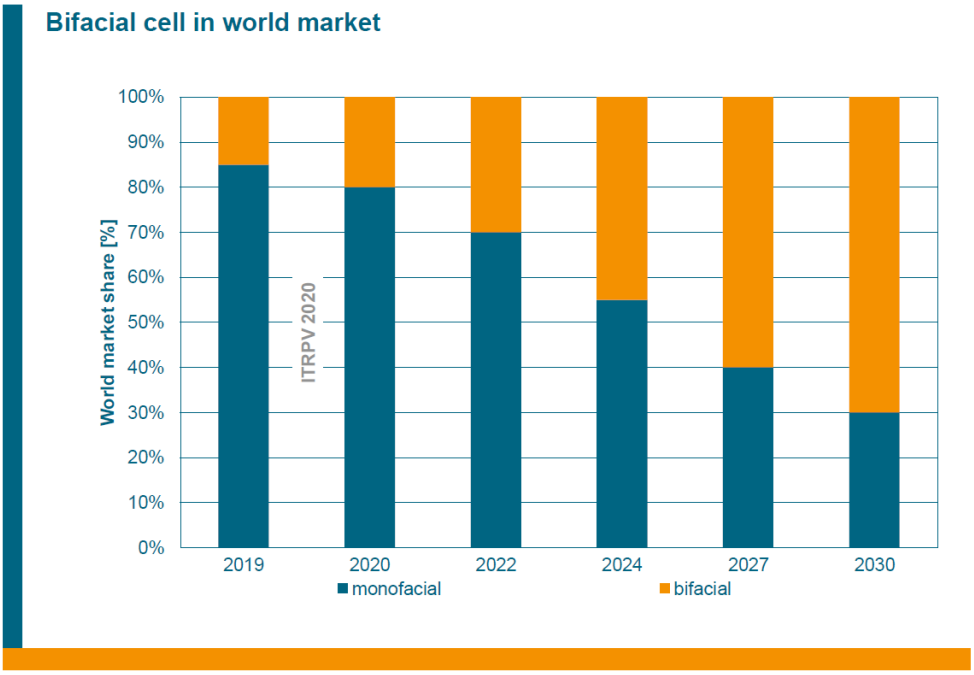

Figure 1.5: Bifacial market share trend from 2019 to 2029 as projected by the ITRPV. Retrieved from [10].

that deals with the same issues of reflected light as the urban environment PV is becoming very important. Therefore these types of models are getting more attention and becoming more intricate. Currently there are already numerous models to calculate bifacial PV yield. These types of models need to be continuously improved and explored as this thesis will also try to do.

There is another trend in the PV field that is expected to have an increased share in the PV energy mix in the future. This technology is called tandem PV. The requirements of modelling tandem PV is unrelated the geometrical problems as discussed before but related to the nature of how tandem PV works. To explain this, first the principle working of tandem PV devices must be known. Tandem PV devices stack multiple cells on top

of each other. However, the cells have different energy band gaps. The advantage of this is that the each cell absorb in a certain part of the spectrum. The high band gap material will be on top as it absorbs the photons with the high energy and the low energy photons that pass through this material will then be absorbed by the cell below. The spectral information of the irradiance impinging on the cells becomes increasingly relevant. As the ITRPV projects increase of the market share of tandem PV devices which is shown in Figure 1.6. It can

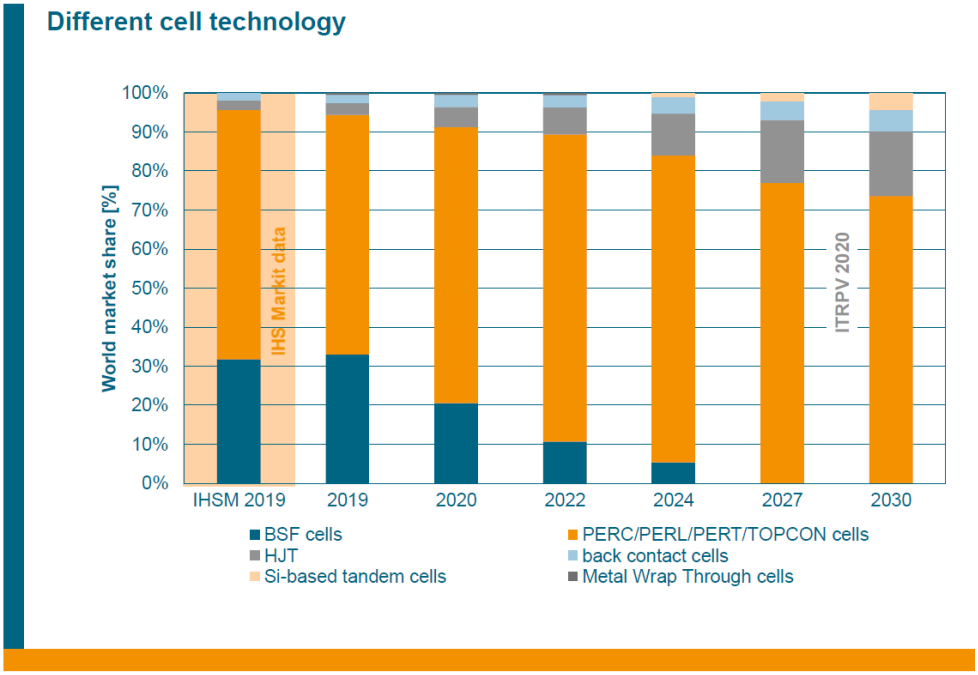

Figure 1.6: Market share of different PV technologies from 2020 to 2030 as projected by the ITRPV. Retrieved from [10].

be seen that the share of tandem PV is expected to increase up to 5% in 2030 compared to 0% in 2020. Making it relevant to develop models that are able to model the spectral properties of the incoming light.

The main focus of this thesis project is to develop a model framework that is able to model the irradiance on a PV system in complex environments, taking into account reflection and spectral information. The research questions that need to be answered to achieve this goal will be discussed in the next section.

1.2. Research Questions

To achieve the goal of this research the following research questions/objectives are formulated.

1. **What type of reflections do we need to model in order to accurately simulate the irradiance impinging on a PV module in a complex environment?**
   - *How do we accurately and efficiently model different reflective properties?*
   - *How do we calculate irradiance coming from different type of reflectors?*
2. **Create a model that is structured in a way that accelerates simulation.**
   - *Subdivide the model into decoupled blocks to allow efficient simulation.*
   - *Structure the model so that it allows us to perform spectrally resolved simulations and model surfaces with time dependent reflective surface properties.*
3. **How does the performance of the proposed model compare to measured data and existing models?**
   - *How does the model perform for cases where irradiance is mostly due to specular reflections?*
   - *How does the model perform over long periods of time for different orientations and weather conditions?*

Now that the main objectives of this thesis project are known the next section will discuss the structure of the report.

1.3. Thesis Structure

Before we dive into the subject matter of this thesis first this section will give an outline of how the thesis is structured.

Theoretical Background This chapter will give an explanation of necessary theoretical background information. This theoretical background information is crucial to understand the underlying principles of the thesis' work.

Existing Models This chapter dives into the models that are currently being used. The chapter will give an overview of their respective advantages and disadvantages. Also the modelling techniques and principles used in present models are important to understand because they lie at the basis of the proposed model framework. Therefore these techniques will be discussed as well.

Proposed Model Framework This chapter presents and explains the proposed model framework that is developed. The structure and techniques that are implemented will be discussed and the justification and reasoning behind it will be explained.

Experimental Setup And Validation This chapter will give an overview and explanation of the different experimental setups that are setup on the PVMD monitoring roof. Next to that it will give the results of the model validation compared to measurements as well as other present models.

Conclusions and recommendations This chapter is dedicated to summarising the answers the research questions stated before and drawing conclusions from the entire thesis' work and results. Additionally recommendations for future research and development will be given to finalize the thesis.

2

Theoretical Background

In this thesis, the goal is to model the irradiance on a PV module in complex environments. In an urban environment the irradiance on a system is dependent on a lot of different variables. Shading (which can be partial), different forms of reflection, transmission losses and so on contribute or decrease the irradiance on the system. The first part of this chapter will dive into the basics behind modelling irradiance on a PV module.

The irradiance on a PV module can be split into three different components as shown below: 2.1.

$$G_{\mathrm{m}} = G_{\mathrm{m}}^{\mathrm{dir}} + G_{\mathrm{m}}^{\mathrm{diff}} + G_{\mathrm{m}}^{\mathrm{refl}} \tag{2.1}$$

Splitting up the irradiance components like this is called the transposition model.

- $G_{\mathrm{m}}^{\mathrm{dir}}$ is the direct irradiance and can be seen as the component that travels directly from the sun in a straight line to the module.
- $G_{\mathrm{m}}^{\mathrm{diff}}$ is the diffuse irradiance is the radiation that after being scattered by molecules and particles like dust and clouds still reaches the module.
- $G_{\mathrm{m}}^{\mathrm{refl}}$ the reflected irradiance from either the ground or other surrounding surfaces. The optical properties of the surface will determine the direction and intensity of the reflected light.

A graphical representation of the different components of irradiance can be seen in Figure 2.1. There are a lot of different models to calculate the separate components of irradiance. A few models will be discussed in the next subsections. First, it is important to define the coordinate system that will be used throughout this thesis.

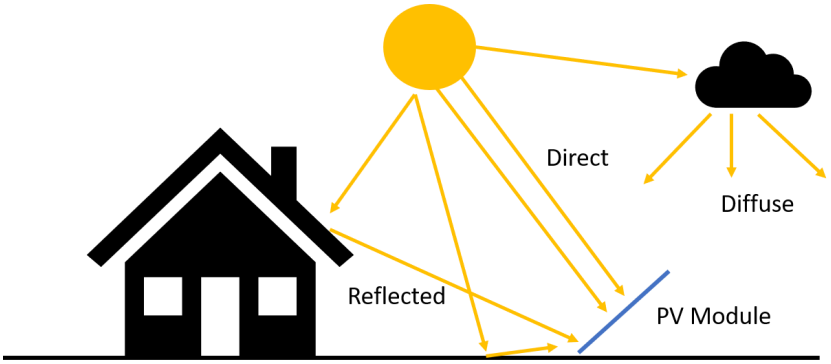

Figure 2.1: Graphical concept of different irradiance components on a PV module.

For convenience sake a spherical coordinate system will be used throughout this work to describe the geometries. The used coordinate system is shown in Figure 2.2. To understand the irradiance calculations for

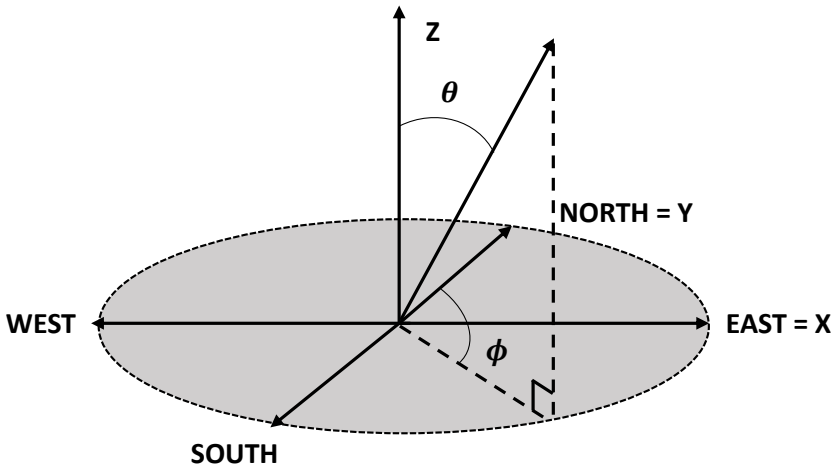

Figure 2.2: The used spherical coordinate system in terms of zenith (θ) and azimuth (ϕ) angle. The cardinal directions are as follows. The y direction in this diagram points in the North direction, negative y will be South. Therefore, positive x points into the East direction and negative x in the West direction. Azimuth will be measured East from North.

the different components first a section will be dedicated to elaborate on important concepts and quantities that are used throughout these calculations.

2.1. Radiometric Quantities

In order to get a clearer picture of the different concepts regarding irradiance below a list of important radiometric quantities and their explanation:

- **Radiant flux**: Radiant flux is the amount of radiant energy per unit time. It is expressed in Watts. The formal definition of the radiant flux is given in equation 2.2.

$$\phi_e = \frac{\partial Q_e}{\partial t} \tag{2.2}$$

  In this equation Q_e is the radiant energy emitted, t is the time ϕ_e is the radiant flux.

- **Irradiance**: Irradiance is the amount of radiant flux per unit area A. In the context of PV modelling it can be seen as the amount of solar power per unit area. The unit is W/m^2. The formal definition of irradiance is given in equation 2.3.

$$I = \frac{\partial \phi_e}{\partial A} \tag{2.3}$$

- **Radiance**: Radiance is the radiation received by a given surface per unit solid angle per unit of projected area. The formal definition is given in Equation 2.4.

$$L_{e,\Omega} = \frac{\partial^2 \phi_e}{\partial \Omega \partial A \cos\theta} \tag{2.4}$$

- **Luminance**: Luminance is a photometric measure of the luminous intensity per unit area of light travelling in a given direction. It is in similar to the concept of radiance however, it is weighted by the luminosity function of the eye. Often luminance is used when dealing with more of the visual side of light modelling compared to the quantitative side.

In a few of these quantities the unit of solid angle is mentioned. The next subsection will explain what a solid angle actually is.

2.1.1. Solid angles

In light and irradiance modelling very often the point of interest is taken with respect to a unit hemisphere surrounding that point of interest. In the case of PV irradiance modelling this point/position is on the surface of the solar cell.

The solid angle subtended by an object from a given point of view (apex) is (by definition) the area of the projection of the object on the unit sphere. The solid angle is expressed in the unit of steradian (sr). One steradian is when the area on the hemisphere is equal to the radius of the hemisphere squared[23]. The solid angle can be interpreted as a unit that gives a measure of what size a certain object or feature is perceived by an observer at the center of the sphere. The principle of a solid angle is graphically shown in Figure 2.3 Now that the concept of solid angle is known it is useful to elaborate on another important concept that often arises when dealing with irradiance calculations for both diffuse and reflected irradiance modelling. This concept is called 'the view factor'. This concept will be explained in the next subsection.

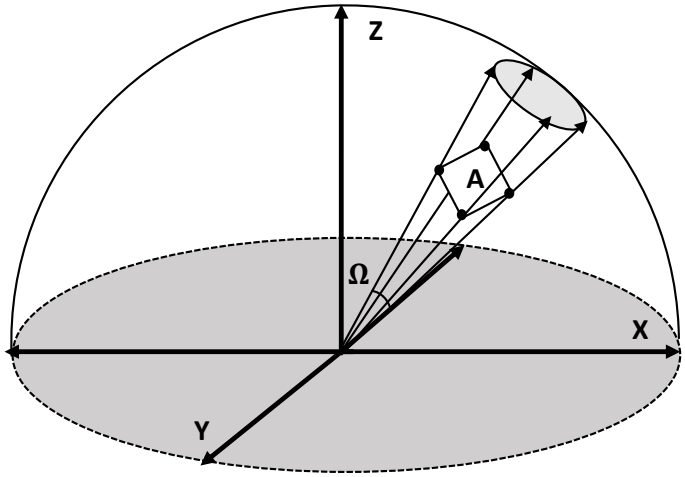

Figure 2.3: Schematic representation of the solid angle principle for surface A. The angle of the cone subtending that surface to the unit sphere equals the solid angle.

2.1.2. View factors

As mentioned before, the view factor is an important concept to calculate irradiance from both sky sections as well as from reflection from surfaces. The view factor can be described as the fraction of radiation leaving surface 1 that reaches surface 2. View factors assume isotropic scattering of radiation from all surfaces. The definition of the view factor for two surfaces A_1 and A_2 is given in Equation 2.5[8].

$$F_{1\to 2} = \frac{1}{A_1}\int_{A_1}\int_{A_2} \frac{\cos(\theta_1)\cdot\cos(\theta_2)}{\pi\cdot S^2}\mathrm{d}A_2\mathrm{d}A_1 \tag{2.5}$$

Where θ_1 and θ_2 are the angles between the surface normals and S is the distance between the surfaces. In Figure 2.4 a graphical representation of the parameters of the view factor between two differential surfaces is shown.

There are 3 important rules when dealing with view factors:

- **Reciprocity**: a pair of view factors is reciprocal. This means that the view factor of surface i to j can be related to the view factor from j to i. This can be done using Equation 2.6:

  $$F_{i\to j}\cdot A_i = F_{j\to i}\cdot A_j \tag{2.6}$$

  It can be seen that for two surfaces with equal areas the two view factors are equal. When this is not the case they can be related to each other by their area ratio.

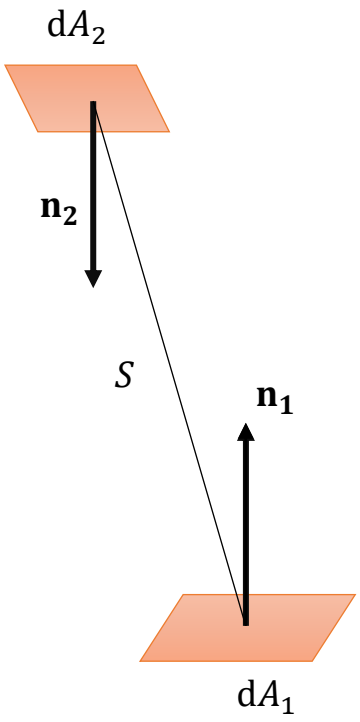

Figure 2.4: Graphic representation of the parameters of the view factor in the case of two differential surfaces.

- **Summation**: this rule comes from the conservation of energy and dictates that the radiation coming from a surface i will all be intercepted by the surroundings. Therefore, the sum of the view factors from surface i to all the surfaces around the i will equal unity. This can be formalized in Equation 2.7

$$\sum_{j=1}^{N} F_{i\to j} = 1 \tag{2.7}$$

  In this equation N is the number of surfaces surrounding surface i

- **Superposition** : this rule dictates that the view factor from surface i to j which consists of for example 2 parts a and b can be expressed as the sum of the view factor from i to a and i to b. This can formalized in Equation 2.8:

$$F_{i\to j(a,b)} = F_{i\to a} + F_{i\to b} \tag{2.8}$$

  This rule can be useful for geometries where a specific view factor is hard to calculate but the view factors to certain subsections of a surface can be calculated.

There are some crucial interpretation principles that are important in how view factors can be applied when modelling PV irradiance. How the view factor should be applied to calculate irradiance on a PV module will be formalized in a later section.

The next subsection is dedicated to the rendering equation which is the basic equation that underlies all light modelling esspecially in ray tracing models.

2.1.3. The Rendering Equation

The rendering equation is the most important equation in basic light modelling and is often used in 3D graphical rendering programs. It is useful to explore the concepts behind the rendering equation because it is derived from the principles of conservation of energy. This makes it a very fundamental physically relevant equation also from a PV modelling standpoint. The rendering equation is given in Equation 2.9[41].

$$L_o = L_e + \int_{\Omega} L_i \cdot \text{BRDF} \cos(AOI)\, \mathrm{d}\Omega_\mathrm{i} \tag{2.9}$$

n this Equation L_o is the out going radiance, L_e is the emitted radiance from the surface of interest and the last integral describes the reflected radiance which depends on the incoming radiance L_i and is weighted by the cosine of the angle between the surface normal and the incoming direction as well as the Bidirection Reflectance Distribution Function (BRDF). The exact definition of the BRDF will be given in the following subsection.

The integral basically sums all the incoming radiance from the hemisphere around the normal with corresponding weighing factors. This is why the integral is over the solid angle Ω to find the incoming radiance for all solid angles. The cosine factor is there for the same underlying reason as to why the direct irradiance decreases with the cosine of the angle of incidence. When calculating the incident irradiance for a particular source of interest this rendering equation is used as follows.

For a source of radiance that is not reflecting the incoming radiance there is no integral and the outgoing radiance $L_o = L_e$. Therefore, the irradiance hitting the surface of interest from that source will be $L_e \cdot cos(\theta) \cdot d\Omega_{\text{source}}$. Where θ is the angle with respect to the normal of the surface of interest. This principle is shown in Figure 2.5. In the case of a reflector of light that is reflecting the term L_e will be replaced by $L_i \cdot$ BRDF. The

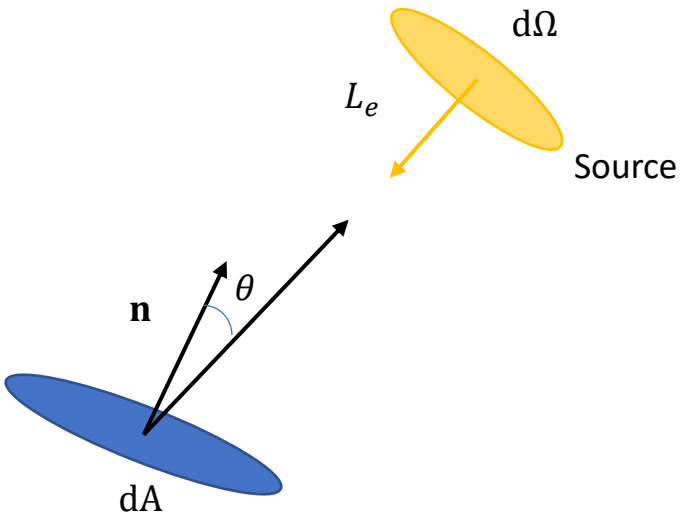

Figure 2.5: Graphic representation of the variables needed for calculating the irradiance from a light source using the rendering equation.

incoming L_i for the reflector needs to be calculated using the same principle as before. Integrating over all the incoming light sources which can in turn be emitting light sources or again reflectors one can find the integral and therefore the outgoing radiance.

However, one can see that a reflector at a certain position can affect the incident irradiance on another reflector and vice-versa. So to counteract the infinite loop that would occur if there was no limit an exit condition needs to be defined. This exit clause is implemented in ray tracing models by limiting the number of ray bounces that are allowed to occur. In this way the loop can be limited and the computation time controlled.

The rendering equation is the basis for all ray tracing models that exist and also the basis of how the rays are treated in the proposed model in this thesis.

2.1.4. Bidirectional reflectance distribution function

To characterization of the behaviour of light bouncing of a surface can be done using the BRDF. This BRDF quantitatively defines the 'shininess' of an object. As said before a material/surface can be diffuse or spec-

ular. But also anything in between. To be more precise the BRDF quantifies the radiance scattered into all directions from a surface illuminated by a source from any direction above the hemisphere of the material. The BRDF is given by equation 2.10[32].

$$\text{BRDF} = \frac{\partial L_o(\Omega_o)}{\partial E_e(\Omega_i)} \tag{2.10}$$

In fact it is the fraction of differential radiance outgoingL_o and differential irradiance incoming E_e[22]. The top part of this fraction can be written as Equation 2.11.

$$\partial L_o(\Omega_\text{o}) = \text{BRDF} \cdot L_\text{i} \cdot \cos(\theta_\text{i}) \text{d}\, \Omega_\text{i} \tag{2.11}$$

It can be seen when this differential radiance is integrated the second part of the rendering equation given in Equation 2.9 is obtained.

To elaborate on the bottom part of the BRDF fraction the differential irradiance can be seen as the amount of irradiance coming from a very small solid angle in the region around the incoming direction. This can be written as Equation 2.12.

$$\partial E_e(\Omega_\text{i}) = L_\text{i} \cdot \cos(\theta_\text{i}) \text{d}\, \Omega_\text{i} \tag{2.12}$$

So to summarize the BRDF is a way to relate the incoming irradiance to outgoing radiance. Because of this it is logical to see BRDF has the units of inverse steradian sr^{-1}.

Logically the BRDF is different for different surfaces and there are a number of different reflection mechanisms. These will be discussed later in this chapter.

Because the main important concepts and parameters are now known the explanation of the different components off irradiance will continue in the next section, starting with the direct irradiance.

2.2. Direct irradiance

The direct component of irradiance is the irradiance that comes from the sun directly and hits the PV module without any reflection or other disturbance. The direct component of irradiance can be computed using Equation 2.13:

$$G_\text{m}^\text{dir} = DNI \cos(AOI) \tag{2.13}$$

In this Equation *DNI* is the direct normal irradiance and *AOI* is the angle between the surface normal and the incident direction of the sunlight, often called the angle of incidence [35].

The *AOI* depends on the solar position in both azimuth and altitude. So, be able to model the irradiance the solar position must be known. Therefore, a solar position calculator is needed.

2.2.1. Solar position calculation

The input variables that are necessary to model the solar position accurately is the time and date and specific location on earth which is given in longitude and latitude[25]. The specific equations to find the azimuth and altitude of the sun with these inputs are lengthy and complicated and therefore will be left out of this thesis. These equations but can be found in [25] and [35].

To show the result of this calculator, Figure 2.6 shows 4 different sun paths for the center of Delft 3 months apart using this solar position calculator. This is also the solar position calculator used throughout this thesis.

2.3. Diffuse irradiance

There are numerous different methods to model the diffuse irradiance on a surface. Most calculations have one thing in common though. Because the diffuse light is the light coming from the sky. It must be known how much light comes from each part of sky. To find these values a model for the sky needs to be made. This model can basically be seen as a sky map that describes the radiance coming from each part of sky.

There are numerous different models describing these sky conditions. Each method has its underlying assumptions and principles. In the next section a selection of models will be described and discussed.

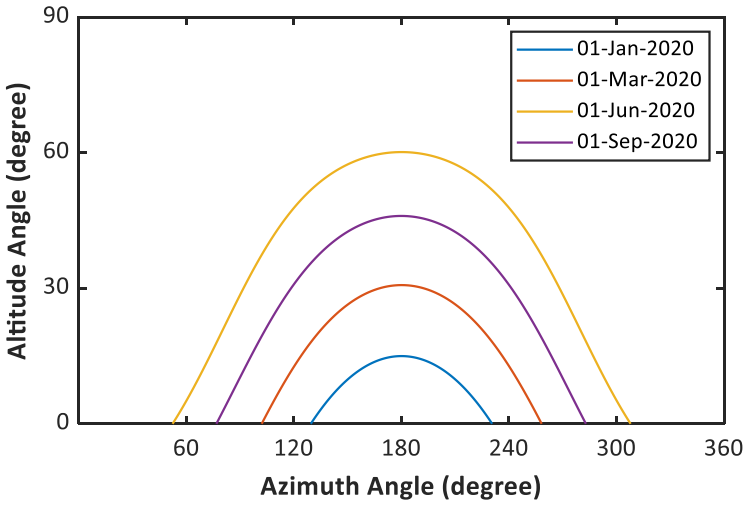

Figure 2.6: Path of the sun for 4 different days spread out over a year in Delft.

2.3.1. Isotropic sky model

The most basic method uses the underlying assumption that the sky brightness is the same for all parts of the sky. When calculating irradiance with this model the only thing that needs to be taken into account is 'how much of the sky is seen' by the surface of interest. This factor can be seen as the Sky View Factor or *SVF*. Equation 2.14 is then used to calculate the diffuse irradiance.

$$G_{\mathrm{m}}^{\mathrm{diff}} = DHI \cdot SVF \tag{2.14}$$

Where is *DHI* is the diffuse horizontal irradiance with no horizon obstruction. *SVF* is the sky view factor which gives a measure of how much of the sky is seen by the surface of interest. For a clear horizon it solely depends on the tilt angle(θ_{tilt} of the module and is given by Equation 2.15

$$SVF = \frac{1+\cos(\theta_{\mathrm{m}})}{2} \tag{2.15}$$

It can be seen that for a clear horizon and no tilt the *SVF* equals 1 which makes sense. As mentioned this model makes the assumption the brightness over the sky dome does not vary. This assumption is called the isotropic sky assumption. In reality the sky is not isotropic. Over the years different models have been developed to take into account for the anisotropic sky for example the Hay and Davis model. This model will be discussed in the next subsection.

2.3.2. Hay and Davis sky model

This model makes the assumption the sky an be subdivided into two parts. An isotropic section and a circumsolar section. The circumsolar section is the brightened area of sky just around the sun. The circumsolar section light direction will be the same as the *DNI* direction. The exact derivation of the equations governing the Hay and Davis model is outside the scope of this thesis. Only the fundamental equations will be discussed below[5].

First an anisotropic index is defined as in Equation 2.16

$$A_i = \frac{DNI}{E_a} \tag{2.16}$$

Where *DNI* is the direct normal irradiance and E_a is the extraterrestrial incoming radiation (i.e hitting the outside of the atmosphere). For the sky diffuse radiation then Equation 2.17 is formulated.

$$G_{\mathrm{m}}^{\mathrm{diff}} = DHI \cdot \left(A_i R_b + (1 - A_i) \cdot \frac{1+\cos(\theta_{\mathrm{m}})}{2} \right) \tag{2.17}$$

Where *DHI* is the diffuse horizontal irradiance. R_b is defined as $\frac{\cos(AOI)}{\cos(\theta_{\text{sun}})}$ where *AOI* is the angle of incidence, θ is the solar altitude and θ_m is the module tilt.

2.3.3. Reindl sky model

The Reindl model goes one step further than the Hay and Davis model because it also includes horizon brightening. The same anisotropic index is used as given by Equation 2.16[7].

The final equation for the sky diffuse radiation is then given by Equation 2.18[7].

$$G_{\text{m}}^{\text{diff}} = DHI \cdot \left[A_i \cos(AOI) + (1 - A_i) \cdot \frac{1 + \cos(\theta_{\text{m}}}{2} \left(1 + \sqrt{\frac{DNI \cdot \cos(\theta)}{GHI}} \sin\left(\frac{\theta_{\text{m}}}{2} \right)^3 \right) \right] \tag{2.18}$$

2.3.4. Perez Sky Model

The models mentioned before do account for uneven luminance but are not fully anisotropic. They divide the sky into different parts for which they specify the behaviour. The Perez model is different. The Perez Model developed by R. Perez in 1993 creates a radiance distribution for the sky which does not use the circumsolar or horizon section splitting as the models described before. Instead it is a fully anisotropic approach. There are multiple variations made over time but the basic idea will be explained in this section [27]. As the Perez Model will be used the explanation will be more in-depth compared to the previous models.

The framework of the model starts with a generalization of the CIE standard clear sky formula. The CIE general sky is allows calculation of luminance distribution under a wide range of occurrences from the overcast sky to cloudless situations without or with sunlight respectively[14]. The general model of the CIE general sky contains five coefficients *a*,*b*,*c*,*d* and *e* which can be tweaked to simulate different sky conditions. A number of standard skies, such as clear sky or fully overcast have their standard value for *a*,*b*,*c*,*d* and *e*. The relative luminance of a sky element, which is the ratio between the luminance of that sky element and an arbitrary reference element is given by Equation 2.19:

$$lv = f(\zeta, \gamma) = \left[1 + a \exp\left(\frac{b}{\cos(\zeta)} \right) \cdot [1 + c \cdot \exp(\mathrm{d}\gamma) + \mathrm{e} \cdot \cos^2(\gamma) \right] \tag{2.19}$$

In this equation ζ is the zenith angle of the sky element and γ is the angle between the sky element and the position of the sun. The coefficients a, b, c, d and e are coefficients to alter sky conditions. How these coefficients are implemented will be explained later.

The actual luminance can be calculated by normalizing it to the diffuse illuminance *Evd*. *Evd* needs to be either measured or modelled. The actual luminance of a sky element is then given by Equation 2.20

$$Lv = \frac{lv \cdot Evd}{\int_{\text{sky}} lv(\zeta, \gamma) \cdot \cos(\zeta) \mathrm{d}\Omega} \tag{2.20}$$

When the goal is to model irradiance on a PV module for a particular day these coefficients a, b, c, d and e are not known. This is where the Perez Model comes into play. The sky distribution needs to be defined by using the data that is present for that day. This is where the Perez Model comes into play.

As mentioned before the 5 coefficients are there to represent different sky conditions of the model. Each coefficient has their specific characteristics in how it affects the sky distribution. These characteristics are listed below:

- **Coefficient *a***: affects the amount of horizon darkening/brightening(darkening $-> a < 0$ and brightening $-> a > 0$). For example for overcast there is more darkening and for clear sky there is brightening of the horizon
- **Coefficient *b***: allows to adjust the gradient of the luminance near the horizon.
- **Coefficient *c***: adjusts the relative intensity of the region around the sun (i.e circumsolar region).
- **Coefficient *d***: can widen or narrow down the width of circumsolar region

- **Coefficient *e***: accounts for the relative intensity of back scattered light.

The work Perez has done is to find the coefficients needed for the CIE general sky formula using only the DNI and DHI as inputs. These can either be modelled using separate model or measured data. Then with using these inputs and the the solar zenith angle θ in radians the the variables sky clearness ϵ and sky brightness Δ can be calculated [28]. . The equations for ϵ and is given in Equation 2.21.

$$\epsilon = \frac{\left(\frac{DHI + DNI}{DHI}\right) + 1.041\,\theta^3}{1 + 1.041\,\theta^3} \tag{2.21}$$

The equation for Δ is given in Equation 2.22.

$$\Delta = \frac{mDHI}{DNI_0} \tag{2.22}$$

In these equations m is the optical airmass and Ees_0 is the normal extraterrestrial irradiance. Using the values found for ϵ and Δ the values for a, b, c, d and e can be found. Perez created a table for each coefficient with 8 rows and 4 columns. The row that is chosen for each coefficient is defined by the sky clearness ϵ. Each row represents a bin of ϵ values. Once the row is defined the coefficient values are calculated as follows. In this equation a is chosen as example coefficient.

$$a = a_1(\epsilon) + a_2(\epsilon)\theta + \Delta[a_3(\epsilon) + a_4(\epsilon)\theta] \tag{2.23}$$

In this equation a_1,a_2,a_3 and a_4 are the respective column values of the coefficient in the table. There are two exceptions for the coefficients c and d in the first ϵ bin. For coefficient c in the first ϵ bin equation Equation 2.24 is used.

$$c = \exp[(\Delta(c_1 + c_2\theta))^{c_3}] - c_4 \tag{2.24}$$

For coefficient d in the first ϵ bin equation Equation 2.25 is used.

$$d = -\exp[\Delta(d_1 + d_2\theta)] + d_3 + \Delta d_4 \tag{2.25}$$

So from the input DNI and DHI the coefficients of the CIE general sky are found. Then these coefficients can simply be input in the generalization formula and a radiance distribution is found.

Now different sky models are discussed which give us a radiance distribution for the sky. However from this sky distribution the diffuse irradiance on a surface needs to be calculated. How this is done will be explained in the next subsection.

2.3.5. Irradiance from diffuse anisotropic sky

To compute the irradiance on the module from the radiance distribution of the sky first it must be known that the irradiance is the sum of all the radiance coming from all directions. Equation 2.26[29] gives us the basic equation for the diffuse irradiance component falling on a horizontal surface:

$$G_{\mathrm{m}}^{\mathrm{diff}}(\theta_{\mathrm{tilt}} = 0) = \int_{\phi=0^\circ}^{\phi=360^\circ} \int_{\theta=0^\circ}^{\theta=90^\circ} R(\phi,\theta) \cdot \cos(AOI) \cdot \sin(\theta)\mathrm{d}\phi\mathrm{d}\theta \tag{2.26}$$

In this equation ϕ is the azimuthal angle and θ the altitude angle. The cosine of the angle of incidence accounts relies on the same principle as the direct irradiance calculation. $R(\phi,\theta)$ is the radiance from the particular sky sector corresponding to the angles θ and ϕ. The factor $\sin(\theta)\mathrm{d}\phi\mathrm{d}\theta$ is the differential solid angle $\mathrm{d}\Omega$ [29] and accounts for the perceived size of the sky sector considered. This can basically be seen as the view factor from the sky patch.

Two planes can be chosen as reference. One approach is taking the module plane as the reference plane and the other is taking the horizontal plane as the reference plane. The method explained in this section takes the horizontal plane as the reference plane. For a tilted surface of interest a few correction factors will come into play that can be inserted into 2.26. The correction factors that are present in Equation 2.26 can be split up into 3 principles [29]:

- **Incidence effect *i***: The incidence effect is the cosine of the angle of incidence factor. This angle can be calculated by calculating Equation 2.27.

$$\cos(AOI) = \frac{\mathbf{n}_{\text{cell}} \cdot \mathbf{s}}{|\mathbf{n}_{\text{cell}}| \cdot |\mathbf{s}|} \tag{2.27}$$

  This factor is always present so for both reference planes. In this equation $\mathbf{n}_{\text{cell}}$ is the normal vector to the receiving plane/cell and $\mathbf{s}$ is the vector that points to the radiance source.

- **Dilation effect *j***: this corresponds to the factor $\sin(\theta)$. This factor compensates for the increasing azimuth-arc length from a certain solid angle when the altitudal angle (θ) of the solid angle increases.

- **Accessibility factor *k***: This factor can either be 0 or 1 and compensates for the fact that when a plane is tilted not all radiances can reach the plane.

2.4. Reflected Irradiance

Reflected irradiance is the most complex component of irradiation to model. This section will dive into the different mechanisms and methods to model the reflected irradiance.

The most basic model is using equation 2.28 [35].

$$G_{\text{m}}^{\text{refl}} = GHI \cdot \alpha(1 - SVF) \tag{2.28}$$

In this equation *GHI* is the Global Horizontal Irradiance which is the sum of the *DHI* and the $G_{\text{m}}^{\text{dir}}$ (from Equation 2.13) This method assumes a constant reflectivity for all surrounding surfaces. Also this model only takes into account horizontal surfaces which are all illuminated evenly. This does not take into account the shading that can occur with more complex geometries. Also it does not take into account different reflection mechanisms. Because reflection is different for each material. To summarize this model is not very accurate and uses a lot of simplifications.

To understand more complex methods for calculating irradiance first it is useful to look at different mechanisms of reflection. There are three different types of reflection: diffuse, specular and mixed. The basic idea of the different reflection types can be seen in Figure 2.7.

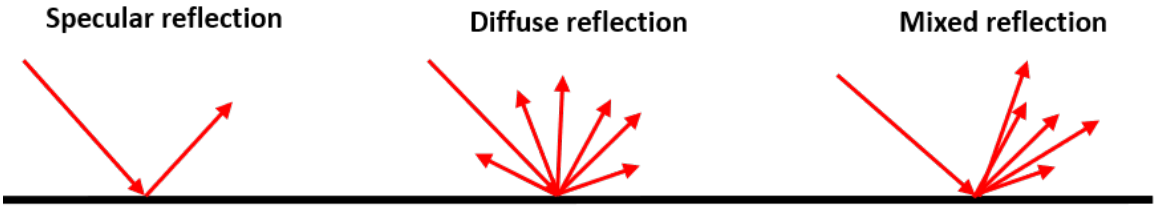

Figure 2.7: Specular, diffuse and mixed reflection shown in a schematic manner[9].

2.4.1. Diffuse reflections

Diffuse reflection is the reflection such that a single ray is scattered in different angles contrary to specular reflection where it reflects at only one angle. A perfect diffuse reflector displays lambertian reflection. Which will be discussed in the following paragraph.

Lambertian Model

The way a lambertian surface reflects can be interpreted in different ways and therefore be confusing. This paragraph will discuss the way a lambertian reflector should be interpreted.

Each point of a lambertian surface reflects the light intensity in a cosine pattern. This principle is shown in Figure 2.8. This principle leads to an interesting property of a lambertian reflector.

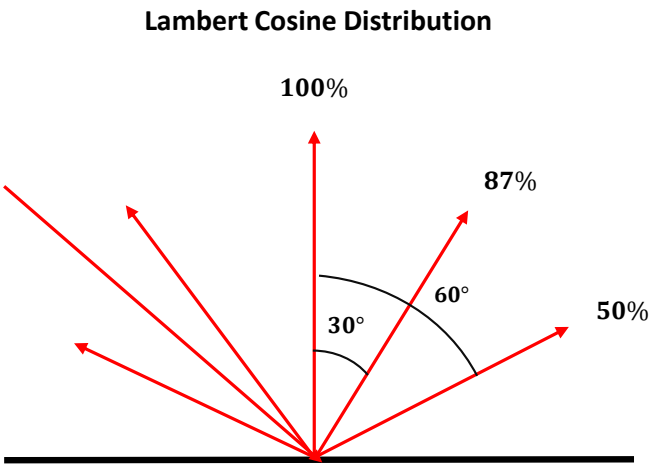

Figure 2.8: Lambert cosine distribution.

When looking at the surface as an observer, the area of the surface which is seen by the observer is proportional to $\frac{1}{\cos(\theta)}$. The radiance that is measured/seen comes from the the reflected intensity from each point. That radiance is proportional to $\cos(\theta)$ times the number of points seen which is proportional to $\frac{1}{\cos(\theta)}$, and therefore the radiance is independent of θ. Thus the measured reflected radiance is *independent of the viewing direction*. The BRDF of a lambertian reflector will therefore be *constant*. To find this BRDF first the reflectivity must be of a surface must be mathematically defined. Real Time Rendering 4th Edition [13] defines this as the amount of light reflected along a given direction for incoming light in any direction in the hemisphere around the surface normal[11]. This can be written as Equation 2.29.

$$\rho = \int_{\theta=0}^{\frac{\pi}{2}} \int_{\phi=0}^{2\pi} \text{BRDF}_{\text{lambertian}} \cdot r^2 \cdot \cos(\theta) \cdot \sin(\theta) \text{d}\theta \text{d}\phi \tag{2.29}$$

In this equation ρ is the reflectivity of the surface. Assuming unit length vectors and therefore $r = 1$ Equation 2.29 can be rewritten to equation 2.30

$$\rho = \text{BRDF}_{\text{lambertian}} \int_{\theta=0}^{\pi 2} \sin(\theta)\cos(\theta)\text{d}\theta \int_{\phi=0}^{2\pi} 2\pi \text{d}\phi \tag{2.30}$$

Working out this equation one can derive Equation 2.31

$$\rho = \text{BRDF}_{\text{lambertian}} \cdot \pi \tag{2.31}$$

Therefore, for the BRDF we can write Equation 2.32

$$\text{BRDF}_{\text{lambertian}} = \frac{\rho}{\pi} \tag{2.32}$$

In this equation ρ is the reflectivity of the surface. When the BRDF is known the reflective behaviour of the surface is defined and the outgoing radiance of this surface can be calculated based on the incoming radiance.

However, lambertian reflection does not occur for all surfaces. Concrete, ceramic and cloth for example display reflection that can be more accurately modelled using the Oren-Nayar reflection model which will be explained in the following paragraph.

Oren-Nayar Model

The Oren-Nayar model has similarities to the lambertian reflector model. It differs in the sense that it uses the microfacet model, introduced by Torrance and Sparrow [38]. This microfacet model assumes each surface consists of infinitesimally small Lambertian scatterers[16].

The exact derivation and properties of the Oren Nayar-model is outside the scope of this thesis. However, the BRDF of Oren-Nayar reflection is given in Equation 2.33.

$$\text{BRDF}_{\text{Oren-Nayar}} = \frac{\rho}{\pi}(A + \sin(\alpha) \cdot \tan(\beta) \cdot \gamma \cdot B) \tag{2.33}$$

Where the value of A is given by Equation 2.34

$$A = 1 - 0.5\frac{\sigma^2}{\sigma^2 + 0.33} \tag{2.34}$$

The value B is given by Equation 2.35.

$$B = 0.45\frac{\sigma^2}{\sigma^2 + 0.09} \tag{2.35}$$

In Equation 2.33 α will the the maximum inclination angle of either the incoming irradiance or outgoing radiance, β is the minimum azimuthal angle of the incoming irradiance or outgoing radiance. γ is the maximum between zero and the azimuthal angle difference between incoming irradiance and outgoing radiance. The most noteworthy aspect about this model is that this BRDF is not isotropic and the intensity of the reflected light will be dependent on the viewing angle. This is a crucial difference from the Lambertian BRDF.

2.4.2. Specular reflections

A distinction between the model that will be presented in this thesis and a lot of current models is the fact that it will also take into account the effect of specular reflections. The math behind direct reflections will be described in this section.

The incoming angle of light of a ray will be reflected with the same outgoing angle and a part of the light will be transmitted through the surface. The intensity of the reflected ray will decrease by a reflection coefficient given by the Fresnel equations described in Equation 2.36. For a perfect mirror this Fresnel coefficient will be 1 as there will be no transmitted light. For S- and P-polarized light respectively the Fresnel coefficients are:

$$\begin{aligned} R_s &= \left[\frac{n_1\cos(\theta_i) - n_2\cos(\theta_t)}{n_1\cos(\theta_i) + n_2\cos(\theta_t)}\right]^2 \\ R_p &= \left[\frac{n_1\cos(\theta_t) - n_2\cos(\theta_i)}{n_1\cos(\theta_t) + n_2\cos(\theta_i)}\right]^2 \end{aligned} \tag{2.36}$$

In this equation θ_i is the incoming angle and θ_t is the transmitted angle which can be found using Snell's law. This relation is given in Equation 2.37.

$$\theta_t = \arcsin\left(\sin(\theta_1) \cdot \frac{n_1}{n_2}\right) \tag{2.37}$$

For sunlight it can be most often assumed that it the light is unpolarized and then the reflection coefficient can be written as:

$$R = \frac{R_s + R_p}{2} \tag{2.38}$$

For computational reasons sometimes the Schlick approximation is made for calculating the Fresnel reflection coefficients. Schlick presented a work in which he proposes Equation 2.39[17].

$$R_{\text{schlick}}(\theta_i) = R_0 + (1 - R_0)(1 - \cos(\theta_i)^5 \tag{2.39}$$

In this equation R_0 is given by Equation 2.40

$$R_0 = \left(\frac{n_1 - n_2}{n_1 + n_2}\right)^2 \tag{2.40}$$

In this equation n_1 is the refractive index of the first medium and n_2 of the second medium. The Schlick approximation must be altered when $n_1 > n_2$ or the approximation fails. The θ_i must then be replaced with θ_t[17]. This approximation can be up to 30% faster than the conventional Fresnel equations.

The way the Fresnel coefficients vary for different angles of incidence from air(n=1) to glass (n=1.5) can be seen in Figure 2.9. Also the Schlick approximation is added in this figure. Similarly as to the lamber-

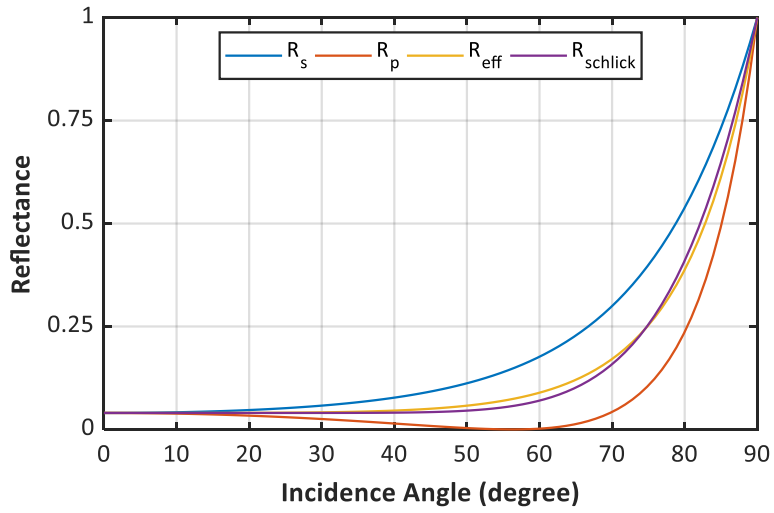

Figure 2.9: Fresnel coefficients for different angles of incidence from air to glass.

tian surface a BRDF can be defined for the specular surfaces. As mentioned before the BRDF quantifies the radiance scattered into all directions from a surface illuminated by a source from any direction above the hemisphere of the material. This is given by Equation 2.10 on page 12. Because the light only is reflected into one direction, namely the one where the angle of incidence is the same as the angle of reflection as shown in Figure 2.10. The BRDF of specular surface can be described by simply two Dirac functions as given in

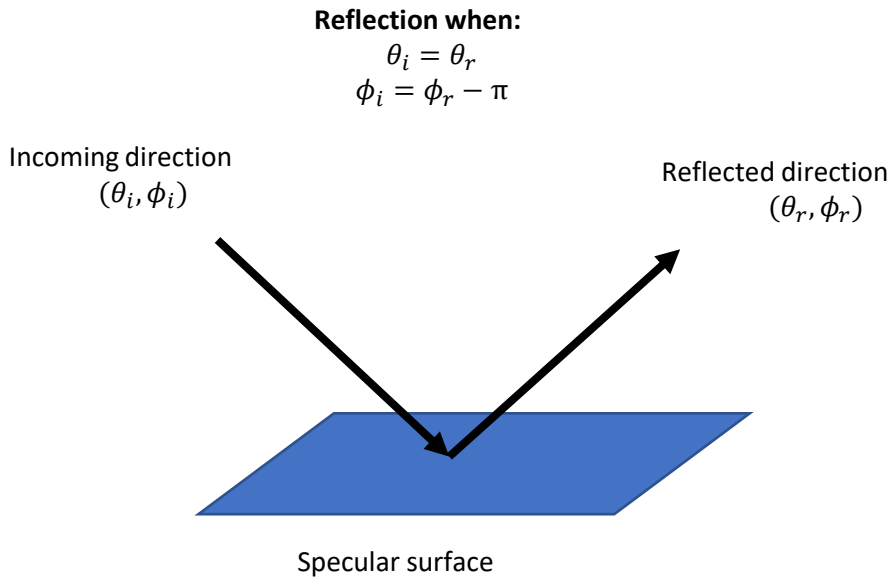

Figure 2.10: Required conditions for occurrence of specular reflection on a certain location.

Equation 2.41[1].

$$\text{BRDF}_{\text{specular}} = R \cdot \delta(\theta_i - \theta_r) \cdot \delta(\phi_i + \pi - \phi_r) \tag{2.41}$$

Where θ_i and ϕ_i are the incoming altitudal and azimuthal angle of the ray. Whereas θ_r and ϕ_r is the altitude angle and azimuthal angle of the reflected ray. And again when the BRDF is known the reflective behaviour of the surface is defined and the outgoing radiance of this surface can be calculated based of the incoming radiance.

As mentioned before in the view factor subsection there is a critical way in which view factors should be interpreted and handled to calculate the irradiance. The next section will discuss this interpretation.

2.5. How to apply view factors for calculating irradiance

As explained before a view factor can be used for surfaces or sky patches that isotropically emit/reflect light. So for perfect Lambertian surfaces the approach in this section can be used. In order to look at the irradiance that reaches the module first it is crucial to know how much radiation leaves a certain surface j. This can be described by the broader term radiosity. Radiosity is the radiant flux leaving (emitted, reflected and transmitted by) a surface j per unit area [2] and is given by Equation 2.42:

$$J = J_{\text{e,em}} + J_{\text{e,refl}} + J_{\text{e,tr}} \tag{2.42}$$

In this equation J_{em} is the emitted radiosity, J_{refl} the reflected light and J_{tr} the transmitted light. For example for a sector of sky the radiosity will only consist of emitted light J_{em} as there is no reflected nor transmitted light.

Now to calculate the irradiance on a PV module it is useful to look at the amount of radiant energy it receives from surface j. The amount it receives will be equal to the radiant energy coming from the surface j times the view factor $F_{j\to i}$ from j to i. And it can also be expressed as the irradiance E_j times the area of the surface i. This equality is shown in Equation 2.43:

$$E_{j\to i} \cdot A_i = F_{j\to i} \cdot A_j \cdot J_{e,j} \tag{2.43}$$

Now the irradiance, radiant energy per unit area , coming from surface j reaching module i can then be described by Equation 2.44 by dividing both sides by A_i:

$$E_{e,j\to i} = \frac{F_{j\to i} \cdot A_j \cdot J_{e,j}}{A_i} \tag{2.44}$$

Now this is for a single surface j. To calculate the total irradiance E_i incident on surface i coming from N surfaces Equation 2.45 can be derived:

$$E_i = \frac{\sum_{j=1}^{N} F_{j\to i} \cdot A_j \cdot J_j}{A_i} \tag{2.45}$$

Now using the reciprocity rule from Equation 2.6 this can be rewritten to Equation 2.46

$$E_{e,i} = \sum_{j=1}^{N} F_{i\to j} J_{e,j} \tag{2.46}$$

So to conclude it can be seen that to calculate the irradiance on the module surface i the view factor from module to surface $F_{i\to j}$ can be used to calculate this.

To expand on this further to translate this to a differential part of a module receiving diffusely reflected light from a differential surface. The first step to calculate this can be seen in equation 2.47.

$$G_{dA_M} = \int_R dG_{dA_M} = \int \alpha \cdot G_{dR} \cdot \frac{dA_R}{dA_M} dF_{R\to A_M} \tag{2.47}$$

This can then be expanded using the same reciprocity rule as mentioned before to Equation 2.48:

$$G_{dA_M} = \int \alpha \cdot G_{dR} \cdot dF_{A_M\to R} \tag{2.48}$$

Now looking back at the section that discussed the sky view factor in the subsection about the diffuse irradiance: this sky view factor can be seen as the sum of the view factors of the sky patches to the module as shown in Equation 2.49

$$SVF = \sum_{i=1}^{N} F_{M \to S_i} \tag{2.49}$$

Where M is the module, S_i the sky patch and N the total number of visible sky patches. Graphically the principle is shown in Figure 2.11. For an obstructed horizon it is shown in Figure 2.12.

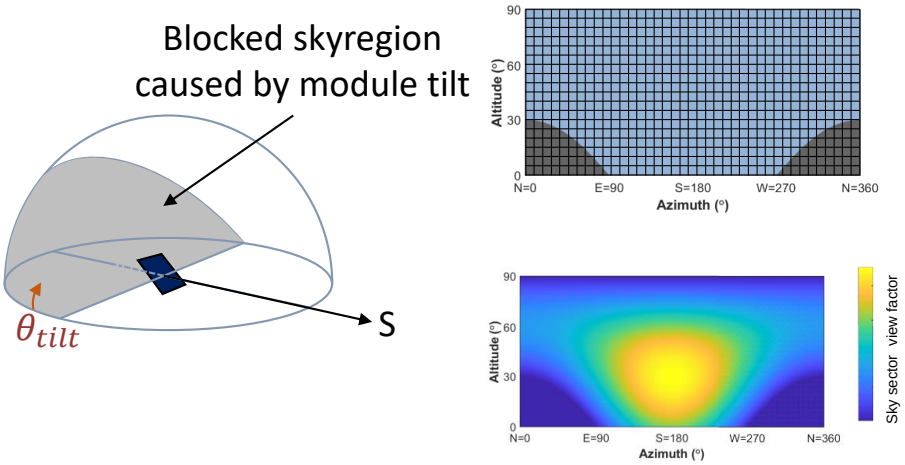

Figure 2.11: Graphical representation how the SVF is constructed of the sum of the view factors of the individual patches in case of a free horizon

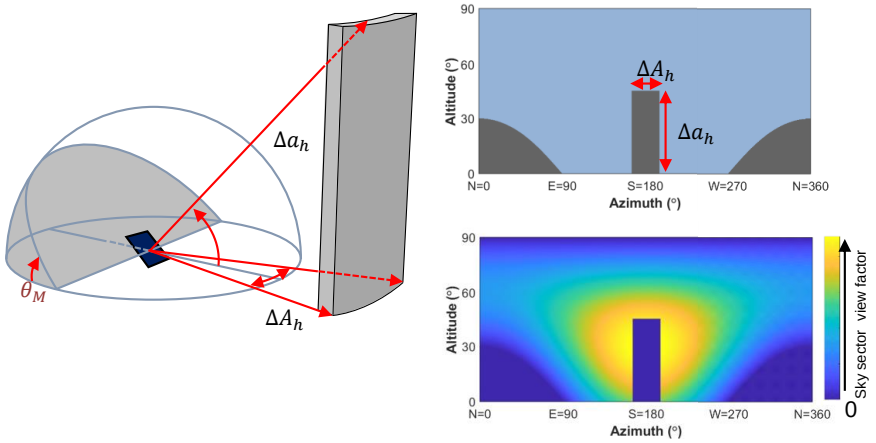

Figure 2.12: Graphical representation how the SVF is constructed of the sum of the view factors of the individual patches in case of a blocked horizon.

2.6. Albedo vs Reflectivity

In the previous sections the principle of reflectivity has been mentioned numerous times. However in literature often the name albedo is used for the same purposes. As in literature there are a different ways these variables are interpreted this subsection is dedicated to clarify the differences in these properties and how they will be interpreted in this thesis.

To start it's useful to define the fundamental principle of albedo as used in this thesis. The definition of albedo is the fraction of solar radiation reflected by an environment. So it is not a surface property but more an environmental property which takes into account the amount reflected by each individual surface or body. The albedo will therefore not vary for different wavelengths as it is an integration of the entire solar spectrum.

When measuring the albedo of a certain location in practice two pyranometers will be used one facing to the sky the other facing to the ground. Dividing the incoming radiation on the bottom pyranometer by the incoming radiation on the bottom pyranometer will give the albedo. There is a fundamental inaccuracy in this approach. The irradiance on the top pyranometer can be influenced by surfaces and environment as well. A building can reflect irradiance on the top pyranometer and increase the incoming irradiance on the top pyranometer. For the albedo of a free horizon α_{FH} this approach will be accurate. To formalize this albedo principle mathematically assuming only lambertian surface Equation 2.50 can be derived.

$$\alpha_{\text{FH}} = \frac{\int\int G(\lambda,\mathbf{x})\, R(\lambda,\mathbf{x})\, dF_{dA\to S}\, d\lambda}{\int G(\lambda) d\lambda} \tag{2.50}$$

In this equation $G(\lambda,\mathbf{x})$ is the incoming spectrum on a surface at position $\mathbf{x}$, $R(\lambda,\mathbf{x})$ is the reflectivity of that specific surface for each specific wavelength and $dF_{dA\to S}$ is the view factor from that surface to the surface of interest.

This approach only works for lambertian surfaces because then the view factor can be used for each surface. When mixed and specular surfaces are considered the BRDF will need to be used. If the BRDF is used the reflective properties also depend on the angle of incidence and therefore the position of the sun. One can imagine that the integration will get increasingly complex. Therefore, the principle of how it is measured and using that albedo for an environment works better than solving the integration analytically.

The difference between albedo and reflectivity can be seen from how the different principles are used in the equation above. Whereas albedo is the fraction of reflected solar radiation which takes into account the entire spectrum and all the different surfaces, the reflectivity can be seen as the ability of a surface to reflect light for each wavelength.

The spectrum $G(\lambda)$ which can often be seen as the incoming spectrum is the AM1.5 spectrum shown in Figure 2.13. Up until now the modelling of the light up until it hits the PV cell is only considered. However, when it hits the PV panel or cell it needs to travel through glass before hitting the actual effective material. To calculate losses happening in this region incidence angle modifiers are used. The working of these will be explained in the next subsection.

2.7. Incidence Angle Modifiers

When simulating radiation impinging on solar panel often an incidence angle modifier (*IAM*) is added which accounts for the loss of power due to the angle of the light coming in. These modifiers are only necessary when dealing with PV cells or modules and not for a sensor like a pyranometer. It can be seen as the fraction of the transmittance at an angle θ $\tau(\theta)$ and the normal transmittance$\tau(0)$ shown in Equation 2.51[6].

$$IAM(\theta) = \frac{\tau(\theta)}{\tau(0)} \tag{2.51}$$

The cosine factor ($\cos(AOI)$) alone is not enough. This is due to the fact there will also be loss of power due to travel through the glass plane in front of the module. Depending on the thickness and properties of the glass the *IAM* will vary. A few models that calculate the *IAM* will be discussed in this section.

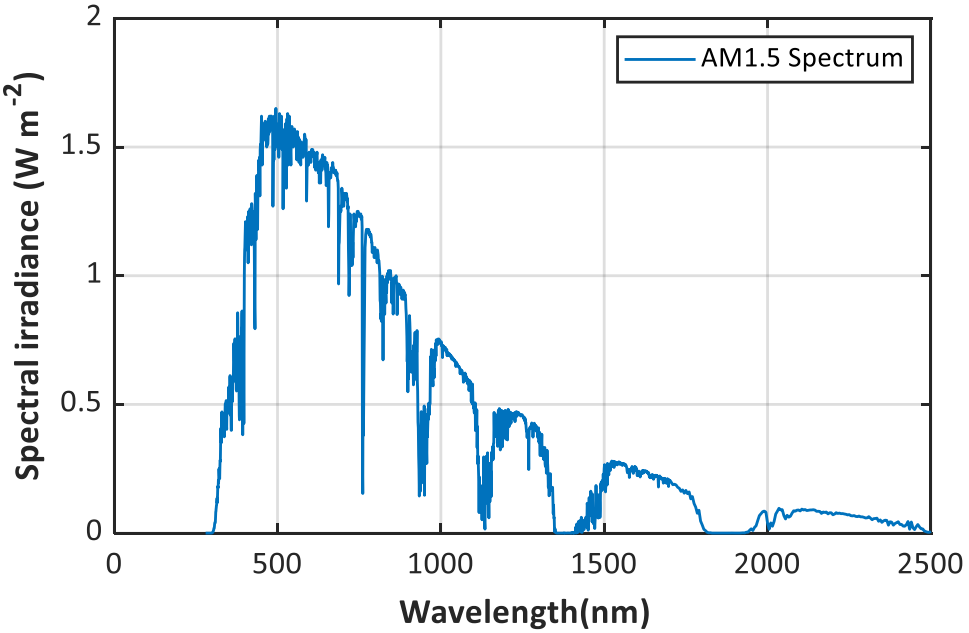

Figure 2.13: The solar AM1.5 spectrum.

2.7.1. ASHRAE IAM model

The most basic approach for calculating the IAM was proposed by Souka and Safat (1966) [4] and then adopted by the American Society of Heating, Refrigeration and Air Conditioning (ASHRAE). For this case the *IAM* is given by Equation 2.52.

$$IAM = 1 - b_0 \left(\frac{1}{\cos(\theta_{AOI})} - 1 \right) \tag{2.52}$$

The dependency on the angle of incidence for this *IAM* model is shown in Figure 2.14 for two different values of b_0.

2.7.2. Physical IAM model

The second model that will be discussed is a physical model based on Snell's and Bougher's law [36]. First the angle of refraction is calculated using Snell's law. Both reflective losses at both interfaces of the glass plane are calculated using the Fresnel coefficients. The transmittance τ at angle θ for a glass with extinction coefficient K and thickness L is then found to be given by Equation 2.53.

$$\tau(\theta) = \exp\left(\frac{-K \cdot L}{\cos(\theta_r)} \right) \left(1 - \frac{1}{2} \left(\frac{\sin(\theta_r - \theta)^2}{\sin(\theta_r + \theta)^2} + \frac{\tan(\theta_r - \theta)^2}{\tan(\theta_r + \theta)^2} \right) \right) \tag{2.53}$$

By finding the limit for which $\theta \to 0$, $\tau(0)$ can be found. The result of this limit is given in Equation 2.54.

$$\tau(0) = \exp(-K \cdot L) \left(1 - \left(\frac{1-n}{1+n} \right)^2 \right) \tag{2.54}$$

The dependency on the angle of incidence for this physical *IAM* model is shown in Figure 2.15.

2.8. Summary

This chapter has given an overview of the physics behind irradiance modelling. Many different principles which are relevant to light modelling principles such as solid angles and view factors have been discussed. Different types of light reflection and the way they can be modelled have been described and explained.

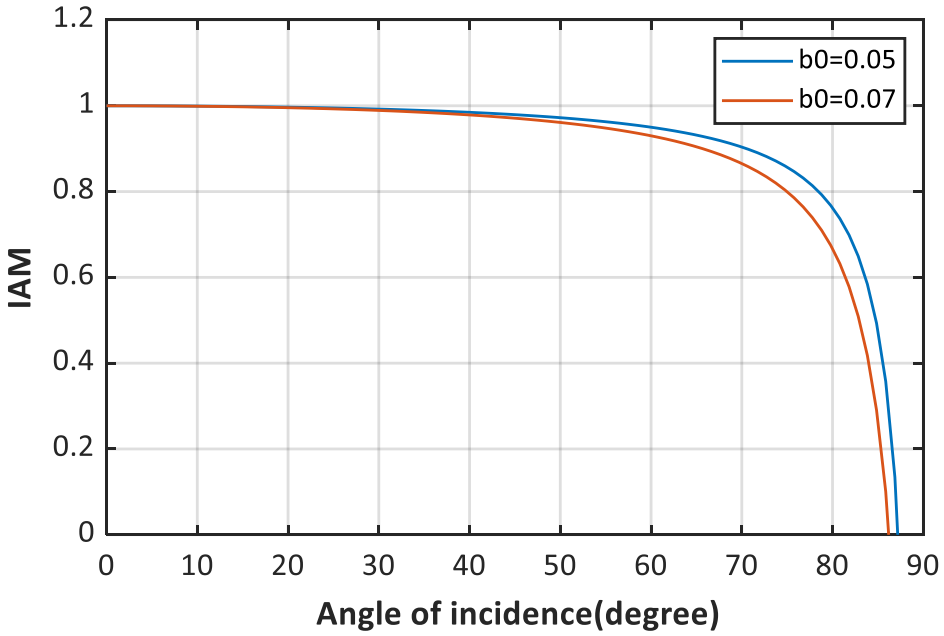

Figure 2.14: Incidence angle plotted to the incidence angle modifier (*IAM*) for the ASHRAE *IAM* model with two different values for b_0.

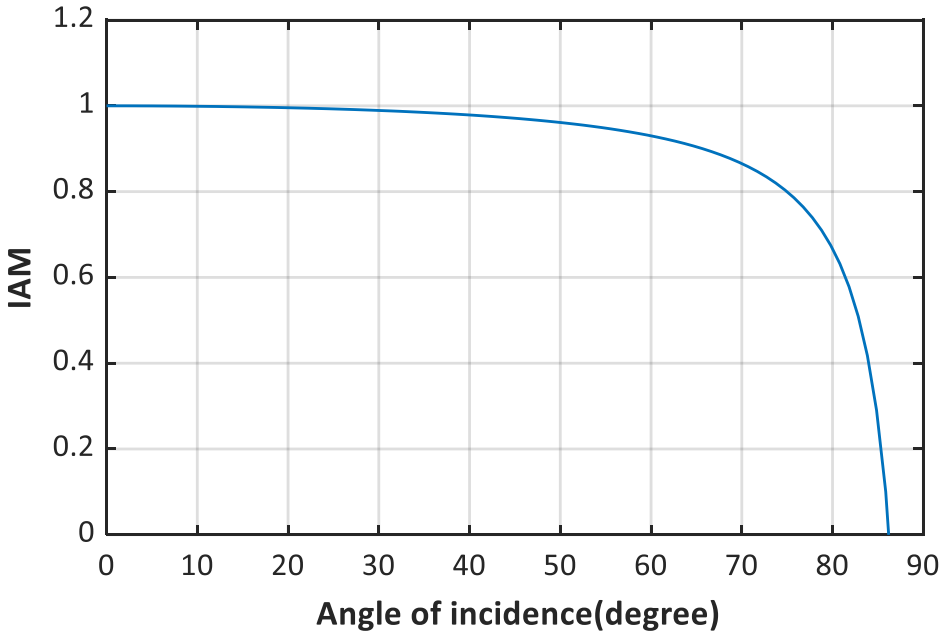

Figure 2.15: Incidence angle plotted to the Incidence angle modifier (*IAM*) for the physical model as proposed by Soto et al. [36].

3

Existing Irradiance Models

There are multiple models to simulate irradiance on a PV module. Currently there are two fundamentally different approaches that are being used. The first one uses view factors and the second one uses ray tracing. The fundamentals, differences and currently applied models will be discussed in this chapter. First a quick summary will be given below:

- **View factor**: As mentioned before a view factor can be seen as the fraction of irradiance reflected from a certain surface that reaches another surface. This modelling framework assumes each surface will scatter light isotropically (i.e lambertian reflection). The final irradiance on a module can then be found by integrating over all the surrounding surfaces. The advantage of this method is that the model is based on closed analytic formulas making it a computationally efficient and relatively fast method. In complex geometries however the accuracy of the view factor method reduces and often ray tracing is used. View factor models are a good option for setups with a relatively free horizon.
- **Ray tracing**: these types of models calculate the individual behaviour of each ray and their respective reflected rays. The final irradiance will be the sum of the irradiance of the rays reaching the module. The ray tracing models can be further subcategorized into forward- and backward ray tracing. A principle which will be explained later in this chapter.

3.1. View Factor Models

View factor models are present in numerous different ways. Because view factors can be calculated analytically for simple geometries they are very attractive for these bifacial power plants. Because the ground is often the only surface reflecting irradiance to the backside for these plants the view factors can be calculated relatively fast and this calculation is limited in its complexity. The ground reflected irradiance can then be calculated using the view factors to the sectors of the ground. Often the *GHI*,*DHI* and albedo and an irradiance model is used to calculate the irradiance on the front and back of a panel [24].

One option to model the ground reflected irradiance configuration factors, which are actually the same as 2D-view factors[21]. One of the methods mentioned by Marion et al. describes how the ground reflected can be calculated using a configuration factor by using Equation 3.1.

$$G_{\text{gr,refl}} = \alpha \cdot GHI \cdot \left(\frac{1 - \cos(\beta)}{2} \right) \tag{3.1}$$

The incoming irradiance on the ground is assumed to be *GHI* (the global horizontal irradiance), α is the ground albedo and β is the PV module tilt as measured from the horizon. The configuration factor in this equation is $\frac{1-\cos(\beta)}{2}$. The assumption is that all the radiation incident on the ground is the same (namely the GHI). This is not true in reality as the shadows of the modules will disrupt the intensity of light incident on the ground and therefore the reflected irradiance as well. Applying configuration factors separately for the unshaded and shaded parts of the ground is the way to counteract the effect of shading. This is exactly what Marion et al. proposed in their work.

Marion et al. presented a model to take into account this disruption [21]. To solve this problem the ground is divided into unshaded and shaded areas. They also added additional accuracy for the incident irradiance on the ground. Instead of assuming the GHI they used a more complex sky model. Using the Perez model for the diffuse component, splitting it up into a circumsolar I_{cir}, sky I_{sky} and horizon I_{hor} component, the irradiance incident ($G_{\text{gr,inc}}$ on the ground will be given by Equation 3.2.

$$G_{\text{gr,inc}} = a \cdot (DNI + I_{\text{cir}}) + CF_{\text{sky}} \cdot I_{\text{sky}} \tag{3.2}$$

In this equation a is the cosine of the sun zenith angle for unshaded segments. For shaded segments it will be multiplied with the fraction of opening of the PV array due to gaps [21]. The horizontal I_{hor} can be ignored for the ground. The CF_{sky} can be found using Equation 3.3.

$$CF_{\text{sky}} = \frac{1}{2}(\cos(\theta_{s1}) - \cos(\theta_{s2})) \tag{3.3}$$

The variables are defined as shown in Figure 3.1. Now that the irradiance received by the ground is known the

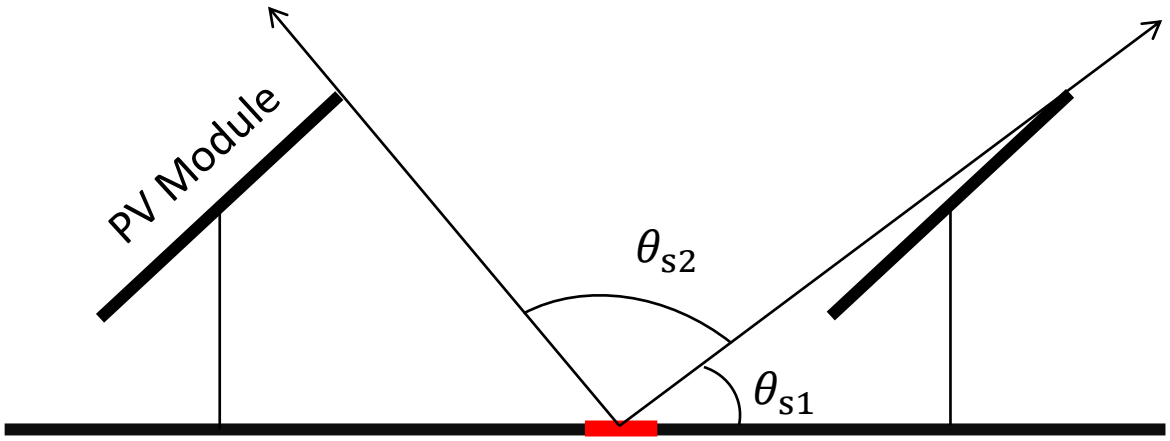

Figure 3.1: Schematic representation of the view angle from sky to ground and the variables that are needed to calculate Equation 3.3[21].

backside irradiance can be calculated. This will be the sum of the irradiance coming directly from the sky, the ground reflected irradiance and the reflected irradiance from the modules behind. For the modules behind Marion et al. [21] decided to only take into account the diffusely reflected irradiance. Due to geometrical reasons it is unlikely the specular reflections of the direct/circumsolar component will ever hit the backside of the PV module.

The diffuse component for the backside irradiance is calculated by adding up 180 degree segments and multiply the irradiance for each segment with its respective CF and a angle of incidence correction[21]. The final equation for the back side irradiance is given in Equation 3.4.

$$BSI = b \cdot F_b \cdot (DNI + I_{\text{cir}}) + \sum_{i=1}^{180^\circ} CF_i \cdot F_i \cdot I_i \tag{3.4}$$

In this equation b is the positive $\cos(AOI)$, F_b is an added angle of incidence modifier as proposed by Sjerps-Koomen et al. [34] similar to the angle of incidence modifiers discussed in the previous sections.

There are more methods to incorporate view factors in modelling irradiance on a PV panel: For example Nussbaumer [24] presented a work which describes a model for bifacial panels as follows. The direct irradiance modelling on the front and back of the panel are calculated using the geometrical properties explained in the previous chapter. The diffuse irradiance is done using the Perez model. The ground reflected irradiance is modelled using 'a quasi 3D view factor concept' as previously used by Shoukry et al[33][24]. To calculate the ground reflect irradiance on the backside of the module the ground underneath the module is split into a shaded and unshaded part as shown in Figure 3.2.

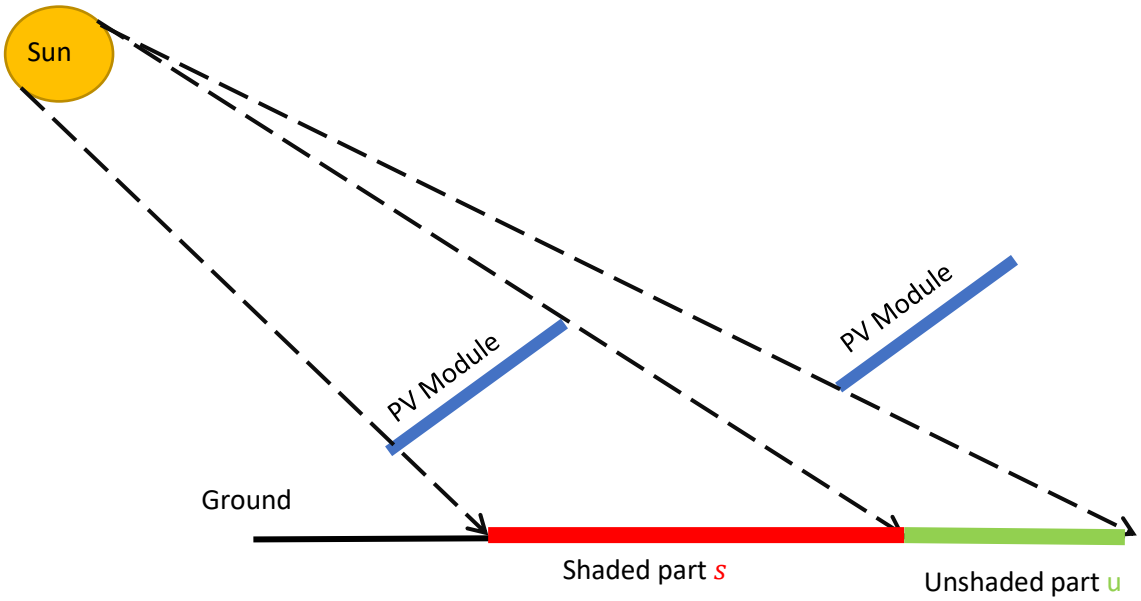

Figure 3.2: Schematic representation of how the unshaded and shaded parts affect the ground reflection of the backside of a bifacial module. The size of the shaded parts will depend on tilt angle, row distance, panel size and clearance height[24].

The view factors of both these section from the back of the module are calculated and will change over time due to the changing shadows caused by the changing sun position. Then using Equation 3.5 the rear side irradiance is calculated.

$$I_{\text{gr,refl}} = \alpha \cdot GHI \cdot F_{A_{\text{unsh}} \to A_{\text{M}}} + \alpha \cdot DHI \cdot F_{A_{\text{sh}} \to A_{\text{M}}} \tag{3.5}$$

Because the *DNI* is blocked by the module the reflected irradiance from the shaded part is only the *DHI*. From the unshaded part the total *GHI* is reflected.

A sidenote to this calculation is the fact that when looking at the view factor calculations made in the previous chapter they do not match with this method. In the previous chapter it was found that that the view factor from ***the module*** to the ***unshaded area*** should be used instead of the other way around. How this was actually solved within the research project of Shoukry et al is not known. But for irradiance it is crucial to understand that the view factor that is used should be the view factor from the surface of interest to the source of irradiance. This source of irradiance can be a sky patch but also a patch of ground if it is reflecting.

For the method proposed by Shoukry et al. the view factor is possible to calculate with an analytical formula. This is due to the fact that the area of the shaded area and unshaded area can be calculated using analytical closed formulas. This is not always the case. If we are looking at more complex geometries like urban environments this is not possible. Then the view factor needs to be calculated using numerical integration. And as the shaded area changes over time this view factor must be recalculated for every time instant. One can see that this is simply not viable. Therefore for complex environments the view factor approach is not a preferable method.

3.2. Ray Tracing Models

The core ray tracing principle is emitted light rays through the landscape of interest and monitoring their intensity, direction and absorption. A few assumptions are classically made when using ray tracing. These assumptions will also be used in this thesis.

It is assumed that the wave nature of light is irrelevant. Therefore effects like diffraction and interference are neglected. Only refraction and propagation through materials are taken into account. This assumption can be made because the scale on which diffraction and refraction occur are small compared to the scale that ray tracing simulations are useful. These assumptions fall under the concept of ray optics[31] and can be summarized as follows:

- Light rays are straight lines
- Reflection and refraction are described by Snell's law described in the previous chapter.
- Transmission and reflection coefficients are calculated using the Fresnel equations
- Light rays do not affect eachother in any way

It is useful to return to the rendering equation discussed in the previous chapter again shown in Equation 3.6. This equation can basically be seen as the basis of how ray tracing models model the light through the scene.

$$L_o = L_e + \int_{\Omega} L_i \cdot \text{BRDF} \cos(AOI) \, \mathrm{d}\, \Omega_\mathrm{i} \tag{3.6}$$

For example if a ray hits a patch of the sky the reflected light (so the integral) will not have any effect as there is no reflection from the sky. However, if it hits a wall the integral will be the only source of outgoing radiation. To find L_o therefore L_i must be computed. The L_i will in turn depend on all the other surfaces and light sources (like the sky) around it. One can imagine that this is reciprocal. One wall affects the other wall and vice versa. Therefore an exit clause must be defined in order for ray tracing to work. This is done by limiting the number of bounces that can occur in a ray tracing model. By doing this geometries can not infinitely affect each other in the amount of radiance they emit or reflect and an infinite loop is broken.

Over the last years ray tracing approaches have gained interest in modelling the irradiance on PV panels. Namely due to their accuracy and ability to handle complex geometries. Also edge effects are more easily taken into account compared to view factor models. The downside of ray tracing is that it is very computationally demanding. As mentioned before ray tracing can be split up into two different methods backward ray tracing and forward ray tracing.

3.2.1. Forward Ray Tracing

Forward ray tracing follows the ray from the source to the module. It is very accurate but in order to get high accuracy a lot of rays need to be calculated. Therefore making it very computationally heavy. Also tracking every ray means that also rays that do not reach the module will be completely tracked making it inefficient.

Santbergen et al.[30] presented a model 2017 which uses the forward ray tracing principle. Firstly a sky map is calculated using the Perez model which is explained in the previous chapter. This sky map will be different for each time instant, in their case hourly data was present. The maps are integrated over an entire year therefore creating a sky map for the the whole year. An example of this can be seen in Figure 3.3. Consequently a sensitivity map is calculated as follows. A forward ray tracing simulation will be performed by placing a light source at different positions in the sky. The module/surface will be illuminated from the direction of interest and parallel rays will be traced from this direction as seen in Figure 3.4. Then the ratio of emitted radiant flux and received radiant flux is calculated which defines the sensitivity for that specific point in the sky. This fraction is defined in Equation 3.7.

$$S = \frac{I_{\text{abs}}}{I_{\text{dn}}} \tag{3.7}$$

In this equation I_{abs} is the power of the absorbed rays and I_{dn} is the power of the illumination beam. Doing this for the entire hemisphere of the sky a sensitivity map is calculated. This map gives the sensitivity of the module/surface for each hemispherical angle of incidence[30].

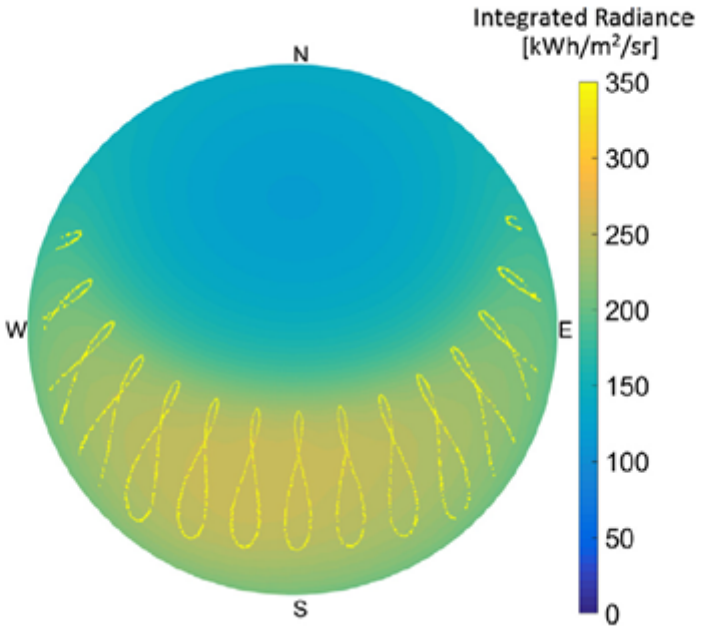

Figure 3.3: Integrated skymap for a whole year as done by Santbergen et al.. The analemmas that can be seen give the suns path over a year[30]. This map is made for a location in Eindhoven, the Netherlands.

It is important to note that this needs to be calculated for each direction to find the entire sensitivty map. Also for each cell of the module the map will be a little different. An example of a sensitivity map result can be shown in Figure 3.4.b The total irradiance over a year will then be found using Equation 3.8.

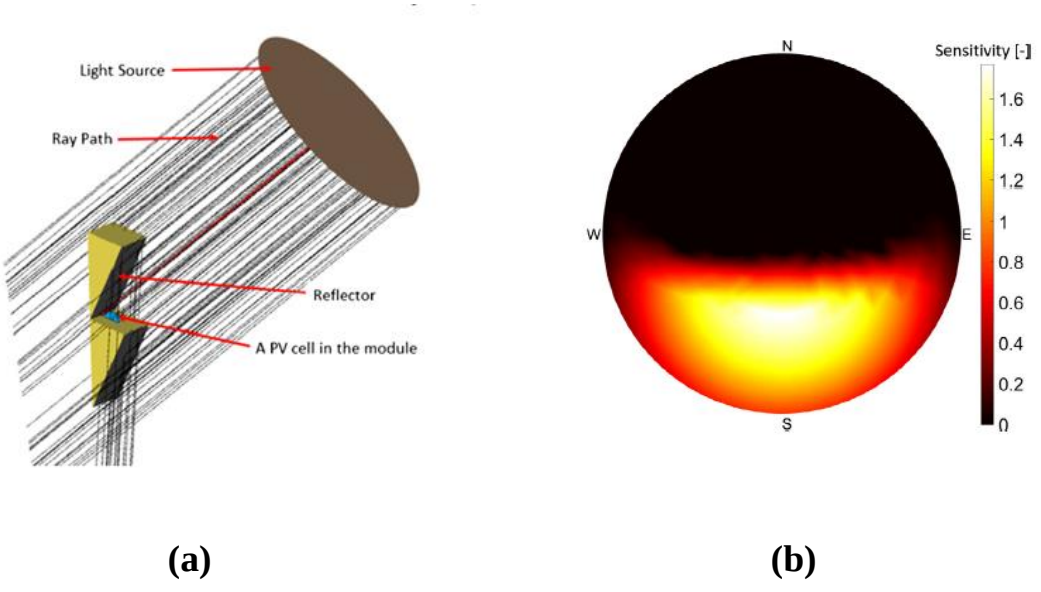

Figure 3.4: **(a)**Diagram of the principle of forward ray tracing as presented by Santbergen et al.[30] **(b)** Sensitivity map calculation as done by Santbergen et al for different tilt angles.

$$G_{\mathrm{m}} = \int_{\mathrm{sky}} \text{skymap} \cdot \text{sensitivity map} \, \mathrm{d}\Omega \tag{3.8}$$

3.2.2. Backward Ray Tracing

In backward ray tracing instead of tracing the rays from source to receptor the rays are traced from the solar cell to the source. By doing this one of the flaws from forward ray tracing is avoided because lot of rays that are traced in forward ray tracing will never reach the solar cell. One of the most commonly used software for backward ray tracing is RADIANCE [39].

RADIANCE is a rendering system developed by the author over the past nine years at the Lawrence Berkeley Laboratory (LBL) in California and the Ecole Polytechnique Federale de Lausanne (EPFL) in Switzerland[20]. The visual rendering side is not that relevant for PV applications however the incoming irradiance can also be modelled using RADIANCE. The rendering side of the Radiance software will be outside of the scope of the thesis however how RADIANCE is applied in PV irradiance modelling will briefly be discussed in this section.

RADIANCE uses a ray tracing approach which is a combination of stochastic ray tracing and deterministic ray tracing[40]. The initial rays traced from the point of interest are stochastic except for one ray called the shadow ray. This ray is deterministic and is aimed at the biggest light source (the sun). The other stochastic rays however are modelled in such a way to optimize the amount of rays into regions of high variance or large amounts of indirect light. For example if a ray hits a surface and RADIANCE needs to calculate the incident irradiance on that surface it casts a ray deterministically to the biggest light source (very often the sun). It can then be checked if this ray is either obstructed or unobstructed. If it is unobstructed the irradiance due to that source can be immidiately calculated. By using this method the biggest source of variance is removed from the calculation. The same can be done for specular surfaces which can also cause peaks in the incident irradiance. Even though this way the computation time is limited for calculating diffuse interreflection it will still too computationally heavy to cast rays for every point. RADIANCE uses interpolation between the points to do this as efficiently as possible. The exact principles behind this interpolation is outside the scope of this thesis. However the use of RADIANCE can be tweaked with 5 main variables. A short explanation of these 5 variables is listed below.

1. **Ambient bounces**: This variable determines the amount of diffuse bounces allowed in the simulation. The minimum value is 0 and this is when only the irradiance coming directly from the sky is considered. Depending on surroundings this value can be either increased or decreased.

2. **Ambient accuracy**: RADIANCE often uses interpolation to limit the amount of secondarily cast rays. Interpolation is used to limit the errors caused by this approximation. The ambient accuracy determines the maximum interpolation error as a fraction. This variable has a big impact on computation time.

3. **Ambient resolution**: this variable determines the amount of points that will be used for hemispherical sampling (i.e secondary ray casting). The higher this value the less interpolation is necessary. The minimum distance between two points that are calculated with hemispherical sampling is given in Equation 3.9.

   $$S_{\mathrm{min}} = D_{\mathrm{max}} \cdot \frac{\text{Ambient accuracy}}{\text{Ambient resolution}} \tag{3.9}$$

   In this equation D_{max} is the maximum feature size of the loaded scene.An increase in ambient resolution can have a very significant impact on simulation time.

4. **Ambient divisions:** this variable determines the amount of points used for hemispherical sampling from each intersection point.

5. **Ambient super-samples:** this variable determines the amount of extra samples in regoins with high variance for the indirect irradiance hemispherical sampling.

Generally using RADIANCE the following structure should be used. First a geometry should be generated that can be loaded into the RADIANCE software. This file should contain material and geometry information and the point(s) of interest where one wants to calculate the irradiance values. This file should then be converted into .rad files. Using the inputs of DNI and DHI a Perez sky model can be generated which will be combined with the .rad files into a special file format called an octree. This is a specific file format which allows efficient

and fast simulation often used in 3D rendering software.

After that the RADIANCE software can be called (either directly or using MATLAB or Python for example). The amount of rays and resolution of the geometrical mesh can be tweaked by the person using the software and depends on the conditions in the 3D model.

In 2015 Lo et al. presented a work in which they used Radiance to model the yield of bifacial solar panels. The surrounding geometry and material properties were implemented in the radiance model. For details the solar cell is modelled very accurately. For example the reflections of the copper ribbons on the cell were taken into consideration. For objects like buildings they are seen as boxes because the details do not matter that much anymore. Using SMARTS a software program that calculates the solar irradiance spectrum is used as an input as well as all the material properties of the surroundings which can be wavelength dependent (for example the refractive index). Because RADIANCE is only able to simulate using RGB colours. For 3 wavelengths the simulation is performed and averaged to come to the final irradiance value on the front and back surface. Using the radiance software the incident irradiance on the PV module could be found.

A downside of using RADIANCE is that as mentioned before it is mainly used for rendering. A lot of features that require computation power are actually not relevant for PV irradiance modelling but are used for visual effects and rendering. On top of that the RADIANCE software is very complex and not tweaked for PV modelling. It is hard to estimate what effect each different adjustment will have on the accuracy or simulation time. Therefore it is hard to adjust the RADIANCE model specifics for the goal that is pursued for your calculations.

A crucial step for both forward and backward ray tracing is to be able to find the intersections between light rays and the surrounding geometry. This can be done with different methods. The speed of the intersection calculation is of great importance to the speed of the overall code. Optimising this will greatly improve the computation time.

3.2.3. Finding intersections

An essential step in ray tracing and therefore in the model that is proposed in this thesis is to be able to find intersections between the light rays and the surrounding environment. If it does not intersect any surrounding geometry this needs to be known and the ray travels to the sky. However if it does hit a surface the interaction with that surface can be modelled. There are many different methods to find the intersections.The method that will be used in this thesis will be discussed in the next section.

The simplest step is to find the intersection between a ray and an infinite plane. How this can be done is described below.

3.2.4. Ray and infinite plane

A line through points P_0 and P_1 can described by the parametric equation $P(s) = P_0 + s\mathbf{u}$. Where P_0 is the origin point of the line $\mathbf{u}$ is the direction vector $(P_1 - P_0)$ and s is a scalar. Then given the plane $\mathbf{P}$ given by a point V_0 on it and a normal vector $\mathbf{n}$ the factor s can be found according to Equation 3.10.

$$s = \frac{-\mathbf{n} \cdot \mathbf{w}}{\mathbf{n} \cdot \mathbf{u}} \tag{3.10}$$

In this equation $\mathbf{w}$ is $P_0 - V_0$. To now find the intersection first it must be checked that for a ray travelling in its positive direction that $\mathbf{s}$ is larger than 0. If so the intersection can be found using the parametric equation $P(s) = P_0 + s\mathbf{u}$. A downside of this simply gives the intersection between ray and an infinite plane. In reality and for our geometries all the planes are bound and part of a surface. So an important step is to find if the found intersection is actually within the bounds of the surface. A method often used in ray-tracing applications uses a barycentric coordinate system.

3.2.5. Barycentric coordinates

Barycentric coordinates are coordinates which are defined relative to vertices of a triangle. This principle is schematically drawn in Figure 3.5. Using this diagram, barycentric coordinates(α, β, γ) of the point $\mathbf{x}$. For example α can be defined as in Equation 3.11[18]:

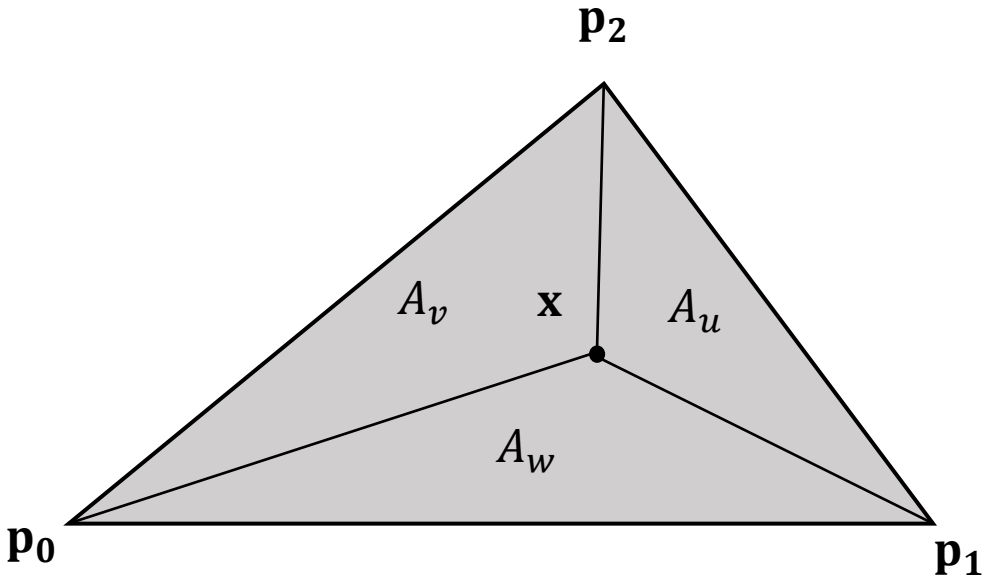

Figure 3.5: Schematic drawing of the barycentric coordinate system principle.

$$\alpha = \frac{A_u}{A} \tag{3.11}$$

Similarly β and γ can be calculated by dividing A_v and A_w instead of A_u. Now to find these coordinates first three vectors are defined. Two of them u and v are the vectors of the triangle/plane of interest and the other w is the vector from a vertix of the triangle to the intersection point. The vectors **u**, **v** and **w** can be calculated using Equation 3.12.

$$\begin{aligned} \mathbf{u} &= p_1 - p_2 \\ \mathbf{v} &= p_3 - p_1 \\ \mathbf{w} &= p - p_1 \end{aligned} \tag{3.12}$$

Computing the areas that are necessary for calculating the barycentric coordinates can be done by using the relation of the cross product to the area A of a triangle given in Equation 3.13.

$$4A^2 = \mathbf{n} \cdot \mathbf{n} \tag{3.13}$$

In Equation 3.13 $\vec{n}$ is the normal vector of the triangle given by $u \times v$. Using Equation 3.13 the total area A of the triangle can be found. Now to compute A_u the normal vector of the triangle that spans up A_u is computed using the cross product which yields $u \times w$. Using this principle it can be shown that the barycentric coordinates will be given by Equation 3.14[18]:

$$\begin{aligned} \alpha &= \frac{(u \times w) \cdot n}{n \cdot n} \\ \beta &= \frac{(w \times v) \cdot n}{n \cdot n} \\ \gamma &= 1 - \alpha - \beta \end{aligned} \tag{3.14}$$

The actual coordinates are then given by Equation 3.15.

$$P = \alpha \cdot P_1 + \beta \cdot P_2 + \gamma \cdot P_3 \tag{3.15}$$

The coordinates lie inside the triangle if α, β and γ are between 0 and 1. So using this principle it can be checked whether or not intersection point is inside the triangle.

3.3. Summary

This chapter has described models that are used to calculate the irradiance on a PV module. View factor models have been described and explained as well as ray tracing models. It can be concluded that view factor models can be used in less complex environments and are especially useful for repetitive geometries. In these type of geometries the view factors can be analytically calculated and do not require computationally heavy numerical integration.

Ray tracing models are especially useful in very complex environments and deliver great accuracy. These type of models can be split up into forward and backward ray-tracing. The difference is the way they track either from source to point of interest or the other way around. The downside of these type of models is the fact that they are computationally demanding. Also conventional ray tracing software is often used for rendering and not for calculating numerical values. Therefore the effect of tweaking and changing model parameters is hard to do and the consequences hard to determine. This makes many currently used ray tracing models not tweaked specifically for PV irradiance modelling.

4

Proposed irradiance simulation model

This chapter will discuss the new framework this thesis proposes. The concept behind the model is combining backward ray tracing with view factors . However there are some fundamental differences between this framework and ray tracing models like RADIANCE. This chapter will discuss those differences. On top of that this chapter will describe the methodology of the framework and its possible advantages and disadvantages.

First of all it is useful to recapitulate why the effort is made to present this new model. The reasons that can be drawn forward are the disadvantages of the models presented in the previous chapter. These disadvantages are reasons to pursue a different approach.

As mentioned for the view factor based models these models have the disadvantage that for complex geometries the calculations will not be accurate. However for backward and specifically forward ray tracing the computation time can be very high. By combining the view factor approach with backward ray tracing the accuracy can be high in complex geometries. Also the model can be more practical to use for PV applicatoins compared to RADIANCE.

This chapter will explain step-by-step how the model calculates the irradiance on the module. The first important step is the ray generation.

4.1. Model framework and calculations

The first step is to define how the rays that will be traced from the point (or points if a higher resolution is needed) of interest will be generated. Therefore first the concept of primary and secondary rays needs to be clear.

- **Primary rays**: These are the rays generated directly from the point of interest. This can be especially useful if multiple test-points are defined which is interesting when modelling an entire module for example. Each point on the module will then be a source of rays. These rays can either directly hit the sky or hit a part of the geometry, a wall or glass for example. When this is the case secondary rays will be generated.
- **Secondary rays**: Secondary rays will be generated when one of the primary rays hits a lambertian or a specular surface. In this model those two are the only type of surfaces that exist. New rays will be cast in a specific manner dependent on the type of surface.

  For this model framework currently only the secondary rays that directly reach the sky will be taken into account. If a secondary ray hits another surface, tertiary rays could be generated. For computational purposes the sequence will be broken at the first reflection. In RADIANCE the amount of bounces can be tweaked. In this model framework the amount of bounces is limited to 1 and the model is not yet structured so that the amount of bounces can be increased.

In order to generate the primary rays equiangularly an azimuthal and altitudal resolution is defined. This resolution determines what spacing in both the azimuthal and altitudal direction the rays will have. The az-

imuthal angle will range from 0 to 360 degrees and the altitudal angle form -90 to 90 degrees. The resolutoins define how fine or coarse the discretization in both the rays and sky will be. Then by using the spherical coordinate transformation the x,y and z coordinates of the end points of the rays is found. All the rays will be normalized for easier calculations. An animation that shows how each ray is mapped to the center of a sky patch is shown graphically in Figure 4.1.

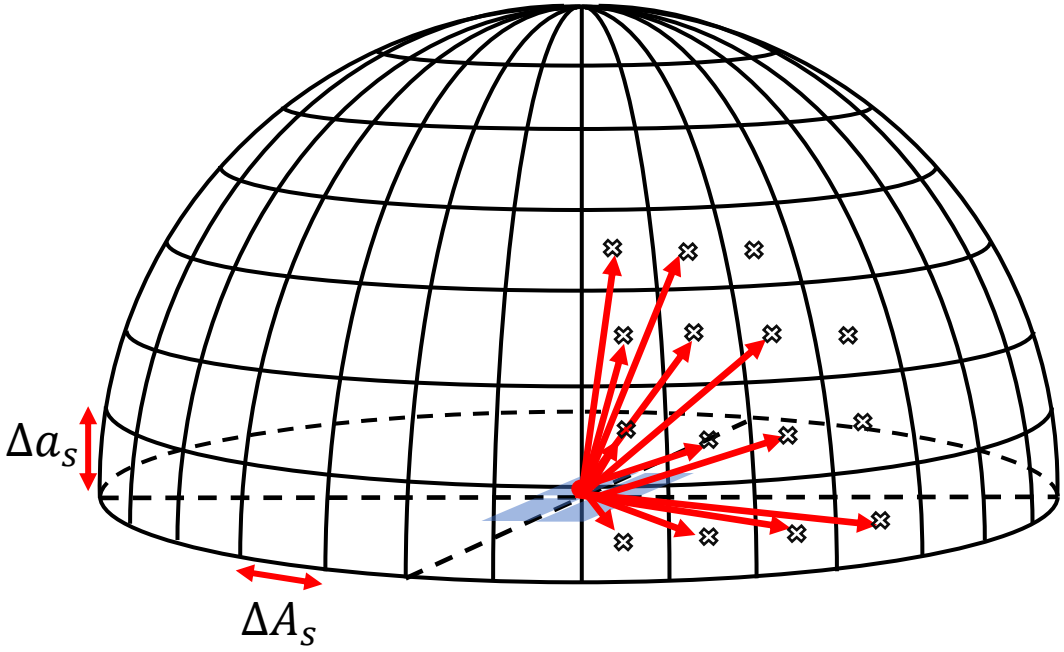

Figure 4.1: Graphic representation of how each individual ray that is cast is mapped to a sky patch. The secondary rays will use the same principle only with a different resolution.

Now to calculate the view factors to the different sky patches the normal of the surface of interest needs to be known. Using the tilt (θ_c) and azimuthal (ϕ_{cell}) direction of the PV module the normal vector $\mathbf{n}_{cell}$ of the cell can be calculated. by using Equation 4.1.

$$\mathbf{n}_{cell} = \begin{bmatrix} \sin(\theta_c) \cdot \sin(\phi_{cell}) \\ \sin(\theta_c) \cdot \cos\phi_{cell}) \\ \cos(\theta_c) \end{bmatrix} \tag{4.1}$$

Then using the direction of each ray, the cosine of the angle of incidence with the module can be found by taking the dot product of both these vectors. By only considering the rays where the cosine of the angle of incidence with the cell is larger than 0 the rays that come from patches behind the panel and cannot reach the cell will not be considered.

The closest intersection between each ray and the geometry are found using the barycentric method described in the previous chapter. This method can be used for triangles and because the imported geometry is a triangular mesh this method can be implemented. A more optimized code regarding the intersections would allow the geometry to be meshed in other shapes as triangles as well.

Consequently the view factor from the module to the sky patches is calculated. To understand this first it is useful to look how the view factor for the entire sky can be calculated using Equation 4.2.

$$SVF = \int_{a_s=0\circ}^{a_s=90\circ} \int_{A_s=0}^{A_s=360\circ} \frac{\cos(\theta_1)\cos(\theta_2)}{\pi} \cos(a_s) dA_s da_s \tag{4.2}$$

In this equation the nomenclature is as shown in Figure 2.4. Because the sky patches are so far away the normal of the individual sky patches can be assumed to be pointing to the center of the module at all times as

shown in Figure 4.2.

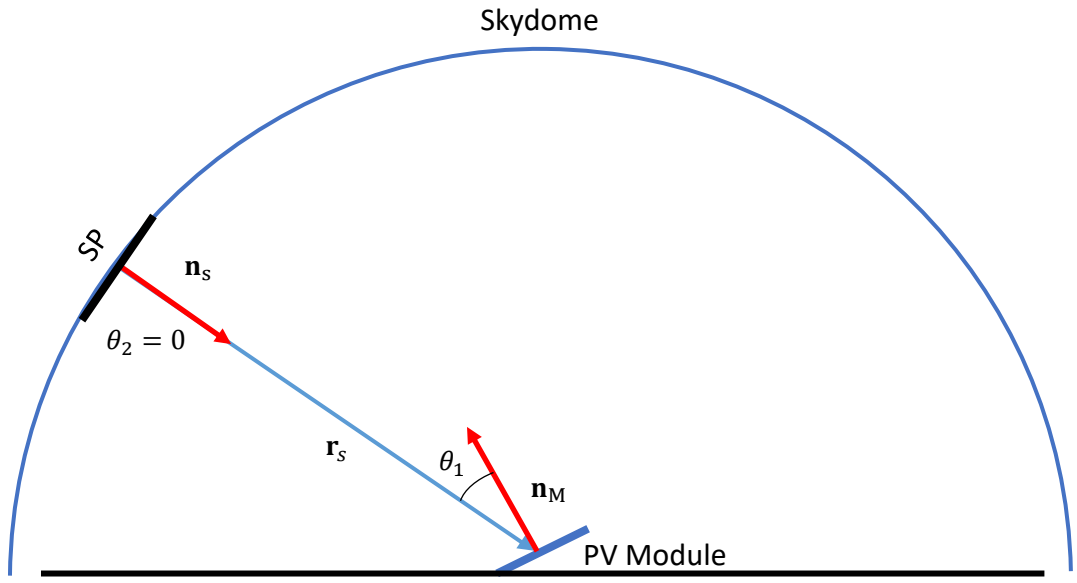

Figure 4.2: Sky patch to module view factor angles. As can be seen the normal of the sky patch is the same direction as the vector from sky patch center to module center. Therefore θ_2 is 0.

The $\cos(\theta_2)$ term will therefore drop away leaving Equation 4.3 which can then be simplified to Equation 4.4 using the dot product to cosine angle relation for normalized vectors $\mathbf{n}_M$ and $\mathbf{n}_s$.

$$SVF = \int_{a_s=0\circ}^{a_s=90\circ} \int_{A_s=0}^{A_s=360\circ} \frac{\cos\theta_1}{\pi} \cos(\theta) \mathrm{d}\phi \mathrm{d}\theta \tag{4.3}$$

$$SVF = \int_{a_s=0\circ}^{a_s=90\circ} \int_{A_s=0}^{A_s=360\circ} \frac{\mathbf{n}_M \cdot \mathbf{n}_s}{\pi} \cos(\theta) \mathrm{d}\phi \mathrm{d}\theta \tag{4.4}$$

In this equation $\mathbf{n}_M$ is the normal of the module and $\mathbf{n}_s$ the normal of the sky patch. Knowing that in this model the sky is discretised into patches with an equiangular distribution meaning that the steps in altitude and azimuth will be the same. The view factor for a differential sky patch can then be derived as follows. It is known that the view factor must be taken from the module to the sky patch. In differential terms therefore Equation 4.5 is the starting point.

$$\mathrm{d}F_{M \to S} = \frac{\cos(\theta_1)\cos(\theta_2)}{\pi} \mathrm{d}S \tag{4.5}$$

Knowing that for the sky patch the normal will always be pointing to the center of the module $\cos(\theta_2)$ will drop away. Then using the dot product equivalency Equation 4.5 can be rewritten to Equation 4.6.

$$\mathrm{d}F_{M \to S} = \frac{\mathbf{n}_M \cdot \mathbf{r}_s}{\pi} \mathrm{d}S \tag{4.6}$$

Mathematically it can be shown that $\mathrm{d}S$, the differential surface area of the sky patch, can be substituted for $\mathrm{d}\Omega$, the differential solid angle. Because the sky hemisphere can be seen as a unit sphere. Why this equality is valid will be derived in the next few equations. The differential solid angle $\mathrm{d}\Omega$ can be written as Equation 4.7.

$$\mathrm{d}\Omega = 4\pi \left(\frac{\mathrm{d}S}{A} \right) (\mathbf{r}_s \cdot \mathbf{n}_s) \tag{4.7}$$

In this equation $\mathbf{r}_s$ is the vector from the viewing point to the sky patch of interest and $\mathbf{n}_s$ the normal of the sky patch. In this equation $r = 1$ for it is a unit sphere. Then $A = 4\pi \cdot r^2$ will be equal to 4π. On top of that $\mathbf{r}_s \cdot \mathbf{n}_s$ is also 1 because these vectors point in the same direction. This principle is also seen in Figure 4.2. Then the equality described in Equation 4.8 is valid.

$$d\Omega = dS \tag{4.8}$$

So the final differential view factor will be given by Equation 4.9.

$$dF_{M\to S} = \frac{\mathbf{n}_M \cdot \mathbf{r}_s}{\pi} d\Omega \tag{4.9}$$

So to find the view factors the area/solid angle of these sky patches therefore must be calculated. In reality the view factors/solid angles will not be differential but will be approached as if they are. This calculation is split into two different parts: the spherical cap and all the other patches. All spherical patches have four corners except the patches that make up the top cap of the sphere. These patches will have three corners. The area of the spherical cap can be derived using Equation 4.10.

$$\Omega_{cap} = A_{cap} = \int_0^{2\pi}\int_0^{\theta} \sin(\theta)\, d\theta\, d\phi = 2\pi \int_0^{\theta} \sin(\theta) d\theta = 2\pi [-\cos(\theta)]_0^{\theta} = 2\pi(1-\cos(\theta)) \tag{4.10}$$

As this cap will be still azimuthally divided this area will be divided by the azimuthal resolution as in Equation 4.11 to get the area of the individual patches on the spherical cap.

$$\Omega_{patch,cap} = A_{patch,cap} = \frac{A_{cap}}{Az_{res}} = \frac{\Omega_{cap}}{Az_{res}} \tag{4.11}$$

The area and solid angle of the other patches can be derived using by integrating as in Equation 4.12 and then be reduced to Equation 4.13.

$$\Omega_{SP} = A_{SP} = \int_{\phi_0}^{\phi_1}\int_{\theta_0}^{\theta_1} r^2 \cdot \sin(\theta) d\theta d\phi \tag{4.12}$$

$$\Omega_{SP} = A_{SP} = r^2(\cos(\theta_0) - \cos(\theta_1)) \cdot (\phi_1 - \phi_0) \tag{4.13}$$

These steps must be performed for both the primary Ω_{SP_1} and secondary sky patches Ω_{SP_2} as their solid angles are different.

One very crucial advantage of the method proposed in this thesis is the fact that all the steps mentioned up until now can be calculated before the geometry or sky conditions are known. The view factors from the module to the sky patches do not change and for a particular sky distribution and can therefore be pre-calculated. Then for different sky conditions or varying spectral simulations this geometrical part does not have to be recalculated.

After the rays are cast the rays that reach the sky immediately can be found as well as the ones that intersect with the geometry.

Both will be handled differently it is therefore useful to split this up in two different sections. One section for the escaped rays and one for the rays that intersect with the geometry.

4.1.1. Rays that escape to the sky

As the rays are generated in an equal manner to the sky patch distribution as shown in Figure 4.1 The rays that escape and reach the sky as shown i need to be filtered from the total amount of rays.

1. First, from all the rays, the rays that escape are filtered out. Creating a new subset of rays : $\mathbf{r_{esc}}$
2. Secondly, the indexes rays that move upwards from the cell are found because rays that move down will never reach the sky. These indexes can be called $\mathbf{I_{r,sky}}$
3. Filtering out $\mathbf{I_{r,sky}}$ on $\mathbf{r_{esc}}$ the rays are found that reach the sky: $\mathbf{r_{sky}}$

Then using the indices of the rays the corresponding sky patchs can be found. The cosine of the angle of incidence for $\mathbf{r_{sky}}$ is found for each ray that hits the sky. Then the radiance of the corresponding sky patches is found and multiplied with the area/solid angle and the cosine of the angle of incidence. This gives the irradiance due to the rays that escaped. This formula is given in Equation 4.14.

$$G_{\mathrm{m}}^{\mathrm{dir}} = \sum_{i} L_{\mathrm{SP}_{1,i}} \cdot \Omega_{\mathrm{SP}_{1,i}} \cdot \cos(AOI) \tag{4.14}$$

In this equation L_{SP_1} is the radiance of the primary sky patch, $\Omega_{\mathrm{SP}_{1,i}}$ the solid angle of that sky patch.

4.1.2. Rays that intersect geometry

The first step in calculating the contribution coming from rays that intersect with the geometry is to know what kind of surface it hits. In this model framework these can be split up into two. It will hit either a Lambertian surface or a specular surface. These two surfaces will be treated separately. Some steps however are the same for both of the surfaces.

Firstly the intersections are isolated and for each of the planes the specific index of that plane is found. Therefore in the generation of the 3D model each plane is assigned a name. Then using a separate code these names correspond to a reflectivity value. For lambertian surfaces a reflectivity is attributed to each different type of surface.The values come from different types of measurements which will be discussed in the next chapter. For specular surfaces either -1 for glass for -2 for a mirror is assigned. Though this is not physical this is simply a way to identify what type of surface it is. Using this principles the lambertian rays and specular rays are split up. For both the Lambertian surfaces as well as specular surfaces the surface normals are defined: $\mathbf{n}_{\mathrm{lambertian}}$, $\mathbf{n}_{\mathrm{specular}}$ as these normals are used in the following calculations. First lambertian surfaces will be treated.

Rays that hit Lambertian surface

The first step for a lambertian surface is to cast new rays. These will also be generated in an azimuthal and altitudal grid. In Figure 4.3 this principle is shown schematically. The new rays will be generated in a hemi-

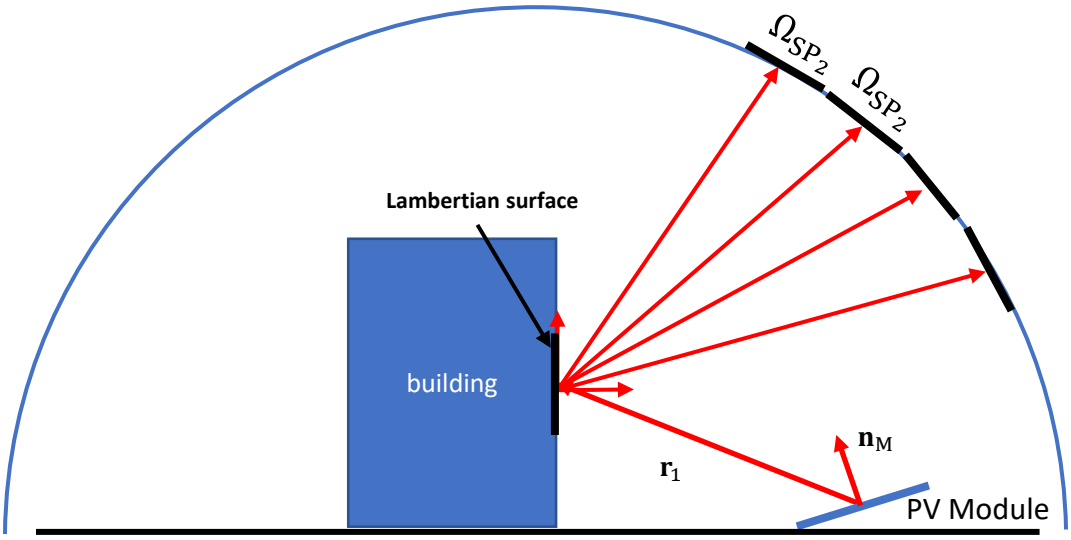

Figure 4.3: Schematic representation of what the model does when a ray hits a lambertian surface.

sphere relative to the surface intersected. The concept of filtering out all the unnecessary rays is equal to the method for the cell itself. For all of the newly generated rays the angle of incidence to the surface is calculated AOI.

Consequently it is chosen in this model framework that the secondary rays that reach the sky will the only rays that will be evaluated. The ones that intersect a geometry are seen as blocked rays and not taken into consideration. These will be neglected in the irradiance calculation as only one bounce is taken into consideration.

From the rays reaching the sky then the following steps are performed.

1. **Calculate incident irradiance on the surface** The first step is to calculate the incident irradiance on the surface coming from a sky patch can be found by multiplying the area of that sky patch with the radiance of that sky patch times the cosine of the angle of incidence of that particular ray. This is similar to calculating direct irradiance on the PV module. However, because a unit sphere is used not the area is used but the solid angle of the sky patch as mentioned before. Summing this over the sky patches will give the total incident irradiance. This can be seen in Equation 4.15.

$$G_{\text{lamb}}^{\text{dir,surface}} = \sum_i L_{\text{SP}_{2,i}} \cdot \Omega_{\text{SP}_{2,i}} \cdot \cos(AOI) \tag{4.15}$$

   As can be seen the method is extremely similar to the incident irradiance on the PV module.

2. **Calculate amount reflected to the PV module**

   To calculate the amount of irradiance reflected on the cell the following principle is used. Instead of using the view factor from the cell to the surface it hit which would be the most accurate way. The view factor to the sky patch it 'would' hit is used. This can be done because the solid angle to the blocking surface is equal to the solid angle of the sky patch. To calculate this view factor the normal of the module is needed as well as the vector that connects the centers and the solid angle of the surface as mentioned in Equation 4.9. By using the equivalence that the solid angles of the blocked surface and the sky patch are the same, the solid angle of the sky patch Ω_{SP} can be used to calculate the view factor. This sky patch will be called SP_{L}.

   By doing this the calculation of the view factors to each particular triangle of the mesh in the geometry is avoided. But Equation 4.9 can be used for all sky patches beforehand and if a ray intersects the geometry this view factor can be taken. How this assumption-principle works is shown in Figure 4.4

   However, there is a sidenote to be placed with using the method that the solid angle of the blocked surface is equal to the solid angle of the sky patch. How big the surface is seen by the cell can be misjudged. As the projection of the sky patch can be larger than the surface actually is in the real geometry and vice-versa. How this principle works out is shown in Figure 4.5. Also if the intercepted surface is for example triangularly shaped this is not how it will be seen for a rectangularly shaped sky-grid. It is expected the inaccuracies for a fine enough ray discretization will not lead to big inaccuracy in the reflected irradiance calculation The incident irradiance coming from a surface will then be calculated by multiplying the incident irradiance on the surface times the reflectivity times the view factor from cell to the sky patch $\text{SP}_{\text{L},j}$ the ray hypothetically would hit. For a single lambertian surface this yields Equation 4.16.

$$\text{d}G_{\text{m}}^{\text{refl,lambert}} = \rho_{\text{j}} \cdot \text{d}G_{\text{m}}^{\text{dir,j}} \cdot \text{d}F_{\text{cell}\rightarrow\text{SP}_{\text{L},j}} \tag{4.16}$$

   Which for N lambertian surfaces together yields Equation 4.17

$$G_{\text{m}}^{\text{refl,lambert}} = \sum_{j=1}^{N} \rho_{\text{j}} \cdot \text{d}G_{\text{m}}^{\text{dir,j}} \cdot \text{d}F_{\text{cell}\rightarrow\text{SP}_{\text{L},j}} \tag{4.17}$$

   In this equation $F_{\text{cell}\rightarrow\text{SP}_{\text{L},j}}$ is the view factor from module to the sky patch j and α_j the reflectivity of surface j.

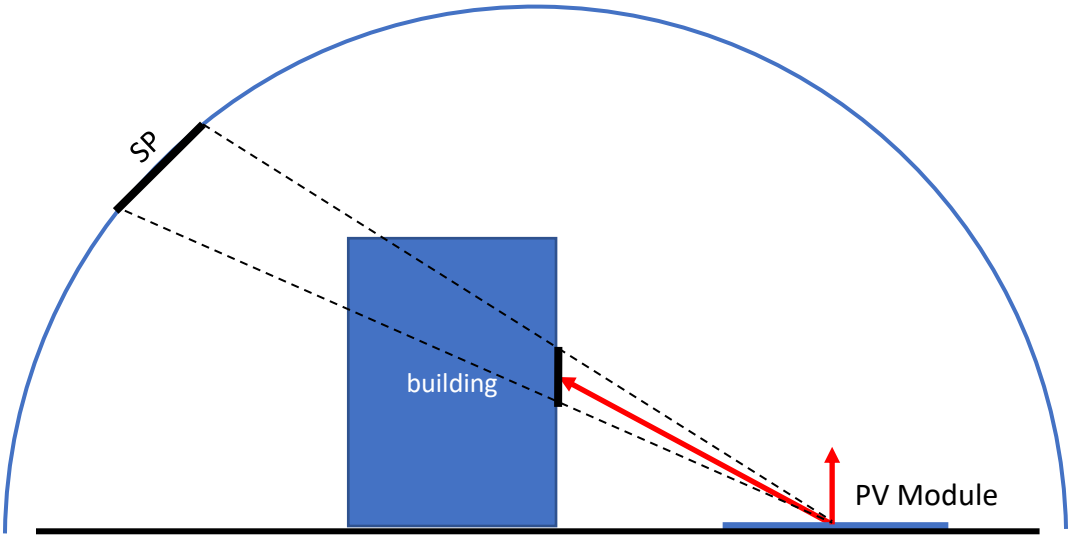

Figure 4.4: Graphical representation how the sky patch is projected on the surface it intersects. The same view factor can be used for the surface as for the sky patch.

Rays that hit specular surface

For the rays that hit a specular surface a different approach is needed. Again first the distinction is made in the type of surface in the manner explained in the previous subsection. When it is known it is a specular surface the following sequence begins.

First a distinction is made between two specular type surfaces. One is the perfect mirror and the other one is a general dielectric. In urban environments this dielectric will almost always be a glass. For both mirrors and the dielectric the following steps are taken:

1. The normal of the specular surface $\mathbf{n}_{\text{specular}}$ is acquired
2. The solid angle of the sky patch the primary ray would hit if not for the specular surface is filtered out of all the solid angles.
3. A vector $\mathbf{r}_1$ is created from the intersection point to the center of the cell and normalized.
4. The reflected ray vector $\mathbf{r}_2$ is created by using Equation 4.18.

$$\mathbf{r}_2 = 2 \cdot (\mathbf{r}_1 \cdot \mathbf{n}_{\text{specular}}) \cdot \mathbf{n}_{\text{specular}} - \mathbf{r}_1 \tag{4.18}$$

5. It is checked whether the reflected ray hits the geometry or the sky
6. If it hits the sky it is possible that multiple rays from the same specular surface hit the same sky patch. In that case the one with the smallest AOI on the specular surface is chosen.

To show how the vectors can be seen graphically is shown in Figure 4.6. To calculate the irradiance by the the radiance of the sky patch it hits is multiplied with the cosine of the angle of incidence and the solid angle. In the case of a mirror there is no loss due to transmission as all the light will be reflected so no reflection coefficient. Therefore the irradiance due to a single mirror reflection of a single mirror surface will be given by Equation 4.19.

$$\mathrm{d}G_{\text{m}}^{\text{refl,mirror}} = L_{\text{SP}_2} \cdot (\mathbf{n}_{\text{specular}} \cdot \mathbf{r}_1) \cdot \mathrm{d}\Omega_{\text{SP}_2} \tag{4.19}$$

In the case of dielectric the Fresnel coefficient R_{s} of reflection need to be taken into account given by Equation 2.36 on page 18. The angle of incidence and angle of transmission will need to be calculated to acquire

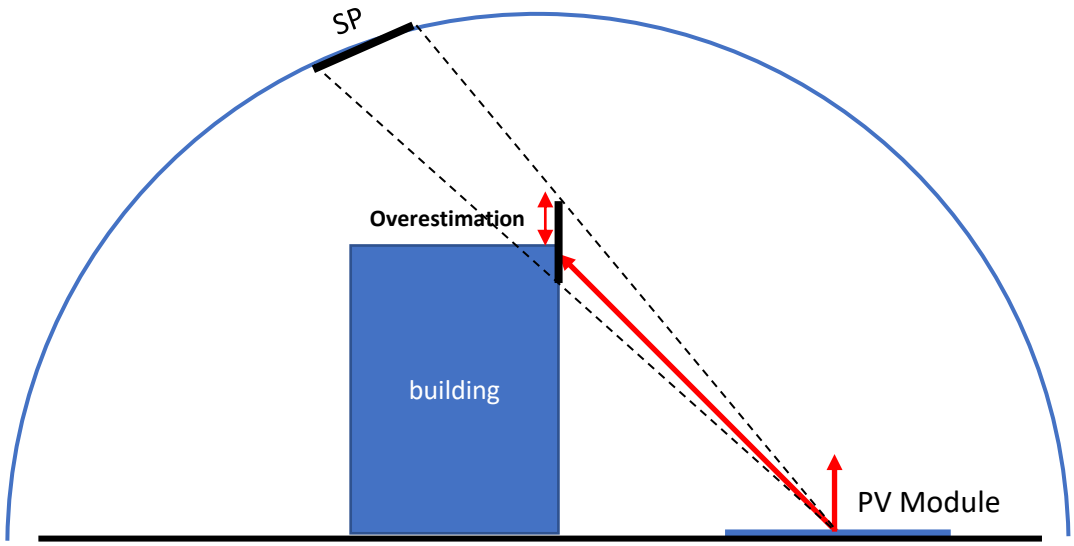

Figure 4.5: Possible view factor overestimation by using the the view factor of the sky patch it would hit.

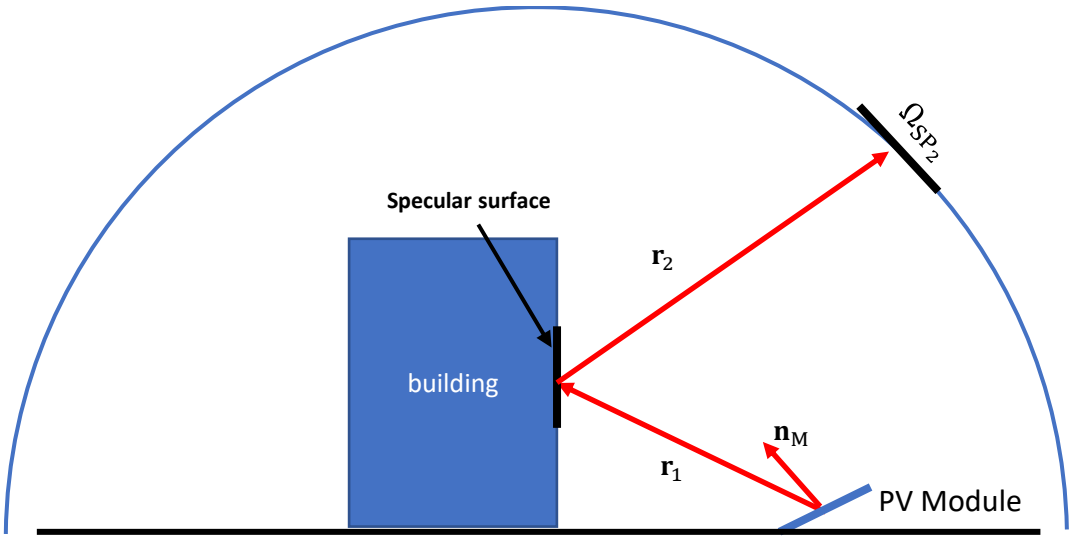

Figure 4.6: Schematic representation how the model works when a ray hits a specular surface.

this coefficient which can be done using Equation 2.37. Then the irradiance due to the dielectric reflection due to a single glass surface will be given by Equation 4.20

$$\mathrm{d}G_{\mathrm{m}}^{\mathrm{refl,mirror}} = R_{\mathrm{s}} \cdot L_{\mathrm{SP}_2} \cdot (\mathbf{n}_{\mathrm{specular}} \cdot \mathbf{r}_1) \cdot \mathrm{d}\Omega_{\mathrm{SP}_2} \tag{4.20}$$

4.2. Model flowchart

This section is dedicated to discussing the final model flowchart which can be seen in Figure 4.7. There is a crucial property in the way the proposed model is structured computationally. This has not been fully described in previous subsections. This property can be be more easily seen in the model flowchart. The sky conditions and material properties (in orange) like reflectivity are only used after all the geometrical calculations (in blue) are done. All the solid angles, view factors and intersections can be calculated without the need of any actual sky conditions.

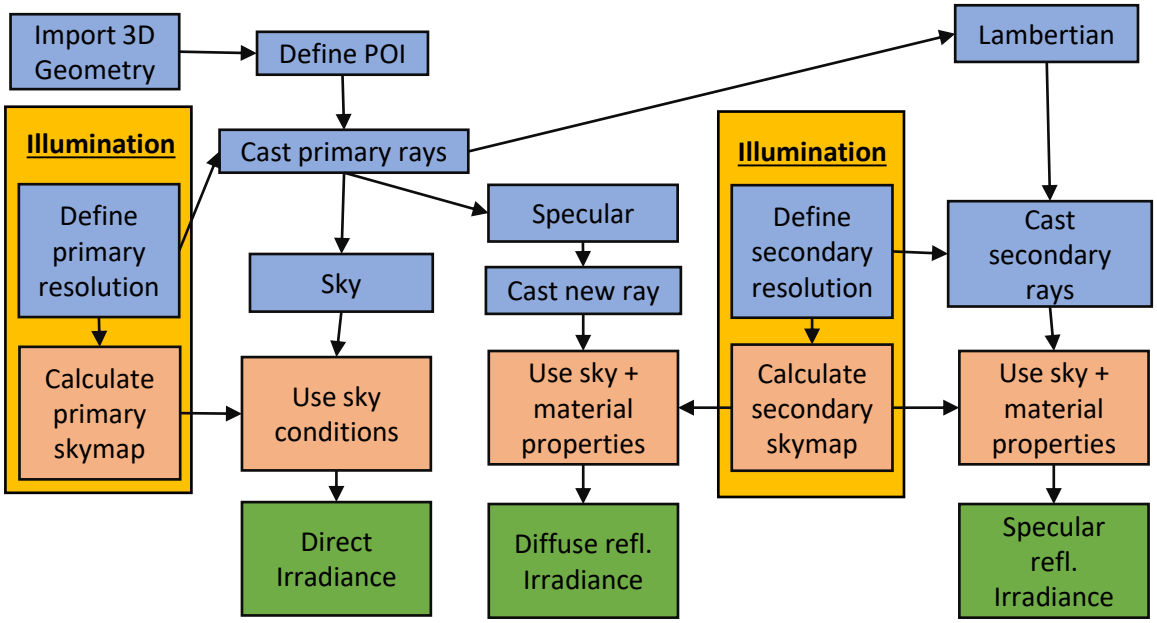

Figure 4.7: Simplified flowchart of the entire model framework.

Due to this decoupled approach if one wants to change the material properties or the sky conditions the geometrical part does not need to be recalculated. This approach has a number of benefits.

- **Spectral simulations**: as the sky conditions are only used at the very end. For different spectra/wavelenghts only the last part of the calculation needs to be performed for the different spectra/wavelengths. One could generate multiple different skymaps for each spectrum and then run the simulation. Again the geometrical part is the same for all of them. This limits the computation time and allows for faster computation for spectrally resolved simulation.

- **Adjustment of material properties** : It is very easy to change the properties of a material. If the reflectivity needs to change it is only changing one number. Because all the geometrical parts stay the same this does not need to be recalculated. This property will therefore also allow reflectivity values that change over time. Which can be useful for example for either snow or dust accumulation on certain surfaces.

For further clarification a flowchart is shown in Appendix D that compares the flow of geometry/skymap loading of our model to RADIANCE.

4.3. Summary

This chapter has described the developed model framework. The framework of the model has been outlined as well as the specific calculation methods for either rays hitting the sky, a lambertian or a specular surface. This chapter has been able to answer the following research questions.

1. **What type of reflections do we need to model in order to accurately simulate the irradiance impinging on a PV module in a complex environment?**

   - *How do we accurately and efficiently model different reflective properties?*
     The proposed model differentiates between two different types of surfaces or reflectors: diffuse (Lambertian) and ideally specular.

     For the lambertian surfaces: it is chosen to cast rays in all directions evenly and find the respective incident irradiance from only the sky coming in. This simulates the isotropic scattering behaviour as described by the BRDF of a lambertian. The incident irradiance on the lambertian surface can then be calculated using Equation 4.21.

     $$G_{\text{lamb}}^{\text{dir,surface}} = \sum_i L_{\text{SP}_{2,i}} \cdot \Omega_{\text{SP}_{2,i}} \cdot \cos(AOI) \tag{4.21}$$

     For the specular surfaces: In the case of an ideal specular reflector, it is considered that the solar cell receives the radiance of a single sky patch incident on the reflector. The position of the sky patch of interest can be determined by mirroring the vector that connects the solar cell and the reflector. This vector is determined using Equation 4.22

     $$\mathbf{r}_2 = 2 \cdot (\mathbf{r}_1 \cdot \mathbf{n}_{\text{specular}}) \cdot \mathbf{n}_{\text{specular}} - \mathbf{r}_1 \tag{4.22}$$

   - *How do we calculate irradiance coming from different type of reflectors?*:
     Once the irradiance on the different type of reflectors is determined, the contribution to the reflected irradiance on the solar cell is determined using the BRDF function of the reflector.

     For the lambertian surfaces: The amount of irradiance due to a lambertian surface can be written as Equation 4.23

     $$\mathrm{d}G_{\text{m}}^{\text{refl,lambert}} = \rho_{\text{j}} \cdot \mathrm{d}G_{\text{m}}^{\text{dir,j}} \cdot \mathrm{d}F_{\text{cell}\rightarrow \text{SP}_{\text{L},j}} \tag{4.23}$$

     Which for all lambertian surfaces together yields Equation 4.24

     $$G_{\text{m}}^{\text{refl,lambert}} = \sum_{j=1}^{N} \rho_{\text{j}} \cdot \mathrm{d}G_{\text{m}}^{\text{dir,j}} \cdot \mathrm{d}F_{\text{cell}\rightarrow \text{SP}_{\text{L},j}} \tag{4.24}$$

     For the specular surfaces: In the case of a specular reflector the contibution to the reflected irradiance on the solar cell is expressed in Equation 4.25. For a mirror R_{s} is a constant which equals 1 if the mirror is ideal. For any other specular reflector (dielectric) it is the Fresnel Coefficient dependent on the angle of incidence and the refractive index.

     $$\mathrm{d}G_{\text{m}}^{\text{refl,mirror}} = R_{\text{s}} \cdot \mathrm{d}L_{\text{SP}_2} \cdot (\mathbf{n}_{\text{specular}} \cdot \mathbf{r}_1) \cdot \mathrm{d}\Omega_{\text{SP}_2} \tag{4.25}$$

2. **Create a model that is structured in a way that accelerates simulation.**

   - *Subdivide the model into decoupled blocks to allow efficient simulation.*
     This objective has been fulfilled by the proposed irradiance model by decoupling of the geometrical problem from the illumination problem. The intersections, (reflected) ray directions, incidence angles, solid angles and other geometrical properties are all calculated independently from the sky conditions. Also the optical properties of the materials are not tangled with the sky conditions. Hence, using this geometry data, which can be solved in a high resolution beforehand, combined with the sky conditions the irradiance simulation can run. This decoupled structure allows efficient simulation over longer time periods because the geometrical problem does not have to be recalculated for each different sky condition.

- *Structure the model so that it allows us to perform spectrally resolved simulations and model surfaces with time dependent reflective surface properties.*
  This objective has been reached by the same decoupling principle as mentioned above. The decoupling of the reflectivity values from the ray tracing geometrical solution allows to solve the irradiance on the cell considering the spectral reflectivity of the surface without the need to repeat the time consuming ray-tracing simulations. For the same reasons, the model also allows to input different reflectivity values for each simulated time instant. This allows to model Lambertian surfaces with time-varying reflectivity properties.

5

Experimental Setups and Validation

This chapter will describe the experiments performed to validate the proposed irradiance model. The main experiment that will be discussed is the specular reflection experiment performed on the roof of the PVMD monitoring station. However, first input data for the proposed model needs to be measured.

5.1. Measuring the input values for the sky model

To generate the sky conditions used in the models the input values of *DNI* and *DHI* must be measured. The Solys2 sun tracker[19] on the side of the right front corner of the roof is used to measure the *DNI*,*DHI* and *GHI*. Three instruments are mounted on the Solys2 sun tracker. To measure *DNI* a pyrheliometer is used. A pyrheliometer is an elongated instrument that has a small orifice trough which the the sunlight can pass. The instrument is mount on the tracker in such a way that it is always pointing to the Sun. Because the Solys2 station tracks the sun this tube will always have its orifice towards the sun, only letting in the direct component from the sun. To measure the *DHI* a pyranometer with a shading ball is used and for the *GHI* an unblocked pyranometer The pyranometer with the shading ball does the exact opposite of the pyrheliometer. The shading ball always blocks the sun and therefore only the diffuse component should hit the pyranometer. However it is logical to see that due to surrounding geometries also reflected light will hit the pyranometer. This disturbs the *DHI* values and therefore the *DHI* values that will be input in the irradiance model need to be corrected. The correction method for the *DHI* measurements is described in Appendix A.

In Figure 5.1 the entire Solys2 station can be seen as well as a close up of the different pyranometers.

5.1.1. Geometry measurement and orientation

To acquire accurate modelling results a 3D model of the roof of the PVMD monitoring station is required. In previous research performed a 3D Rhino model of the PVMD monitoring station was acquired by laser measurements performed by Ruben Cardose. Since the generation of the first model, one of the chimneys in the roof was removed. In this work, the 3D model was corrected and also new details were added. The accuracy of the frames of the windows have been improved and remeasured. The structures on the left side of the roof are added and their dimensions and position refined. Also the black cable holder path and concrete path are added to the model. A 3D model capture of the PVMD monitoring roof can be seen in Figure 5.2.

5.1.2. Measuring reflectivity values of materials on the PVMD monitoring station

As mentioned in the previous chapter all surfaces in the model are either a perfect lambertian reflector or a specular reflector. This section describes how the reflectivity of the lambertian surfaces was measured.

For the materials found on the roof a sample was taken and input in a LAMBDA spectrophotometer. The LAMBDA spectrophotometer allows the measurement of the spectral reflectivity of a material. Multiple samples were taken of materials around the PVMD monitoring roof. The materials that are present on the roof are Black Plastic (which is from the cableholders), a type of mat material which covers different structures on the roof, white paint for walls and different structures. For some materials there is differentiation between clean and dirty versions of the materials. To see whether the reflectivity would vary after a rainy day.

(a) **(b)**

Figure 5.1: (a) Close up from the different pyranometers installed on the Solys2 station. The first pyranometer is used to measure the DHI and is using a shading ball while the other two can be used for measuring GHI. The pyhreliometer used for the DNI cannot be seen in this picture. **(b)** Position of the Solys2 station on the roof of the PVMD monitoring station.

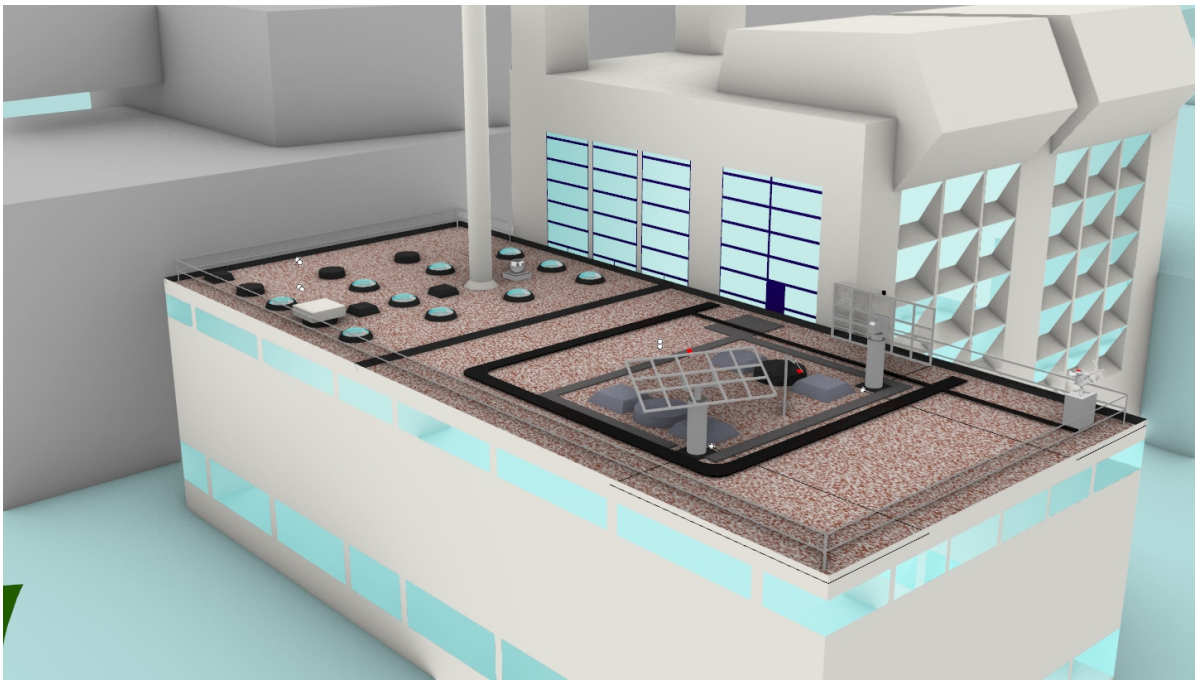

Figure 5.2: 3D Rhino model capture of the PVMD monitoring station with added details on the floor of the roof as well as the windows and facade.

The reflectivity spectrum of the different materials as acquired with the LAMBDA spectrophotometer can be seen in Figure 5.3. It can be seen that for the white paint the 'cleanness' greatly affects the reflectivity. However for the mat material it is the other way around as the dirty/old mat was lighter in color.

The sky conditions in this model are not yet spectrally resolved so the spectral reflectivity needs to be averaged out over the incoming spectrum. The AM1.5 spectrum shown in Figure 2.13 will be used in combination

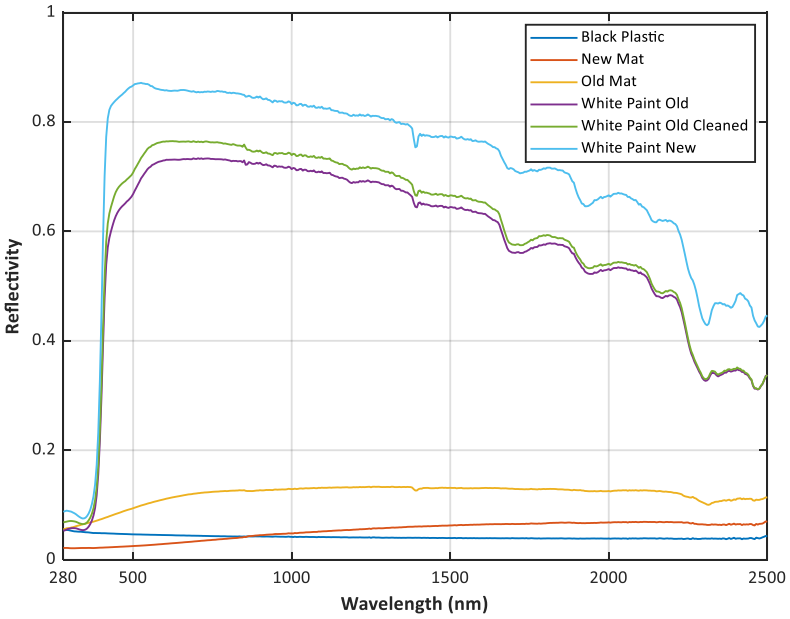

Figure 5.3: Spectral reflectivity for a selection of different materials found on the PVMD monitoring station.

with equation Equation 5.1 to find the spectrally averaged reflectivity.

$$R = \frac{\int R(\lambda) \cdot G_{AM1.5}(\lambda) \cdot \mathrm{d}\lambda}{\int G_{AM1.5}(\lambda)} \tag{5.1}$$

The results of the different materials can be found in Table 5.1. The floor of the PVMD monitoring station is

Table 5.1: Spectrally averaged reflectivites using the AM1.5 for different materials found on the roof of the PVMD monitoring station.

Material	Average reflectivity AM1.5
Black Plastic	0.044
New Mat	0.038
Old Mat	0.113
Oldest Mat	0.114
Thin Mat	0.035
Whitepaint	0.658
Cleaned Whiteapint	0.688
Whitepaint Lid	0.795

covered with small rocks so the same LAMBDA measurements were done for a number of rocks. The results of these measurements can be seen in Figure 5.4. It can be seen that for the rocks the spectral reflectivity is very different for each rock. Therefore to find an average reflectivity to of these pebbles the previous approach is not applicable. Because in the model the roof surface will be modelled as one surface it is necessary to be assign one reflectivity value to the pebble surface. The individual characteristics of each rock can not be taken into account. To find the reflectivity of this pebbles an albedo measurement was done as follows. An albedometer from Kipp and Zonen is placed 1.2 meters above the ground with as little other geometries around it. Of course reflections from the other surfaces will affect the measurements but the main reflected irradiance on the bottom pyranometer is expected to come from the pebbles. This albedo meter uses two pyranometers where one is pointing to the sky and one to the ground. By dividing the incoming *GHI* on the top pyranometer by the irradiance impinging on the bottom pyranometer the albedo is found. This is done using the setup shown in Figure 5.5. All measurements hovered around 0.14 to 0.18. The result of this measurement can be seen in Figure 5.6. A final reflectivity value of 0.17 was chosen for the model. The reason

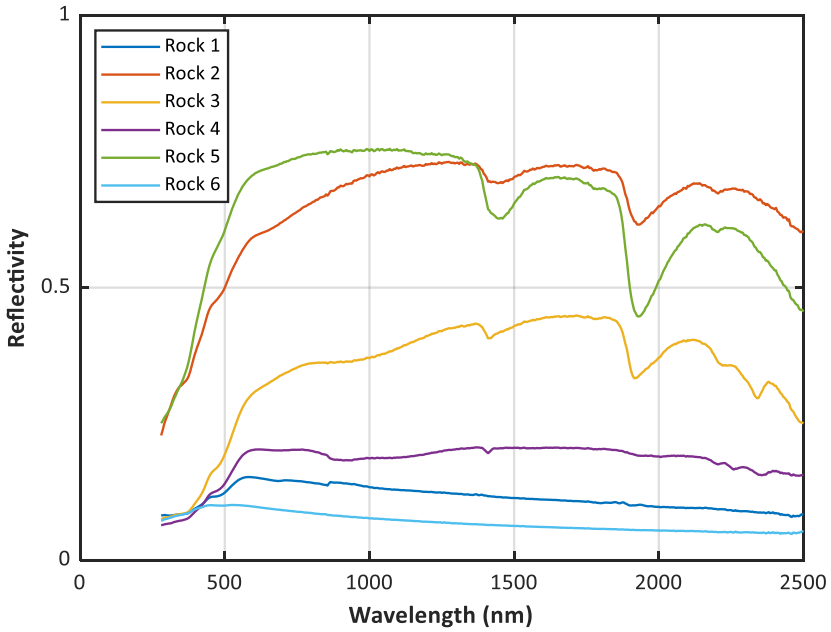

Figure 5.4: Specular reflectivity for 6 dry rocks found on the PVMD monitoring station.

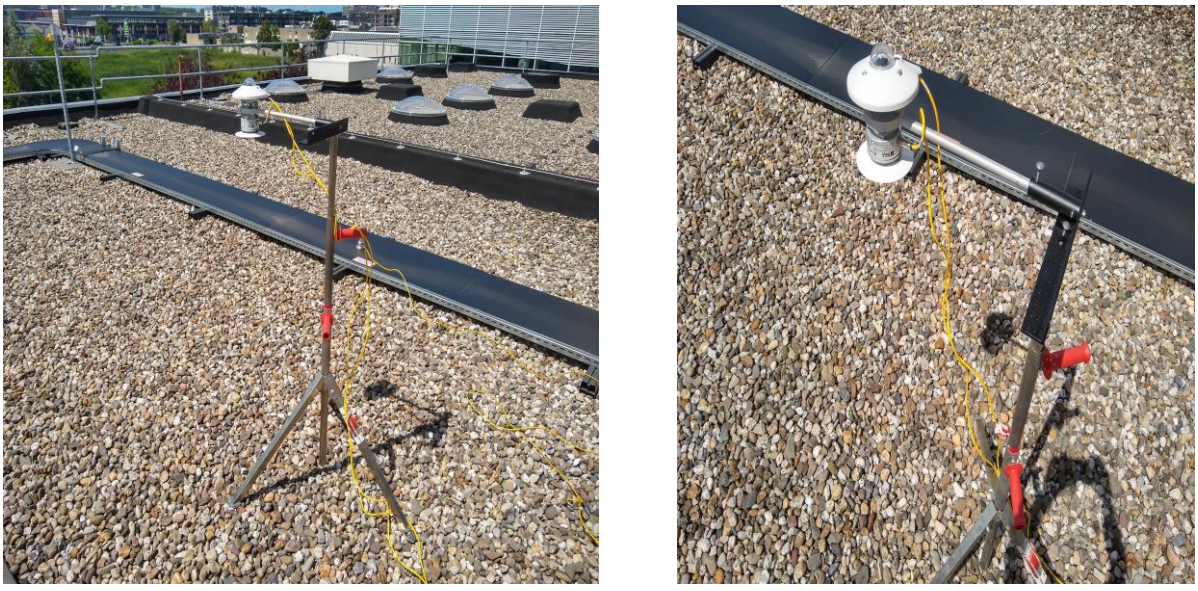

Figure 5.5: **(a)**: Experimental setup for measuring albedo of the pebbles on the PVMD monitoring station roof.**(b)**: Close up of the experimental setup for measuring albedo of the pebbles on the PVMD monitoring station roof.

this value does not have to be determined more accurately is due to the fact that the effect of surrounding geometries is expected to have a larger impact.

Now that the inputs for the model are known the experiments that are conducted to validate the model will be described in the next section.

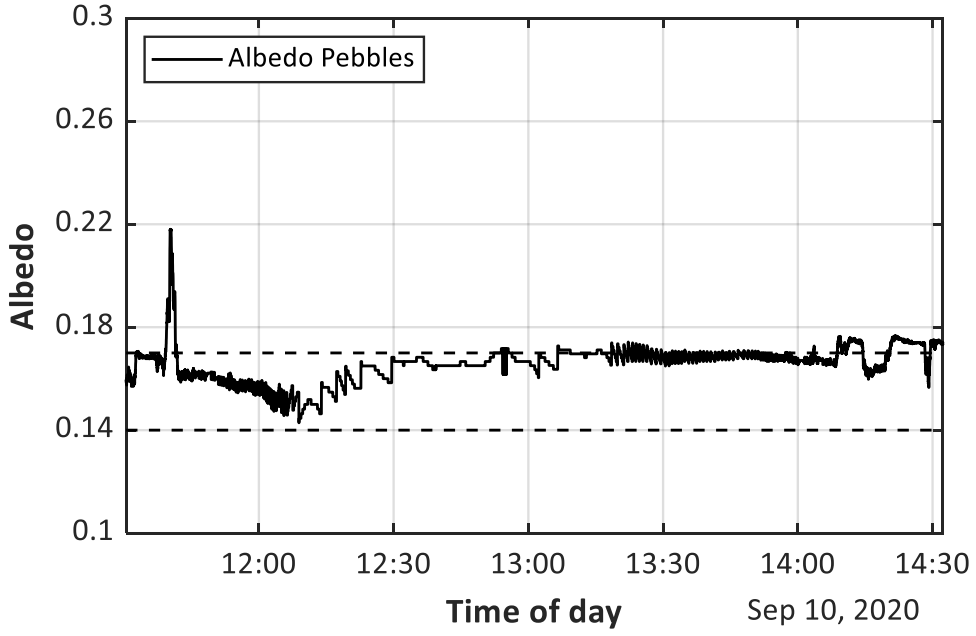

Figure 5.6: Measurement of ground albedo during a 4 hour period.

5.2. Validation of the model

In order to validate the model it is crucial that the experiment specifics like position and orientation are well-defined. Then in the model this setup can be recreated as accurately as possible. The model will be validated using two methods. Logically the first method is comparing it to the measured irradiance values. Secondly it will be compared to RADIANCE which is currently the most used software. This way not only do we see how accurate the model compared to the measurements but also how it compares to the state of the art model that currently exists and is the go-to model for these kind of problems.

This section will describe the experiments and setups that are used to validate the model and its comparison to measured data and RADIANCE.

5.2.1. Specular reflection setup and validation

As one of the main components of the newly proposed model is the possibility to account for specular reflections it is useful to create a setup in which these specular reflections occur in a predictable manner. This subsection will describe the setup and measurements of the experiment that is conducted to measure specular reflections and consequently its validation using our model and RADIANCE.
The first real validation experiment conducted will be done on the roof of the PVMD monitoring station. It was chosen to use 6 mirrors to produce the specular reflections. Firstly the glass façade at the side of the building was considered for this but it was found that using mirrors the result will be more clear-cut. The goal of this experiment is to measure a sizable specular reflection, the origin of the reflection does not really matter. It must be clear that due to the inaccuracy of the used setup it is expected nor is it the goal to very precisely simulate the measured values. The goal is to see if the simulations are in the same ballpark in terms of magnitude and timing. Using mirrors this goal was more easily accomplished.

First a location was chosen with as little obstructions as possible somewhere on the PVMD monitoring station. The best location was found on the backside of the roof shown in Figure 5.7.

The alignment of the mirrors was performed by using sun path calculations and projecting them on the roof of the PVMD monitoring station. This is done as follows: First of all it is known that the angle from the ray to the sensor must be the same as the angle to the sun due to Snell's law. This angle can be split up into two components: altitudal and azimuthal. The altitudal angle must be the same as well as the azimuthal angle. Using the altitudal angle the projected distance from the sensor to the point where the sensor sees the sun

(a) **(b)**

Figure 5.7: The used experimental setup for measuring specular reflections on the PVMD monitoring roof.

can be calculated using the principle shown in Figure 5.8 and then using Equation 5.2.

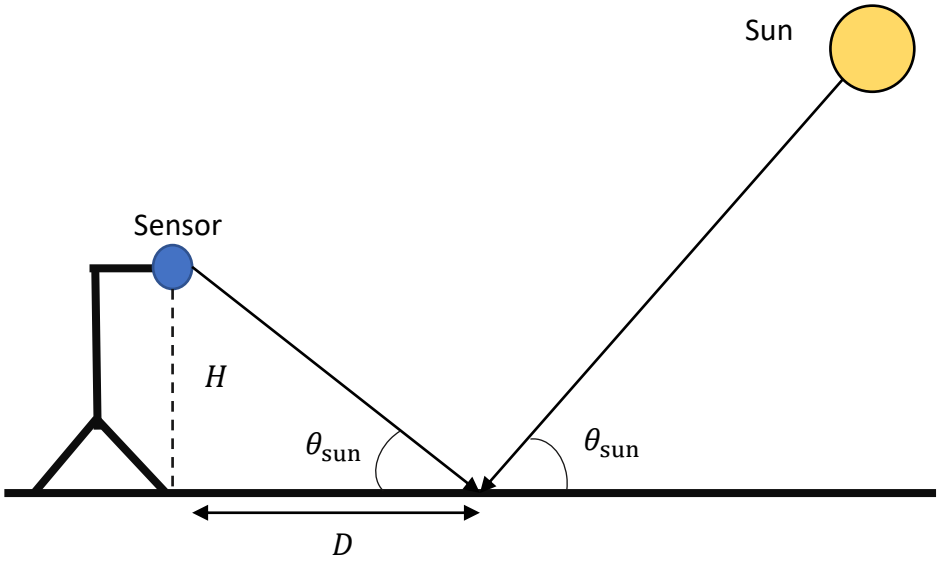

Figure 5.8: Graphical representation of at which distance D for sensor height H and solar altitude θ_{sun} a specular reflection will occur.

$$D = \frac{H}{\tan(\theta_{\text{sun}})} \tag{5.2}$$

Now the distance to the sensor is known the actual x and y coordinates of the sun on the roof must be calculated. Then centering the sensor in a 2D polar coordinate system where the azimuth is measured east from north as shown in Figure 5.9. It can be shown that the x and y coordinates will be given by Equation 5.3

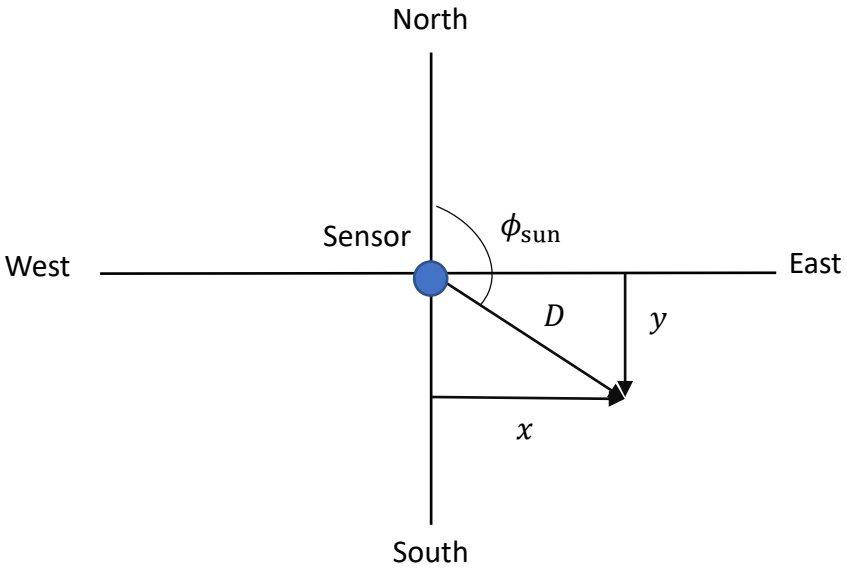

Figure 5.9: 2D representation of the geometry which shows how the coordinates of a specular reflection point can be calculated using the distance to the sensor and azimuth of the sun.

$$x_{\text{refl}} = D \cdot \cos(\phi_{\text{sun}})$$
$$y_{\text{refl}} = D \cdot \cos(\phi_{\text{sun}}) \tag{5.3}$$

Loading the position of the sensor into the 3D model an idea was formed of where to place the mirrors by plotting the projected sun path onto the roof as shown in Figure 5.10. Because it was challenging to align the

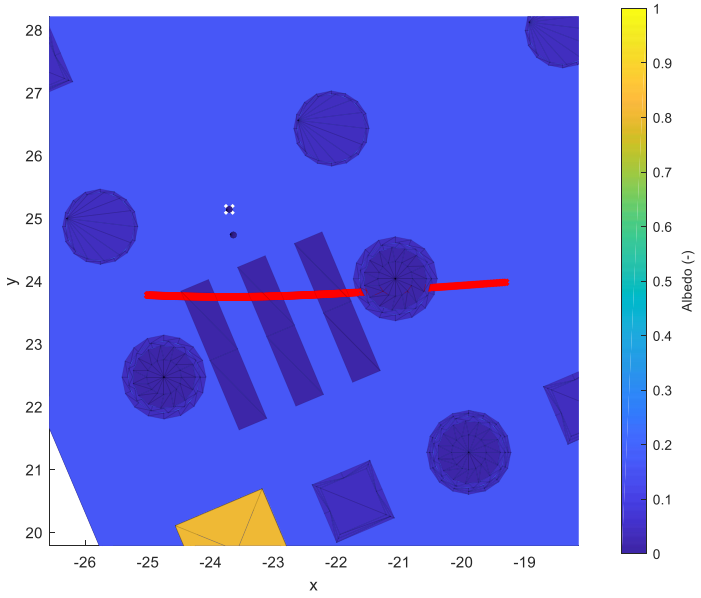

Figure 5.10: Sunpath as projected on the PVMD monitoring roof on where it would create a specular reflection on the bottom pyranometer.

mirrors an error margin is taken into account and the mirrors were placed in a range of where the sun path would surely pass through.

The pyranometer setup is the same as for the albedo measurements. So one pyranometer facing to the ground and one to the sky. The mirrors were placed in front on the floor in the range found using the sun path projection.

Now the setup is defined the measurements were taken. The measurements were taken on september the 15th 2020 from 10.00 in the morning to approximately 15.30 in the afternoon. Now the setup is known and the measurements are taken the validation can begin.

The first validation case will be as follows: For the RADIANCE model the following cases will be calculated: The bottom pyranometer will be simulated in both RADIANCE and our model. In RADIANCE the following conditions are used

1. One ambient bounce, 8192 ambient divisions and mirror reflectivity of 90 %.
2. Two ambient bounces, 8192 ambient divisions and mirror reflectivity of 90%.

These separations are made both differentiate simulation results for different amount of light bounces in RADIANCE. The mirror reflectivity is chosen to be 90 % as the base value. However this value is not fully known. Typically mirrors however have a reflectivity value around 90%. This value can be tweaked in future simulations.

Consequently our model is run for a primary resolution that divides the sky azimuth in 1.5 degree segments as well as the altitudal in 1.5 degree segments. Which means a resolution of 240x120. The secondary resolution will be divided into two degree segments so a resolution of 180x90. The results of this validation can be seen in Figure 5.11. As can be seen in all the models the trends are somewhat a like. The 3 specular reflection

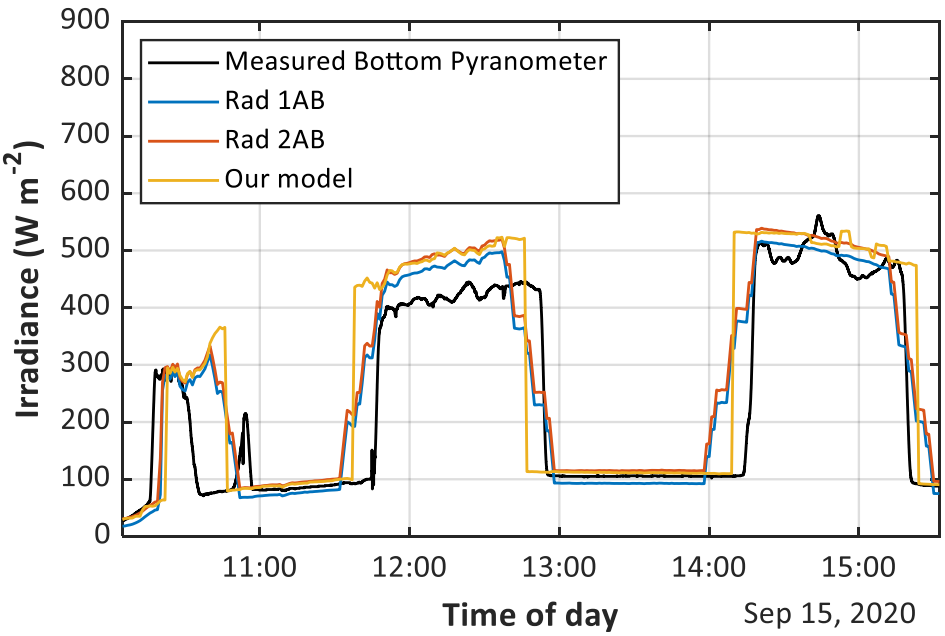

Figure 5.11: Measured irradiance on the bottom pyranometer for the specular reflection setup plotted against the RADIANCE results for both 1 and 2 ambient bounces and our model.

spikes caused by the 3 rows of mirrors can be clearly seen in all the models. However there are some notes to be placed by these results

- **Discontinuity in measured first specular reflection**: There is a clear discontinuity in the measured first specular reflection. It dissapears earlier than expected before it reappears right before 11.00 AM. The

suspected reason for this discontinuity is thought to be the crossing from one mirror plate to the other mirror plate. Even though they are in the same row of mirrors in the setup a misalignment can lead to the loss of the measured specular reflection. Also when looking at Figure 5.10 the border between the two mirrors is close to the projected sunpath. The fact that it is not 100% perfectly defined is due to the fact that the alignment is not very precise as mentioned before.

- **Timing mismatches**: The mismatch in timing can be seen in all models and differs for each row of mirrors. For the 1st row it is relatively late and for the 2nd row it is early. Therefore it is expected this is not due to the fact that the models are inaccurate but more due to the fact that the experimental alingment is not completely aligned with how the 3D models are defined

- **Magnitude mismatches**: The irradiance magnitude of all the models are all relatively close but there are still some mismatches. This can be due to the fact that the reflectivity of the mirror or surrounding materials can be different than as they were input in the models. The mirrors are not perfectly defined/calibrated so the reflectivity of the mirrors can be inaccurate. However to see the effect of different reflectivities a number of different simulations will be run. First the mirror reflectivity will be varied for both RADIANCE as well as our model. In this case only the RADIANCE model with two ambient bounces will be run as it is more accurate than the 1 bounce. The results for changing the mirror reflectivity to 85 % compared to 90 % can be seen in Figure 5.12 Another material that has a big effect on

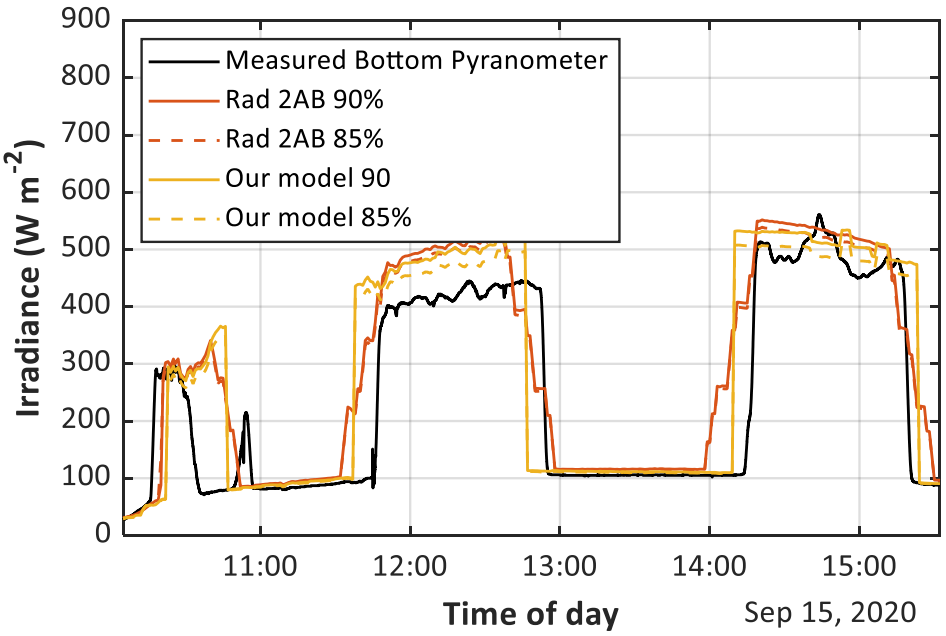

Figure 5.12: Measured irradiance on the bottom pyranometer for the specular reflection setup plotted against the RADIANCE results for both 2 ambient bounces and our model with mirror reflectivities of 90 and 85%.

the reflected irradiance on the bottom pyranometer is the pebble floor. Similarly two simulations are run with one pebble reflectivity of 0.17 and the other of 0.14. The results can be seen in Figure 5.13 It can be seen that for both varying pebble as well as mirror reflectivity it is possible to shift the outcome of the measurements. This shows that the reflectivity of the materials is still a source of error. Namely the mirrors however are likely to be a source of error due to the fact that no real measurements are performed to calculate the reflectivity of the mirrors.

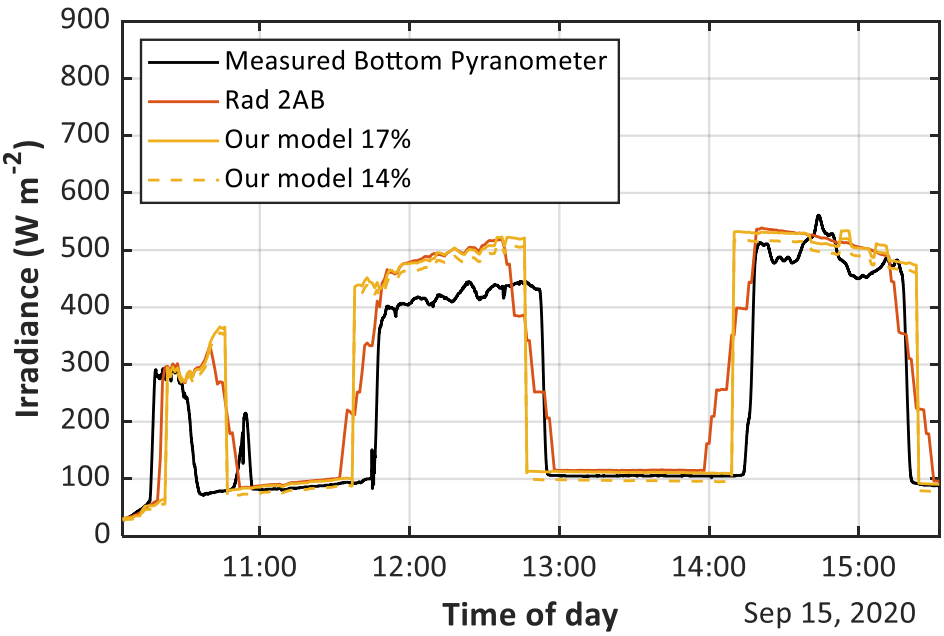

Figure 5.13: Measured irradiance on the bottom pyranometer for the specular reflection setup plotted against the RADIANCE results for both 2 ambient bounces and our model with pebble reflectivity of 0.17 and 0.14.

5.2.2. Validation for different sensors in the PVMD roof

Next to the measurements performed in the previous subsections there are also standard measurement devices on the PVMD monitoring station roof. 3 of these will be used for further validation. This validation will be over longer periods of time as these measuring devices are automatically monitoring irradiance during the entire year. The 3 sensors that are used are described below and shown in

- **Sensor 1**: this sensor is a reference cell on the fixed rack facing south with a tilt angle θ_m of 33 degrees. For sensor 1 an incidence angle modifier will be used because it is a reference cell and not a pyranometer. The glass plane in front of the cell affects the irradiance impinging and therefore a correction is needed. The used IAM model is the physical IAM model described in the theoretical background chapter. The 3D model can be simplified for this sensor to reduce computation time. The simplifications include the deletion of the big building behind the monitoring station shown in Figure C.1 in the Appendix C. Also the glass domes and structures on the monitoring station that can be deleted as they will hardly affect the irradiance impinging on this reference cell. A selection of these structures is shown in Figure C.2 also in Appendix C.

- **Sensor 2**: this sensor is a reference cell placed on the weathermast also facing south with a tilt angle θ_m of 20 degrees. The same physical IAM model will be used for this reference cell. The same simplifications in the 3D model can be made as for sensor 1 as the orientation and position is comparable.

- **Sensor 3**: this sensor is a pyranometer facing mostly east but perpendicular to the roof edge. The tilt of this pyranometer is 90 degrees. The simplification made for this sensor is only the deletion of the structures on the PVMD monitoring roof. The building behind the monitoring station cannot be deleted as it is still able to affect the irradiance on this pyranometer.

Figure 5.14. The first validation that will be performed for all 3 sensors is simulating the irradiance using our model for a week in September (22nd to the 28th) for all sensors. This will be compared to the measured irradiance. To see how the model performs compared to RADIANCE for this week of simulation. RADIANCE will also be run for this week. The simulation parameters are similar to before (which is 2 ambient bounces and 8192 ambient divisions). The result of this validation for sensor 1, 2 and 3 is shown in Figure 5.15, Figure 5.16 and Figure 5.17 It can be seen that in the beginning of each plot a piece of data is missing. This is due to the fact that the input data is invalid for this period because the DNI is blocked on the Solys2 station. Because

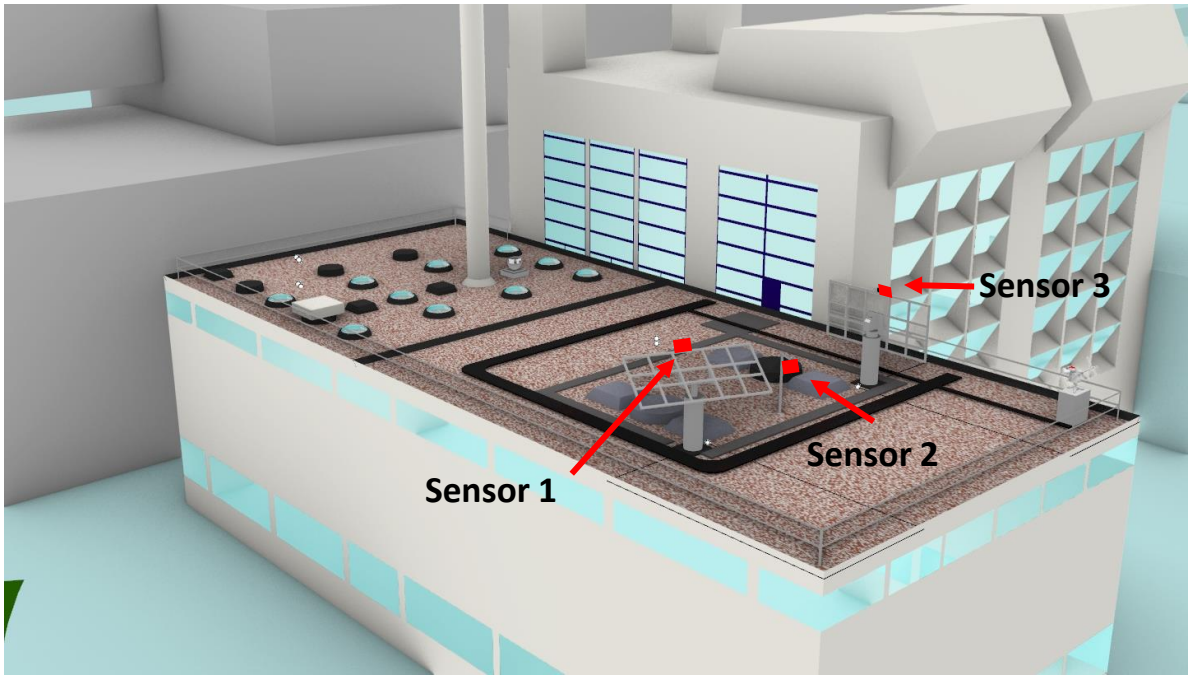

Figure 5.14: Position of the 3 sensors on the roof of the monitoring station.

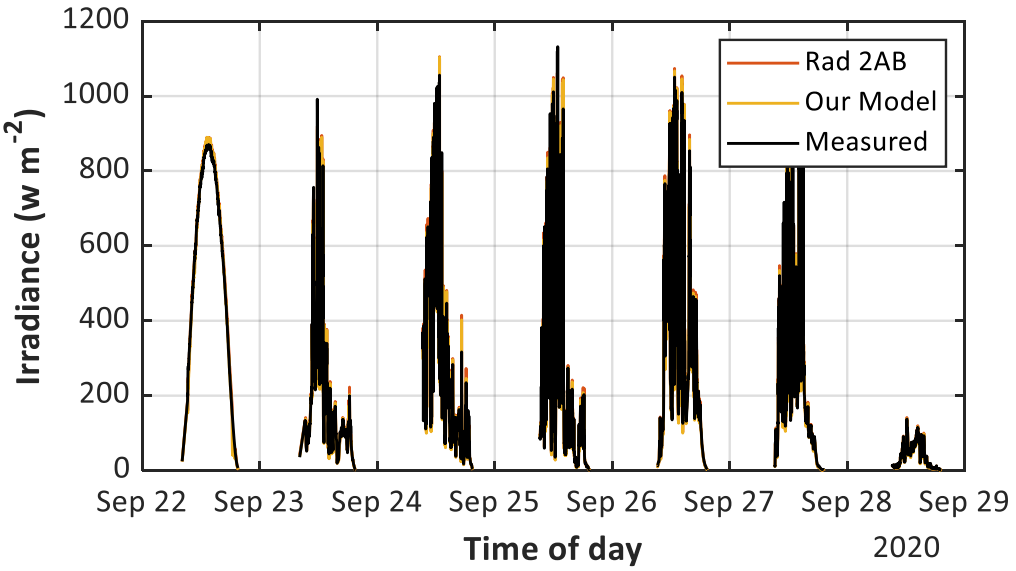

Figure 5.15: Irradiance on sensor 1 vs the measured irradiance for 1 week.

the input data is invalid the simulation results do not make sense to plot for this period. To get a graphical idea of how the these two simulation methods compare and to see the trend in their simulation method a dispersion plot is chosen. This dispersion plot shows the simulated irradiance vs the measured irradiance. This way trends like overestimation or underestimation for certain type of values can be more easily spotted. These dispersion plots are shown in Figure 5.18, Figure 5.19 and Figure 5.20.

To further evaluate the accuracy of the model vs the measured values two more error metrics will be calculated. The chosen error metrics are the (Normalized) Mean Bias Error or (*N*)*MBE* and the (Normalized) Root Mean Square Error or (*N*)*RMSE*. The equation for calculating the un-normalized *MBE* is shown in Equa-

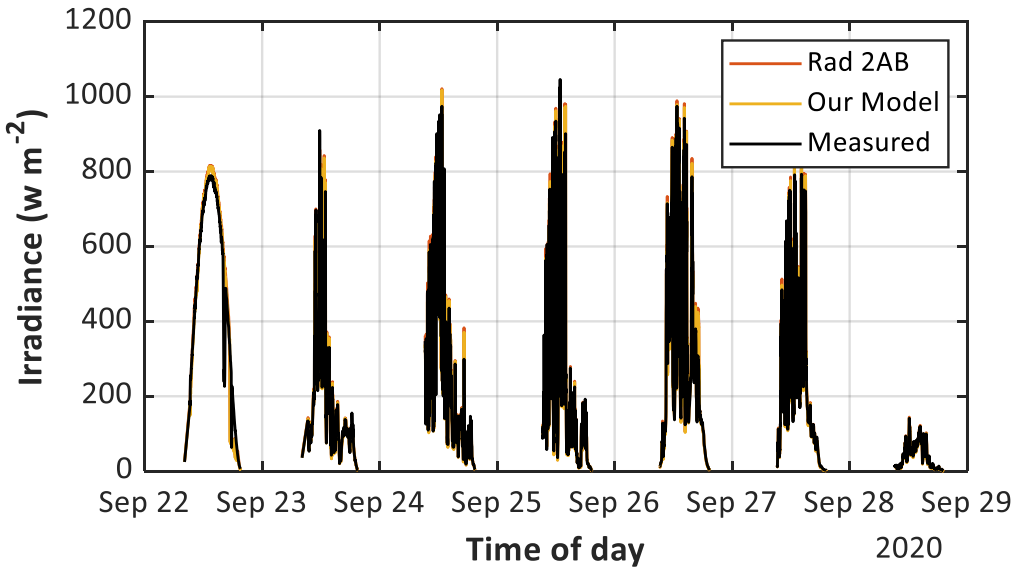

Figure 5.16: Irradiance on sensor 2 vs the measured irradiance for 1 week.

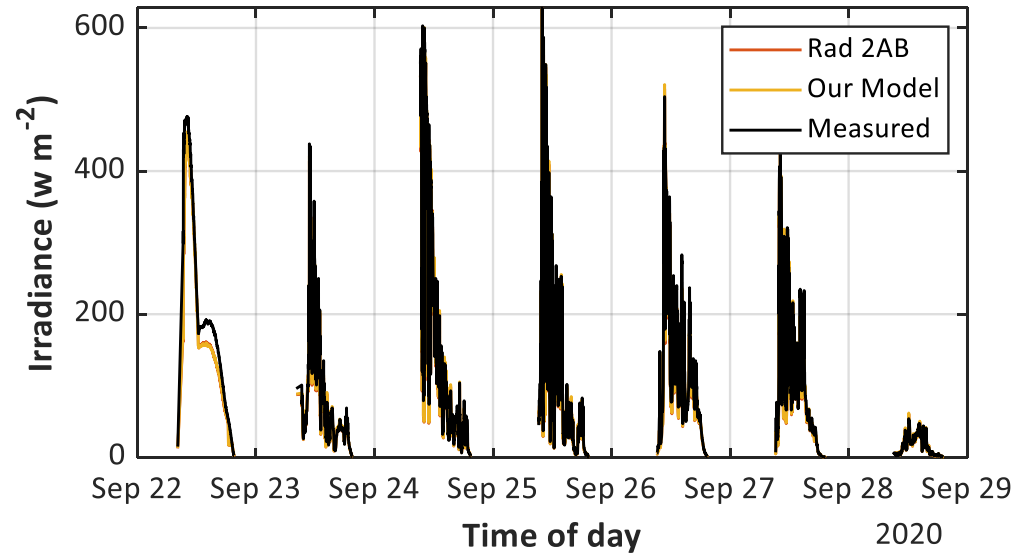

Figure 5.17: Irradiance on sensor 3 vs the measured irradiance for 1 week.

tion 5.6 and for the unnormalized *RMSE* in Equation 5.7

$$MBE = \sum_{i=1}^{N} \frac{(x_{\mathrm{i,m}} - x_{\mathrm{i,sim}})}{N} \tag{5.4}$$

$$RMSE = \sqrt{\sum_{i=1}^{N} \frac{(x_{\mathrm{m,i}} - x_{\mathrm{s,i}})^2}{N}} \tag{5.5}$$

In this equation N is the number of measurements $x_{i,m}$ the measured value and $x_{i,s}$ the simulated value. The normalized errors are then acquired by using equations Equation 5.6 and Equation 5.7. Where $\hat{x}_m$ is the average measured value.

$$NMBE = \frac{MBE}{\hat{x}_m} \tag{5.6}$$

$$NRMSE = \frac{RMSE}{\hat{x}_m} \tag{5.7}$$

In Table 5.2 the MBE and *RMSE* for all sensors and both our model and RADIANCE are tabulated.

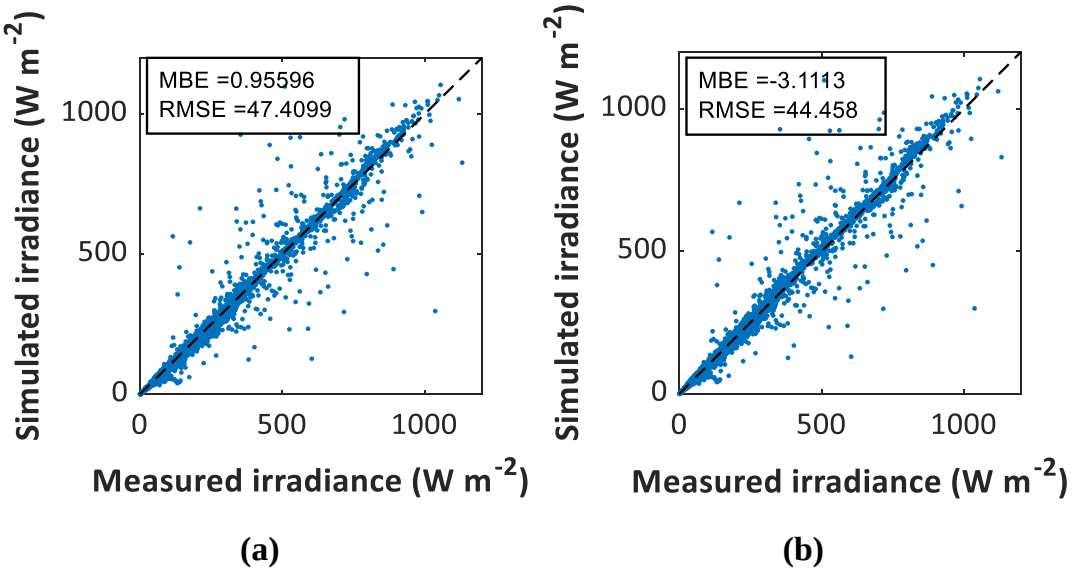

Figure 5.18: (a) Sensor 1 dispersion plot of simulated values using our model vs measured value including the *MBE* and *RMSE* for 1 week **(b)** Sensor 1 dispersion plot of simulated values using RADIANCE vs measured values including the *MBE* and *RMSE* for 1 week.

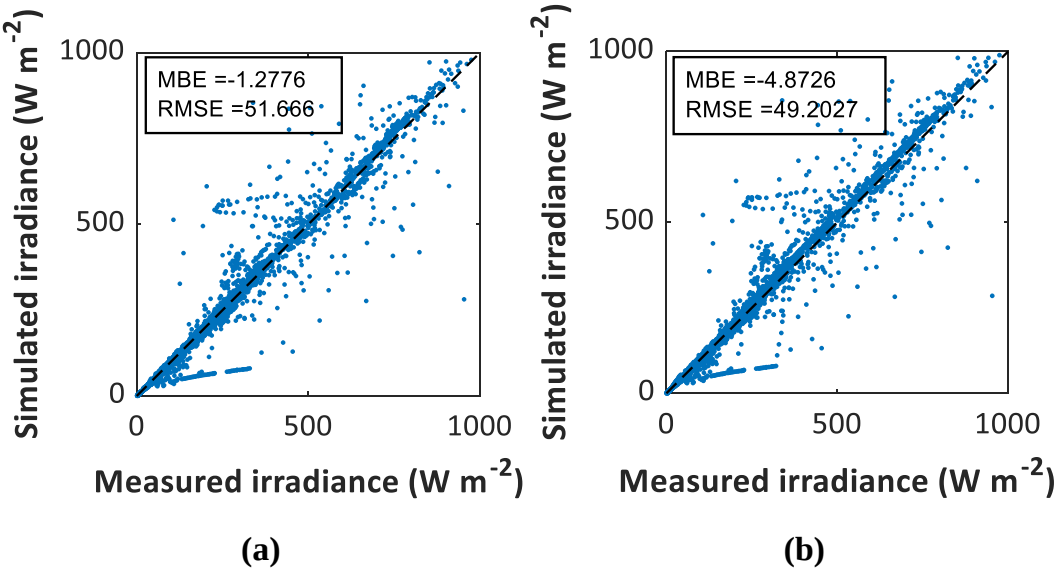

Figure 5.19: (a) Sensor 2 dispersion plot of simulated values using our model vs measured value including the *MBE* and *RMSE* for 1 week.**(b)** Sensor 2 dispersion plot of simulated values using RADIANCE vs measured values including the *MBE* and *RMSE* for 1 week.

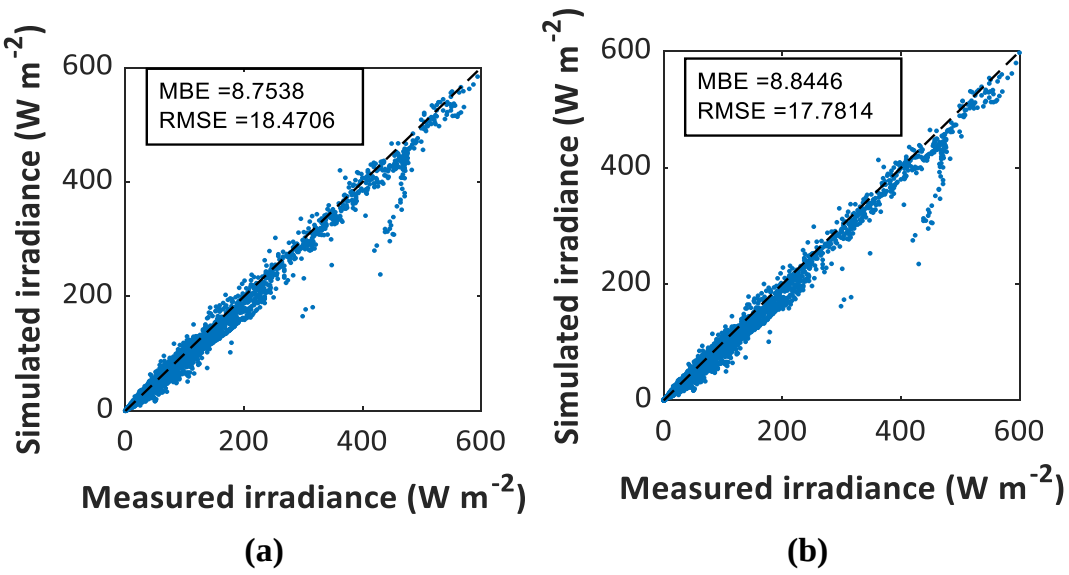

Figure 5.20: (a) Sensor 3 dispersion plot of simulated values using our model vs measured value including the *MBE* and *RMSE* for 1 week **(b)** Sensor 3 dispersion plot of simulated values using RADIANCE vs measured values including the *MBE* and *RMSE* for 1 week.

Table 5.2: *MBE* and *RMSE* error for all 3 sensors for both our model and RADIANCE.

	Sensor 1 Our model	**Sensor 1 RADIANCE**
MBE(%)	0.96%	-3.11%
RMSE	47.41%	44.45%

	Sensor 2 Our model	**Sensor 2 RADIANCE**
MBE(%)	1.28	-4.87
RMSE(%)	51.66	49.21

	Sensor 3 Our model	**Sensor 3 RADIANCE**
MBE(%)	8.76	8.44
RMSE(%)	18.47	17.78

A few key points can be taken from these dispersion plots. Overall the model seems to perform very well. With only one bounce it has a similar or even lower Mean Bias Error than RADIANCE which uses two bounces. Most deviatoins seem to be a small underestimation for both our model as well as RADIANCE. This makes sense as due to limiting bounces in reflection automatically a fraction of reflected light will be missing in the simulation compared to reality.

There is a big difference in the *RMSE* value size for sensors 1 and 2 two compared to sensor 3. This difference can be explained due to the difference in the sensor type. Sensor 1 and 2 are reference cells. They measure the irradiance with a very low response time. The current generated is correlated to the incoming irradiance and this has a relatively low delay time. However the pyranometer on the dual-axis tracker has a higher response time. This is due to the fact a pyranometer uses the temperature of a black surface to measure irradiance. Because the input values of the model (DNI and DHI) are also measured with pyranometers their response times are similar. Due to the mismatches that can occur for sensors with different response nature for some cases the error can be very large. Because the *RMSE* is an absolute value these values do not cancel out over

a long period and causes the higher values of the *RMSE* for sensors 1 and 2.

Also it can be seen that some outliers occur in close to proximity to eachother. These are expected to be caused by geometry mismatches. For example if in reality the sun is not yet blocked but it is blocked by a building in our model this can cause the simulated values to be lower than the measured values.

To get more information of the errors that appear in our model the normalized *MBE* and *RMSE* given by Equation 5.6 and Equation 5.7 are plotted for an extended period of time. This is from mid-August until mid-October. The results of these error calculations can be seen in Figure 5.21 and Figure 5.22.

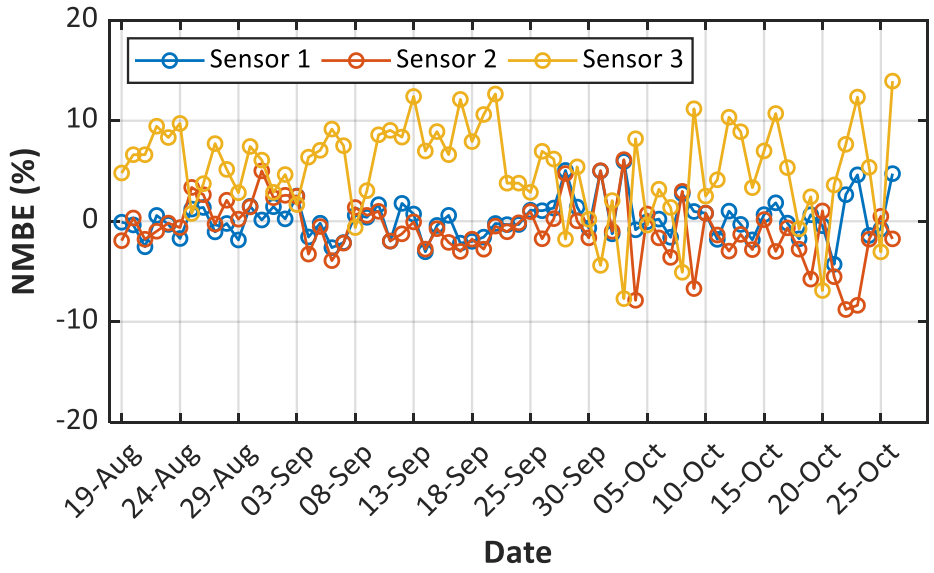

Figure 5.21: Normalized mean bias error for all 3 sensors for a long period of time stretching from mid-August to mid-October.

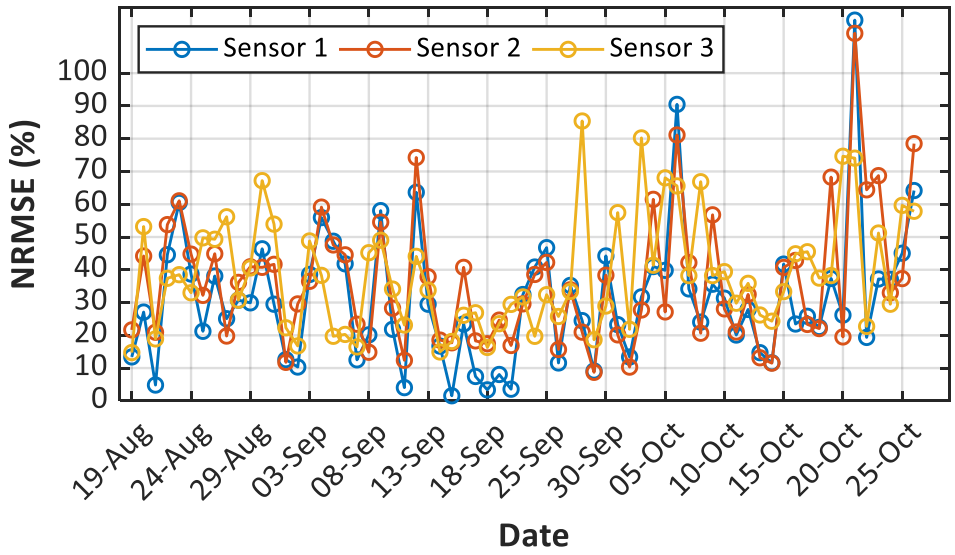

Figure 5.22: Normalized root mean square error for all 3 sensors for a long period of time stretching from mid-August to mid-October.

5.3. Summary

This chapter has described the experiments that were performed in order to validate the proposed model framework. It has presented its results and developed the error metrics neccessary. In doing this this chapter is able to answer the following research questions":

1. **How does the performance of the proposed model compare to measured data and existing models?**:

   - *How does the model perform for cases where irradiance is mostly due to specular reflections?*
     Outdoor measurements show that the model is able to model the relevant characteristics of the irradiance profile when a large fraction of irradiance is due to specular reflections. The results show that there is a good match between the measurements and the reflected irradiance in terms of magnitude and timing. 3 sizable specular reflections caused by mirrors were measured and appeared in the same time region in both our model as well as RADIANCE. In the performed validation the timing-mismatches and magnitude-deviations that occur are expected to be caused by inaccuracies in the experimental setup and not caused by flaws in the model. This is expected because our model performs very similar to the very well validated RADIANCE software.
   - *How does the model perform over long periods of time for different orientations and weather conditions?*
     The model is able to accurately model for different positions on the PVMD monitoring roof over longer periods of time. To evaluate the accuracy different error metrics were calculated. The *MBE* and *RMSE* errors of both our model as well as RADIANCE are shown in Table 5.3.

     Table 5.3: *MBE* and *RMSE* error for all 3 sensors for both our model and RADIANCE.

	Sensor 1 Our model	**Sensor 1 RADIANCE**
MBE	0.96%	-3.11%
RMSE	47.41%	44.45%

	Sensor 2 Our model	**Sensor 2 RADIANCE**
MBE(%)	1.28	-4.87
RMSE(%)	51.66	49.21

	Sensor 3 Our model	**Sensor 3 RADIANCE**
MBE(%)	8.76	8.44
RMSE(%)	18.47	17.78

     The *MBE* is close to 1 % for sensors 1 and 2 and therefore even seems to perform better than the simulations done in RADIANCE. For sensor 3 the errors are substantially larger with a MBE of around 9% for our model and 8.5 % for RADIANCE. This is mostly caused by the limitatoins of the proposed simulation model that is only able to take into account 1 bounce. Also the inaccuracy of the input *DHI* is likely to be a substantial source of error.

     The *RMSE* is very high for both our model as well as RADIANCE especially for sensors 1 and 2 (which are reference cells). This high *RMSE* can be explained due to mismatches in response time for different type of sensors used. This suspicion is confirmed by the results from sensor 3 which has a similar response time to the *DHI* and *DNI* sensors.

6

Conclusions and recommendations

The primary goal of this thesis was to develop and further improve an irradiance simulation model that works for PV systems in a complex urban environment. To achieve this goal the research questions and objectives formulated in the introduction were answered throughout the thesis. Below the answers to the research questions and objectives are summarized:

1. **What type of reflections do we need to model in order to acccurately simulate the irradiance impinging on a PV module in a complex environment?**

   - *How do we accurately and efficiently model different reflective properties?*
     The proposed model differentiates between two different types of surfaces or reflectors: diffuse (Lambertian) and ideally specular.

     For the lambertian surfaces: it is chosen to cast rays in all directions evenly and find the respective incident irradiance from only the sky coming in. This simulates the isotropic scattering behaviour as described by the BRDF of a lambertian. The incident irradiance on the lambertian surface can then be calculated using Equation 6.1.

     $$G_{\text{lamb}}^{\text{dir,surface}} = \sum_i L_{\text{SP}_{2,i}} \cdot \Omega_{\text{SP}_{2,i}} \cdot \cos(AOI) \tag{6.1}$$

     For the specular surfaces: In the case of an ideal specular reflector, it is considered that the solar cell receives the radiance of a single sky patch incident on the reflector. The position of the sky patch of interest can be determined by mirroring the vector that connects the solar cell and the reflector. This vector is determined using Equation 6.2

     $$\mathbf{r}_2 = 2 \cdot (\mathbf{r}_1 \cdot \mathbf{n}_{\text{specular}}) \cdot \mathbf{n}_{\text{specular}} - \mathbf{r}_1 \tag{6.2}$$

   - *How do we calculate irradiance coming from different type of reflectors?*:

     Once the irradiance on the different type of reflectors is determined, the contribution to the reflected irradiance on the solar cell is determined using the BRDF function of the reflector.

     For the lambertian surfaces: The amount of irradiance due to a lambertian surface can be written as Equation 6.3

     $$\mathrm{d}G_{\text{m}}^{\text{refl,lambert}} = \rho_{\text{j}} \cdot G_{\text{m}}^{\text{dir,j}} \cdot \mathrm{d}F_{\text{cell}\rightarrow \text{SP}_{\text{L},j}} \tag{6.3}$$

     For the specular surfaces: In the case of a specular reflector the contibution to the reflected irradiance on the solar cell is expressed in Equation 6.4. For a mirror R_{s} is a constant which equals 1 if the mirror is ideal. For any other specular reflector (dielectric) it is the Fresnel Coefficient dependent on the angle of incidence and the refractive index.

     $$\mathrm{d}G_{\text{m}}^{\text{refl,mirror}} = R_{\text{s}} \cdot L_{\text{SP}_2} \cdot (\mathbf{n}_{\text{specular}} \cdot \mathbf{r}_1) \cdot \mathrm{d}\Omega_{\text{SP}_2} \tag{6.4}$$

2. **Create a model that is structured in a way that accelerates simulation**

   - *Subdivide the model into decoupled blocks to allow efficient simulation.*
     This objective has been fulfilled by the proposed irradiance model by decoupling of the geometrical problem from the illumination problem. The intersections, (reflected) ray directions, incidence angles, solid angles and other geometrical properties are all calculated independently from the sky conditions. Also the optical properties of the materials are not tangled with the sky conditions. Hence, using this geometry data, which can be solved in a high resolution beforehand, combined with the sky conditions the irradiance simulation can run. This decoupled structure allows efficient simulation over longer time periods because the geometrical problem does not have to be recalculated for each different sky condition.
   - *Structure the model so that it allows us to perform spectrally resolved simulations and model surfaces with time dependent reflective surface properties.*
     This objective has been reached by the same decoupling principle as mentioned above. The decoupling of the reflectivity values from the ray tracing geometrical solution allows to solve the irradiance on the cell considering the spectral reflectivity of the surface without the need to repeat the time consuming ray-tracing simulations. For the same reasons, the model also allows to input different reflectivity values for each simulated time instant. This allows to model Lambertian surfaces with time-varying reflectivity properties.

3. **How does the performance of the proposed model compare to measured data and existing models?**

   - *How does the model perform for cases where irradiance is mostly due to specular reflections?*
     Outdoor measurements show that the model is able to model the relevant characteristics of the irradiance profile when a large fraction of irradiance is due to specular reflections. The results show that there is a good match between the measurements and the reflected irradiance in terms of magnitude and timing. 3 sizable specular reflections caused by mirrors were measured and appeared in the same time region in both our model as well as RADIANCE. In the performed validation the timing-mismatches and magnitude-deviations that occur are expected to be caused by inaccuracies in the experimental setup and not caused by flaws in the model. This is expected because our model performs very similar to the very well validated RADIANCE software.
   - *How does the model perform over long periods of time for different orientations and weather conditions?*
     The model is able to accurately model for different positions on the PVMD monitoring roof over longer periods of time. To evaluate the accuracy different error metrics were calculated. The *MBE* and *RMSE* errors of both our model as well as RADIANCE are shown in Table 6.1.

Table 6.1: *MBE* and *RMSE* error for all 3 sensors for both our model and RADIANCE.

	Sensor 1 Our model	**Sensor 1 RADIANCE**
MBE	0.96%	-3.11%
RMSE	47.41%	44.45%

	Sensor 2 Our model	**Sensor 2 RADIANCE**
MBE(%)	1.28	-4.87
RMSE(%)	51.66	49.21

	Sensor 3 Our model	**Sensor 3 RADIANCE**
MBE(%)	8.76	8.44
RMSE(%)	18.47	17.78

The *MBE* is close to 1 % for sensors 1 and 2 and therefore even seems to perform better than the simulations done in RADIANCE. For sensor 3 the errors are substantially larger with a *MBE* of

around 9% for our model and 8.5 % for RADIANCE. This is mostly caused by the limitatoins of the proposed simulation model that is only able to take into account 1 bounce. Also the inaccuracy of the input *DHI* is likely to be a substantial source of error.

The *RMSE* is very high for both our model as well as RADIANCE especially for sensors 1 and 2 (which are reference cells). This high *RMSE* can be explained due to mismatches in response time for different type of sensors used. This suspicion is confirmed by the results from sensor 3 which has a similar response time to the *DHI* and *DNI* sensors.

6.1. Recommendations

The following recommendations are proposed based on the results of this work:

- **Computational optimization**: The most computationally demanding part of the developed model is the determination of the intersections between the rays and the surrounding geometry. The implementation of the model proposed in this thesis is not fully optimized from a computational perspective because the physical models (and not the optimization of the code) was the main goal of this thesis project. Many computational techniques can be used to enhance the speed of this type of code. Further research and optimization will greatly enhance the speed of the code and therefore also allow the use of higher resolution and accuracy.
- **Inclusion of higher order reflections**: Due to further optimization of computational efficiency the inclusion of higher order reflections can be considered. By doing this the accuracy of situations where the reflected irradiance takes up a large fraction can be improved. Currently the computation time would increase too much and therefore the amount of bounces is limited to 1.
- **Validation for different conditions**: Currently the validation performed is limited to only one location, the roof of the PVMD monitoring station in Delft, the Netherlands. To further improve the reliability of the model it needs to be validated for different locations, different climates and different seasons. This can provide a broader picture of the validity of the proposed model.
- **Improvement of specular alignment**: The measurement of the specular setup could be improved by creating a setup that allows easier alignment. Doing this would help to minimize the deviations between the measured and simulated irradiance which are not due to the limitations of the proposed model.
- **Implement spectrally resolved simulations**: Currently the model is structured in a way that allows spectral simulations. However a validation study was not yet performed in this thesis. This is due to the fact that the generated sky maps are not spectrally resolved. For future research creating this sky maps can lead to spectrally resolved simulations which are esspecially useful for simulation of tandem devices.

A

DHI correction

The input values for the sky model come from the Solys2 station on the roof and consist of a *DNI*, *DHI* and *GHI*. Only the *DNI* and *DHI* are used as actual model inputs. The *DHI* however must be corrected first. Why and how this is done will be explained in this section.

Because a lot of light can be reflected from the surroundings to the *DHI* sensor of the Solys2 station this measurement will not only consist of diffuse irradiance coming from the sky. This is required for the model input. Therefore the measurement will be corrected to a case for a free horizon. This is done by running simulation for the location of the Solys2 using RADIANCE. RADIANCE is used as it is the most provenly accurate ray tracing simulation tool.

For the first iteration the measured *DNI* and *DNI* at the Solys2 station will be used. The *GHI* at the Solys2 station will then be calculated using RADIANCE. This will be compared to the measured *GHI* at the Solys2 station. If the *GHI* simulated is higher than the measured *GHI* the difference Δ_{DHI} will be subtracted of from the *DHI*. If this difference Δ_{DHI} is negative it can be seen as an addition and the sign will always be right. Here we assume that the only inaccuracy in *GHI* measurement comes from the *DHI* inaccuracy. The *DNI* is less sensitive to inaccuracies or effects of the surroundings like reflections.

$$\Delta_{DHI} = GHI_{\text{sim}} - GHI_{\text{meas}} \tag{A.1}$$

$$DHI_{\text{new}} = DHI_{\text{old}} - \Delta_{DHI} \tag{A.2}$$

After that the simulation is rerun again with this new *DHI* and the same principle is applied. The correction is aborted within 10 runs or when the measured *GHI* is within 0.5% of the simulation value . The basic principle of the *DHI* correction is shown schematically in the flowchart in Figure A.1.

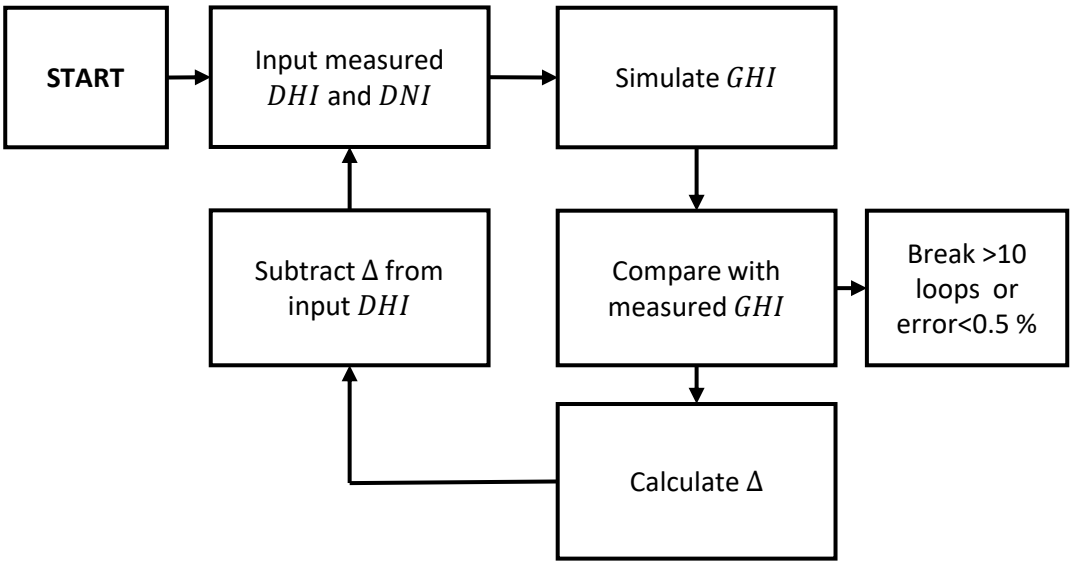

Figure A.1: Flowchart of the *DHI* correction method

B

Horicatcher validation of 3D Model

Also pictures will be taken with the horicatcher device which takes a 360 degree picture using a curved mirror and a camera placed directly above it. The horicatcher pictures let us derive the azimuthal orientation and position of the different objects and surfaces. The result of the horicatcher device can be seen in Figure B.1 These measurements could be validated by matching the skyline generated by the horicatcher to the skyline

Figure B.1: Horicatcher image result of the PVMD monitoring station

that can be seen using the Rhino Model. The result of this validation for a location on the PVMD monitoring roof can be seen in Figure B.2. This was a way to check whether the new measurements were correct and matched reality.

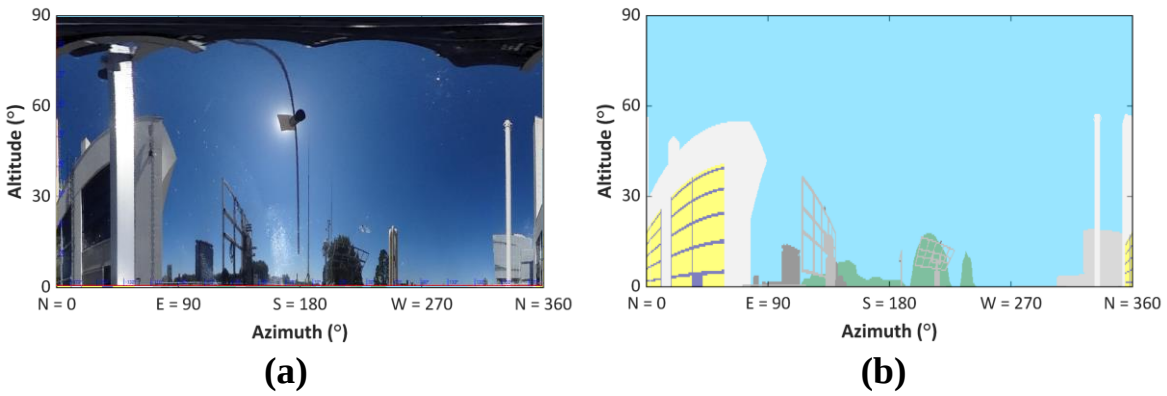

Figure B.2: **(a)**Generated skyline profile using MATLAB **(b)** the horicatcher image generated using meteonorm

C

3D Model simplifications

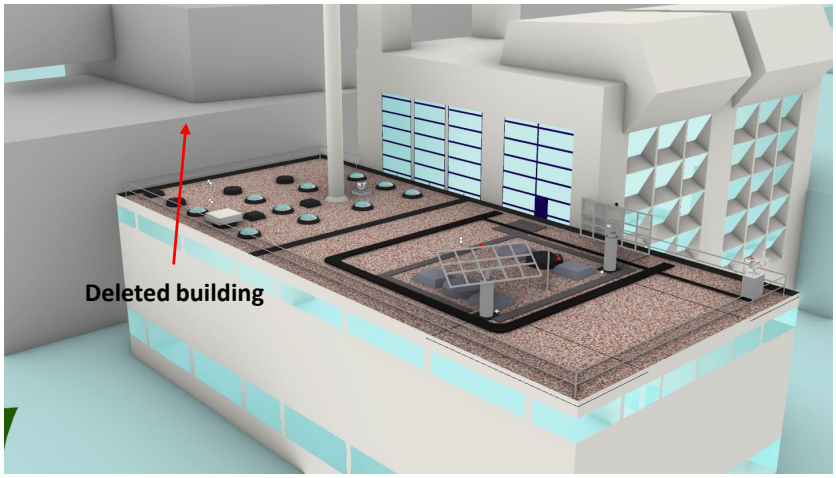

Figure C.1: Deleted building at back of PVMD monitoring roof for simplification of modelling sensors 1 and 2

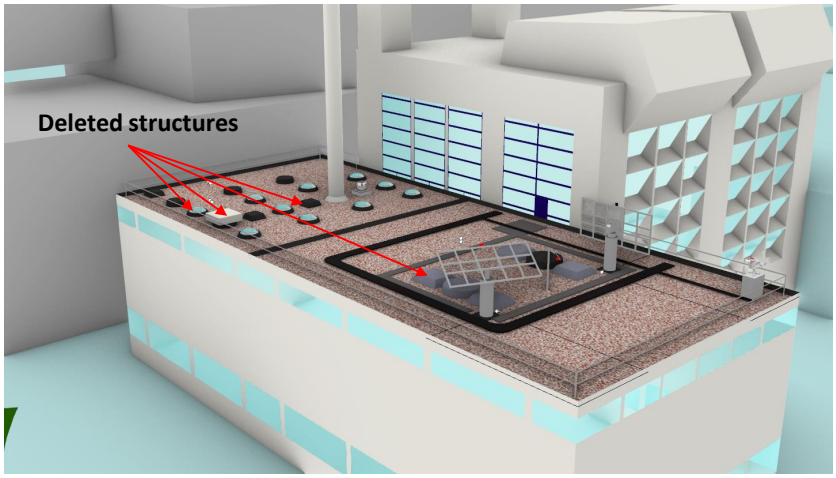

Figure C.2: Deleted structures on the PVMD monitoring roof for simplification of modelling all sensors

D

Flowchart of using our model and RADIANCE

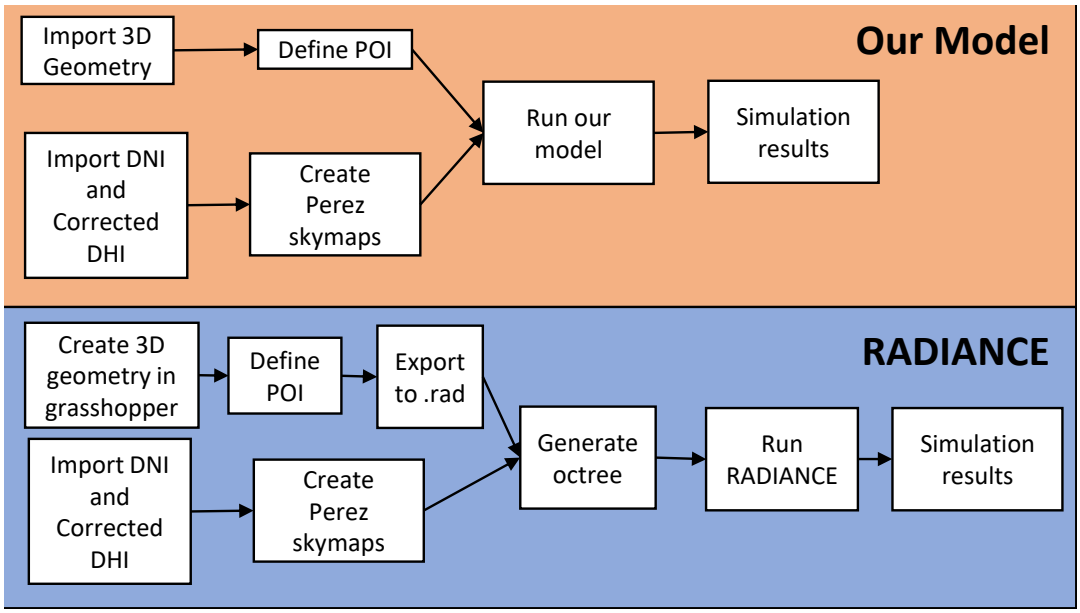

Figure D.1: Flowchart of how our model should be used and how RADIANCE is used

Bibliography

[1] Basic principles of surface reflectance. URL https://www.cs.cmu.edu/afs/cs/academic/class/15462-f09/www/lec/lec8.pdf.

[2] Radiosity (radiometry) - wikipedia. https://en.wikipedia.org/wiki/Radiosity_(radiometry). (Accessed on 05/22/2020).

[3] Glas maakt rotterdam cs transparant en toegankelijk • glas in beeld.

[4] Physical iam model, . URL https://pvpmc.sandia.gov/modeling-steps/1-weather-design-inputs/shading-soiling-and-reflection-losses/incident-angle-reflection-losses/ashre-model/.

[5] Hay and davies sky diffuse model, . URL https://pvpmc.sandia.gov/modeling-steps/1-weather-design-inputs/plane-of-array-poa-irradiance/calculating-poa-irradiance/poa-sky-diffuse/hay-sky-diffuse-model/.

[6] Physical iam model, . URL https://pvpmc.sandia.gov/modeling-steps/1-weather-design-inputs/shading-soiling-and-reflection-losses/incident-angle-reflection-losses/physical-model-of-iam/.

[7] Reindl sky diffuse model, . URL https://pvpmc.sandia.gov/modeling-steps/1-weather-design-inputs/plane-of-array-poa-irradiance/calculating-poa-irradiance/poa-sky-diffuse/reindl-sky-diffuse-model/.

[8] View factor models. URL https://pvpmc.sandia.gov/pv-research/bifacial-pv-project/bifacial-pv-performance-models/ray-tracing-models-for-backside-irradiance/view-factor-models/.

[9] Obtaining good transmission (%t) and reflection (%r) measurements, September 2011. URL http://www.vacuumcoating.info/obtaining-good-transmission-t-and-reflection-r-measurements#image1.

[10] International technology roadmap for photovoltaic. 2019.

[11] Sep 2019. URL https://sakibsaikia.github.io/graphics/2019/09/10/Deriving-Lambertian-BRDF-From-First-Principles.html.

[12] International technology roadmap for photovoltaic. 2020.

[13] Tomas Akenine-Mller, Eric Haines, and Naty Hoffman. *Real-Time Rendering, Fourth Edition*. A. K. Peters, Ltd., USA, 4th edition, 2018. ISBN 0134997832.

[14] Stanislav Darula and Richard Kittler. Cie general sky standard defining luminance distributions. 09 2002.

[15] EIA. International energy outlook 2019 with projections to 2050. 09 2019. doi: 10.5539/esr.v7n2p1.

[16] Martin Estgren Erik S. V. Jansson, Rasmus Hedin. Monte carlo raytracing from scratch, November 2017. (Accessed on 14-05-2020).

[17] Bram Greve. Reflections and refractions in ray tracing. 12 2006.

[18] Wolfgang Heidrich. Computing the barycentric coordinates of a projected point. *Journal of Graphics Tools*, 10(3):9–12, 2005. doi: 10.1080/2151237X.2005.10129200. URL https://doi.org/10.1080/2151237X.2005.10129200.

[19] Kipp Zonen. *Solys2 Instructoin Manual*. Kipp Zonen B.V, Delft, The Netherlands, 2017.

[20] Greg Ward Larson and Rob Shakespeare. *Rendering With Radiance: The Art And Science Of Lighting Visualization*. Booksurge Llc, 2004. ISBN 0974538108.

[21] B. Marion, S. MacAlpine, C. Deline, A. Asgharzadeh, F. Toor, D. Riley, J. Stein, and C. Hansen. A practical irradiance model for bifacial pv modules. In *2017 IEEE 44th Photovoltaic Specialist Conference (PVSC)*, pages 1537–1542, 2017.

[22] Jack Minnet. The rendering equation and brdfs – jackminnet. https://jackmin.home.blog/2018/08/17/the-rendering-equation-and-brdfs/, August 2018. (Accessed on 14-05-2020).

[23] Chuck Moidel. Bi-directional reflectance distribution functions. URL https://web.cs.wpi.edu/~emmanuel/courses/cs563/write_ups/chuckm/chuckm_BRDFs_overview.html.

[24] Hartmut Nussbaumer, Gaby Janssen, Djaber Berrian, Bruno Wittmer, Markus Klenk, Thomas Baumann, Franz Baumgartner, Marco Morf, Antonius Burgers, Joris Libal, and André Mermoud. Accuracy of simulated data for bifacial systems with varying tilt angles and share of diffuse radiation. *Solar Energy*, 197:6 – 21, 2020. ISSN 0038-092X. doi: https://doi.org/10.1016/j.solener.2019.12.071. URL http://www.sciencedirect.com/science/article/pii/S0038092X1931285X.

[25] Astronomical Applications Department of the U.S. Naval Observatory reproduced from The Astronomical Almanac Online, produced by the U.S. Naval Observatory, and H.M. Nautical Almanac Office. International technology roadmap for photovoltaic. 201.

[26] Poorya Ooshaksarei, Kamaruzzaman Sopian, Rozli Zulkifli, Mohammad Alghoul, and Saleem Zaidi. Characterization of a bifacial photovoltaic panel integrated with external diffuse and semimirror type reflectors. *International Journal of Photoenergy*, 2013, 05 2013. doi: 10.1155/2013/465837.

[27] R. Perez, R. Seals, and J. Michalsky. All-weather model for sky luminance distribution—preliminary configuration and validation. *Solar Energy*, 50(3):235 – 245, 1993. ISSN 0038-092X. doi: https://doi.org/10.1016/0038-092X(93)90017-I. URL http://www.sciencedirect.com/science/article/pii/0038092X9390017I.

[28] Richard Perez, Pierre Ineichen, Robert Seals, Joseph Michalsky, and Ronald Stewart. Modeling daylight availability and irradiance components from direct and global irradiance. *Solar Energy*, 44(5): 271 – 289, 1990. ISSN 0038-092X. doi: https://doi.org/10.1016/0038-092X(90)90055-H. URL http://www.sciencedirect.com/science/article/pii/0038092X9090055H.

[29] Naveed Rehman and Muhammad Uzair. The proper interpretation of analytical sky view factors for isotropic diffuse solar irradiance on tilted planes. *Journal of Renewable and Sustainable Energy*, 9, 10 2017. doi: 10.1063/1.4993069.

[30] R. Santbergen, V.A. Muthukumar, R.M.E. Valckenborg, W.J.A. van de Wall, A.H.M. Smets, and M. Zeman. Calculation of irradiance distribution on pv modules by combining sky and sensitivity maps. *Solar Energy*, 150:49 – 54, 2017. ISSN 0038-092X. doi: https://doi.org/10.1016/j.solener.2017.04.036. URL http://www.sciencedirect.com/science/article/pii/S0038092X17303298.

[31] Carsten Schinke, Malte R. Vogt, and Karsten Bothe. *Optical Modeling of Photovoltaic Modules with Ray Tracing Simulations*, chapter 3, pages 27–91. John Wiley & Sons, Ltd, 2018. ISBN 9781119364214. doi: 10.1002/9781119364214.ch3. URL https://onlinelibrary.wiley.com/doi/abs/10.1002/9781119364214.ch3.

[32] James R. Shell. Bidirectional reflectance : An overview with remote sensing applications measurement. 2004.

[33] Ismail Shoukry, Joris Libal, Radovan Kopecek, Eckard Wefringhaus, and Jürgen Werner. Modelling of bifacial gain for stand-alone and in-field installed bifacial pv modules. *Energy Procedia*, 92:600 – 608, 2016. ISSN 1876-6102. doi: https://doi.org/10.1016/j.egypro.2016.07.025. URL http://www.sciencedirect.com/science/article/pii/S1876610216304520. Proceedings of the 6th International Conference on Crystalline Silicon Photovoltaics (SiliconPV 2016).

[34] E. A. Sjerps-Koomen, E. Alsema, and W. Turkenburg. A simple model for pv module reflection losses under field conditions. *Solar Energy*, 57:421–432, 1996.

[35] Arno Smets, Klaus Jäger, Olindo Isabella, R.A.C.M.M. Van Swaaij, and Miro Zeman. *Solar Energy - The physics and engineering of photovoltaic conversion, technologies and systems*. 02 2016. ISBN 9781906860325.

[36] W. Soto, S.A. Klein, and W.A. Beckman. Improvement and validation of a model for photovoltaic array performance. *Solar Energy*, 80:78–88, 01 2006. doi: 10.1016/j.solener.2005.06.010.

[37] Xingshu Sun, Mohammad Khan, Chris Deline, and Muhammad Alam. Optimization and performance of bifacial solar modules: A global perspective. *Applied Energy*, 212, 09 2017. doi: 10.1016/j.apenergy.2017.12.041.

[38] K. E. Torrance and E. M. Sparrow. Theory for off-specular reflection from roughened surfaces*. *J. Opt. Soc. Am.*, 57(9):1105–1114, Sep 1967. doi: 10.1364/JOSA.57.001105. URL http://www.osapublishing.org/abstract.cfm?URI=josa-57-9-1105.

[39] Gregory J. Ward. The radiance lighting simulation and rendering system. In *Proceedings of the 21st Annual Conference on Computer Graphics and Interactive Techniques*, SIGGRAPH '94, page 459–472, New York, NY, USA, 1994. Association for Computing Machinery. ISBN 0897916670. doi: 10.1145/192161.192286. URL https://doi.org/10.1145/192161.192286.

[40] Gregory J. Ward. The radiance lighting simulation and rendering system. In *Proceedings of the 21st Annual Conference on Computer Graphics and Interactive Techniques*, SIGGRAPH '94, page 459–472, New York, NY, USA, 1994. Association for Computing Machinery. ISBN 0897916670. doi: 10.1145/192161.192286. URL https://doi.org/10.1145/192161.192286.

[41] Kurt Zimmerman. Developing the rendering equations. 2010.